POLITECNICO DI TORINO

Master's Degree in Energy and Nuclear Engineering

Master's Degree Thesis

Investigation of coarse-grid CFD approach for nuclear engineering application

Supervisors

Prof. Laura Savoldi

Dr. Haipeng Li

Dr. Jean-Marie LeCorre

Dr. Tobias Strömgren

Candidate

Michela Casarella

SEPTEMBER 2023

Authors

Michela Casarella <michelac@kth.se / s291265@studenti.polito.it>
Double Degree Nuclear Energy Engineering
KTH Royal Institute of Technology & Politecnico di Torino

Place for Project

Westinghouse Electric Company, Västerås, Sweden
KTH Royal Institute of Technology, Stockholm, Sweden

Politecnico di Torino Supervisor

Professor Laura Savoldi
Torino
Politecnico di Torino

KTH Supervisor

Dr. Haipeng Li
Stockholm
KTH Royal Institute of Technology

Westinghouse Supervisors

Dr. Jean-Marie LeCorre
Dr. Tobias Strömgren
Västerås
Westinghouse Electric Company

Abstract

In this thesis, an innovative coarse grid CFD approach is developed that aims to exploit the capabilities of sub-channel codes and CFD methods while overcoming their limitations. In the approach, a very coarse mesh is implemented in the CFD software OpenFOAM and a new wall treatment, based on the traditional concept of the wall function, is applied to the wall boundary conditions of the domain to take into account the low resolution of the grid which does not allow to effectively capture the effect of the solid walls on the thermo-hydraulics of the flow. To investigate the performance of the new approach, the method is implemented first in three simple test cases for which the sub-channel codes are the state-of-the-art thermo-hydraulic analysis since they are single-phase flow problems in which there are no prevailing 3D flow conditions. An additional test case representing a 2x2 fuel bundle with three full-length rods and one half-length rod is investigated to verify the behavior of the new approach in cases where secondary flows are present. The results for the pressure fields are compared with the analytical pressure profiles for the four test cases that well represent the ones that would be obtained with sub-channel code analysis, while the results for the wall shear stresses obtained in the four test cases are compared with the ones obtained with a more refined mesh in which the traditional wall function approach is implemented since they should be the best estimation of the actual wall shear stresses at the wall domain. For the first two cases, the developed approach produces reasonable results with a good agreement to the analytical pressure profiles while the other two test cases show that the methodology has a limited applicability and, before proceeding with the extension of the new approach to single-phase problems with 3D prevailing phenomena and two-phase problems, it is necessary to solve the issues that emerge for some types of cases.

Keywords

Acknowledgements

Acronyms

BC Boundary Condition

BDBA Beyond Design Basis Accident

BWR Boiling Water Reactor

CFD Computational Fluid Dynamics

CG-CFD Coarse Grid Computational Fluid Dynamics

CIWH Condensation Induced Water Hammer

CMFD Computational Multi-Fluid Dynamics

DBA Design Basis Accident

DES Detached Eddy Simulation

DLL Dynamic Link Library

DNB Departure from Nucleate Boiling

DNS Direct numerical simulation

FVM Finite Volume Method

GPL Genral Public License

GRS Gesellschaft für Anlagen- und Reaktorsicherheit - Global Research for Safety

HVAC Heating, Ventilation, and Air Conditioning

KTH Kungliga Tekniska Högskolan, Royal Institute of Technology

LBE Lead-Bismuth Eutectic

LES Large-Eddy Simulation

LOF Loss of Flow

LRGR Low-Resolution Geometry Resolving

MSM Momentum Source Model

NACIE Natural Circulation Experiment

OpenFOAM Open Field Operation And Manipulation

PDE Partial Differential Equation

PISO Pressure-Implicit with Splitting of Operators

PTS Pressurized Thermal Shock

PWR Pressurized Water Reactor

RANS Reynolds-Averaged Navier Stokes

RAS Reynolds Averaged Simulation

RELAP5 Reactor Excursion and Leak Analysis Program

SGM Sub-Grid Model

SIMPLE Semi-Implicit Method for Pressure Linked Equations

SYS-TH System thermal-hydraulics

UDF User Defined Functions

VHTR Very High-Temperature Reactor

1D One Dimensional

2D Two dimensional

3D Three dimensional

List of Tables

List of Figures

Nomenclature

A Cross-sectional flow area

$\mathbf{b}$ Body force per unit mass

C_f Fanning friction factor

C_μ k-epsilon model constant

Co Courant number

$\mathbf{D}$ Deformation tensor

D_h Hydraulic diameter

d Pipe diameter

d_rod Fuel rod diameter

E Empirical coeffcient

e_I Specific internal energy

f Darcy-Weisback friction factor

g Gravitational constant

$\mathbf{I}$ Identity matrix

I Initial turbulent intensity

k Turbulent kinetic energy

L Length of the domain

l Length scale

l_m Mixing length

n Coefficient of the velocity power law

pit Pitch of the subchannel

P Wetted perimeter

p Pressure

$\bar{p}$ Average pressure

p_{OUT} Outlet pressure

Δp Pressure drop

Δp_{fric} Frictional ressure drop

Δp_{grav} Gravitational pressure drop

Δp_{loc} Local pressure drop

$\Delta p_{loc,I}$ Irreversible local pressure drop

$\Delta p_{loc,R}$ Reversible local pressure drop

$\mathbf{q}''$ Heat flux vector

q Power generated in the fuel rod

q'' Heat flux magnitude

q''' Volumetric heat source

r Radial coordinate

R Half distance between two solid walls

Re Reynolds number

T_{IN} Inlet temperature

t Time

Δt Time interval

$\mathbf{u}$ Velocity field

U Velocity profile

u_{max} Maximum velocity

$\mathbf{u}'$	Velocity fluctuation
$\overline{\mathbf{u}'}$	Averaged velocity fluctuation
$\overline{\mathbf{u}}$	Averaged velocity field
U_{avg}	Averaged velocity
u	Velocity magnitude
u^+	Dimensionless tangential velocity
u_m	Characteristic speed
u_{IN}	Inlet velocity magnitude
u_P	Local velocity of a cell having centroid in the point P
u_τ	Friction velocity
Δx	Minimum size of a cell
y	Distance normal to the wall
y_P	Distance normal to the wall of a cell with centroid in the point P
y^+	Dimensionless distance normal to the wall
z	Axial coordinate
δ	Height of the cross-sectional flow area on the top of the half-length rod
ε	Turbulent dissipation rate
κ	Von Kármán constant
ν_t	Turbulent kinematic viscosity
ν_t	Wall kinematic viscosity
ν	Local kinematic viscosity
ρ	Density
σ^t	Viscous stress tensor
τ	Viscous stress tensor
τ_w	Wall shear stress

$\overline{\tau}$ Viscous stress tensor

τ^t Viscous component of the Reynolds stress tensor

ϕ Generic flow field

Contents

Chapter 1

Introduction

In the design and operation of a nuclear reactor, several aspects of heat transmission and fluid movement are involved. Nuclear reactor thermal-hydraulics is the field of nuclear engineering that deals with these aspects to assure a reactor's safe and stable power generation [1]. The goals of thermal-hydraulic analysis are frequently divided into two major categories: design and safety. Thermal-hydraulic design analyses are focused on developing nuclear systems and components that are robust and reliable, have a long and trouble-free continuance, are efficient and economical to operate, and are simple to inspect and maintain. Thermal-hydraulic safety assessments focus on ensuring that nuclear systems and components always function with operating margins compatible with the regulatory agencies' "defense-in-depth" strategy [2]. To mention some practical examples of thermal-hydraulic applications in the nuclear field, reference can be made to the prediction of fluid-structure interaction between the coolant and the reactor's internal components or the determination of the temperature distributions in the reactor core for different operating conditions to ensure that they are below specific limit values for various construction and fuel materials [1].

In this chapter, an outline of this thesis will be reported. Section 1.1 will introduce the specific context in thermal-hydraulic analysis that led to the interest in the topic covered in this thesis. In Section 1.2 the goals of this thesis will be announced and the position on the background presented in Section 1.1 in which this project wants to be placed will be stated. Section 1.3 will briefly examine the possible methodologies currently known to achieve the objectives introduced in Section 1.2 and the reasons for the choice of the methodology used for this thesis will be presented too. Then, the stakeholders involved in this thesis project will be mentioned in Section 1.4 and a brief

description of the following chapters will be presented in Section 1.5.

1.1 Background

The phenomena connected with thermal-hydraulics might be exceedingly complicated, necessitating the use of simulation tools. The computational tools used to simulate thermal-hydraulics-related events have evolved over time and are classified into three types: system codes (SYS-TH), sub-channel codes, and computational fluid dynamics (CFD) codes. The computational scale is one of the key distinctions between the three, with SYS-TH programs sacrificing detail for low computational cost and CFD being the most detailed alternative [3]. SYS-TH codes started to be developed in the early 1970s and they have a relevant position in nuclear applications since they have the capability to simulate steady states and transients of a reactor covering design basis accident (DBA) and some beyond DBA (BDBA) scenarios [4]. To solve for the flow characteristics of a reactor, SYS-TH codes average over time and space, providing an overall description of the circuits. The reactor is modeled by a combination of lumped parameter models, 1D, 2D, and 3D models. The imposed simplifications, along with the fact that nuclear reactors are extremely complicated systems, might result in designs with excessively large safety margins [3]. Additionally, these codes are heavily reliant on empiricism and experimental validation, for example, a new experimental program is necessary to study a new reactor design using SYS-TH codes [3].

The concept behind the sub-channel codes has been developed between the 60s and 80s. A sub-channel is a flow passage formed between a number of rods or a few rods and the channel/shroud tube wall. As shown in Figure 1.1.1 [5], the sub-channels can be formed by either coolant-centered sub-channels or rod-centered sub-channels [6]. A rod bundle, according to the sub-channel analysis approach, is considered a continuously interconnected set of parallel sub-channels containing one-dimensional flow coupled to each other by cross-flow mixing. The axial length is split into a number of increments, dividing the whole flow space of a rod bundle into nodes [6]. Sub-channel codes provide a relatively detailed thermal hydraulic analysis at the sub-channel scale by solving 1D transport equations such as mass, momentum, and energy conservation [7]. They have been developed to perform two primary functions: computing averaged local thermal-hydraulic conditions such as velocity, temperature, and pressure at the sub-channel level and evaluating various margins
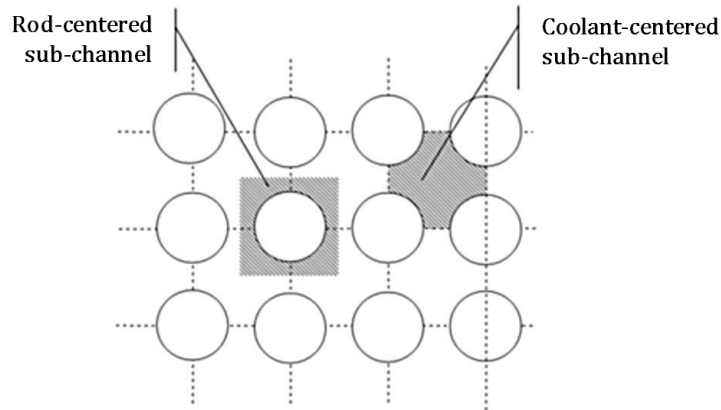
Figure 1.1.1: Definition of two types of sub-channels.

for operation and safety limits to meet the accuracy requirement for reactor thermal-hydraulic designs and safety analysis [8]. Sub-channel codes are widely regarded as the most powerful and widely used tools in nuclear reactor core thermal-hydraulic analysis [8]; in fact, reactor design and safety assessment in the nuclear industry continue to largely rely on them [7]. Sub-channel codes can provide an answer quickly [7] while saving computational cost and are suitable for accident simulation [9], but they cannot provide a detailed description of local features in simulations with 3D geometrical complexities, as well as the associated 3D coolant fluid motion [10] such as pressurized thermal shock, 3D coolant mixing, boron dilution and distribution in the reactor pressure vessel [9]. Furthermore, traditional approaches to plant safety based on sub-channel codes have been successful due to a large database of empirical correlations established from essentially 1D separate effects experiments [10] to account for un-resolved physics such as frictional loss, spacer induced effects, turbulence, inter-channel mixing, and void drift, among other things [7]. This procedure, upon which sub-channel codes are based, has resulted in sub-channel codes that are heavily reliant on experiments and empiricism. Additionally, the knowledge of the exchanges of mass, momentum, and energy between phases for multiphase 3D flows is also very limited, so it is unacceptable to apply sub-channel codes that were developed for 1D situations to 3D situations though this is frequently done for lack of a better choice [10]. The current trend in reactor design has however been to continue with approaches based on sub-channel codes because of their well-established and reliable physical models or often simply in lack of a better choice [10]. With the widespread idea that traditional 1D codes are no longer sufficient to meet the requirements of modern reactor design and with the advance of computing power, CFD approaches have become increasingly

relevant [7]. CFD could provide detailed 3D features and enable the solution through numerical simulation of many 3D flow conditions prevailing problems that were previously only addressed experimentally [7]. The main issue in the CFD context is the computational overhead associated with 3D flow studies [10]. This is due to the wide range of flow scales in a nuclear reactor, which necessitates meshing the computational domain of a CFD model with a fine grid to capture most physical scales. As a result, even with today's high-performance computing systems, performing core-level CFD simulations is still impractical due to prohibitive computing costs [7]. In addition to data storage and CPU issues, the generality, complexity and flexibility of CFD methods, not being developed specifically for nuclear reactor design, make the uncertainties related to user inputs as initial and boundary conditions [7], user effects emerging in the meshing procedure, physical models, scaling distortions and numerical instabilities [10] very difficult to measure and control [7]. In fact, CFD is a general tool and its application to nuclear reactor design is more challenging than for other industrial applications. Although the technology is advancing, progress in this field has been constrained by the time scales associated with the advancements in computer tackle and the effectiveness of the numerical algorithms being used to ensure processing of the information in respectable times [10].

1.2 Goal and Purpose

From the context presented in Section 1.1, the need to develop solutions that can exploit the capabilities of sub-channel and CFD codes and at the same time overcome their limitations seems to emerge. The main objective of this thesis is to develop an innovative approach to answer this need. In other words, this project aims to create and implement a new approach that aims to potentially replace traditional sub-channel codes for thermal-hydraulic core analysis by combining the advantageous features of modern CFD and 1D sub-channel codes. The intention behind the new methodology, which will be described in detail in Chapter 3, is to produce 3D CFD-level results with accuracy at least as good as those obtained with sub-channel codes while avoiding the simplifications associated with traditional codes and circumventing the prohibitive computational costs associated with conventional CFD simulation. Furthermore, this thesis serves as a feasibility study for the use of the CFD software OpenFOAM on which the methodology developed for this project has been implemented, opening future

possibilities to adapt this new approach to multiphase cases.

1.3 Methodology

To develop solutions in thermo-hydraulic analysis that can take advantage of the capabilities of subchannel codes and CFD methods but suffer as little as possible from their limitations many studies have been performed in recent years. The methodologies developed as a result of these works can generally be divided into two categories: coupling methods and coarse grid CFD approach. The methodology developed in this thesis is placed in the second category, but the general understanding of both typologies is considered of relevant importance for this project.

1.3.1 Coupling methods

The coupling methods are techniques that combine several multiscale codes to achieve a balance between computational accuracy and solution time [9]. In such techniques, CFD is typically used to capture the complex 3D flow of the reactor system's most interesting regions/sections, while the remaining parts are depicted using simplified models using system/subchannel codes [7]. Some of the relevant technological experiences in this research field are reported below. Andersson et al. [11] develop a multi-scale simulation method that can be used for reliable design of novel multiphase reactors in which the turbulence is continuously produced and dissipated along the reactor. For this particular feature of these new reactors, the traditional process development using correlations based on average quantities such as energy dissipation is not reliable, so a new method is developed using a system analysis code coupled with a CFD code. Martelli et al. [12] successfully develop and test a coupling methodology between a modified version of the RELAP5/Mod3.3 SYS-TH code and the commercial CFD code Fluent, which is applied to the natural circulation experiment (NACIE) lead-bismuth eutectic (LBE) experimental loop built and located at the ENEA Brasimone research center. Aumiller et al. [13] develop a code system combining RELAP5-3D and a multiphase CFD program through the use of a general semi-implicit numerically stable coupling algorithm. Anderson et al. [14] analyze the hot gas inflow in the outlet plenum of the very high-temperature reactor (VHTR) using coupled RELAP5-3D system code and a CFD code. By coupling the two codes, the three-dimensional flow phenomena are well captured while avoiding modeling the entire reactor with a

computationally expensive CFD code. Guelfi et al. [15] develop the NEPTUNE project that constitutes the thermal-hydraulic part of the long-term Electricité de France and Commissariat à l'Energie Atomique joint research and development program for the next generation of nuclear reactor simulation tools. NEPTUNE is a multiscale coupled simulation platform for advanced two-phase flow thermal hydraulics covering the whole range of modeling scales, the system scale, the component or subchannel scale and CFD in open medium, allowing easy multiscale and multidisciplinary calculations. The NURESIM and NURISP [16] have developed and validated a reference multiphysics and multi-scale platform for reactor simulation that includes system codes, component codes, and also CFD or CMFD (Computational Multi-Fluid Dynamics) simulation tools. Within these projects, a multi-scale analysis is applied to Departure from Nucleate Boiling (DNB), to Dry-Out, to Pressurized Thermal Shock (PTS), to core Reflooding heat transfers, to Condensation Induced Water Hammer (CIWH), and to core thermal-hydraulic in general. Gesellschaft für Anlagen- und Reaktorsicherheit - Global Research for Safety (GRS) develops a methodology for the coupling of the thermal-hydraulic system code ATHLET with the 3D CFD software ANSYS CFX and validation activities for their coupling code are performed based on a PTS related experiment within the European project NURISP [17]. Li et al. [18] carry out a preliminary study for an explicit coupling strategy of the 3D CFD code ANSYS-Fluent with the 1D thermal–hydraulic system code RELAP5/MOD3.1 by using the Dynamic Link Library (DLL) technology and FLUENT User Defined Functions. Toti et al. [19] develop a coupling method between the system thermal-hydraulic code RELAP5-3D and the CFD code Fluent for high-fidelity safety analyses of pool-type reactors. The methodology is developed to assess the effects of 3D phenomena occurring in accidental transients such as loss of flow (LOF) in the research reactor MYRRHA and it is used for validation purposes against the experimental data obtained at the test facility TALL-3D, operated by the KTH - Royal Institute of Technology in Sweden. The developed method shows good agreement with the experimental data.

A subcategory of the coupling methods is related to the coupling between porous media models with the well-resolved CFD. In the porous-media approach, the porous or perforated structure such as the fuel assemblies, packed beds, filter papers, perforated plates, and tube banks is represented by its volume-averaged properties via a geometrically defined porous region of a certain volume. In essence, the porous media model is nothing more than the addition of a momentum source term to the

standard fluid flow equations where the source terms represent the macroscopic effects of the porous structure on the flow [20]. However, this kind of coupling method has issues similar to the sub-channel code ones reported in Section 1.1. Additionally, the main issues related to the multiscale coupling method of system code and CFD method are related to computational stability, low convergence rate, 1D and 3D code coupling boundary condition processing, and computational errors caused by different program physical models [9].

1.3.2   Coarse grid CFD approach

Coarse-grid CFD approach can be employed as a complementary and potentially substitutive approach to resolved CFD and subchannel codes/porous medium modeling and for this reason it is a new and interesting area of research in the recent years. Some of the relevant technological experiences in this research field are reported below. Hu and Fanning [21, 22] develop the concept and formulation of a three-dimensional momentum source model (MSM) that allows to improve the thermal-hydraulic modeling of wire-wrap spacers in a rod bundle. The method consists in a 3D momentum source that spirals around each rod that is introduced to characterize the effects of wire-wrap spacers on the hydraulics in the rod bundle. The wire-wrapped rod can be then simulated using bare-bundle geometry saving significant computing resources due to the reduced number of computational cells needed. The momentum source is represented as a body force within the volume previously occupied by the wire-wrap. The MSM is implemented in STAR-CCM+ and provides reasonably accurate predictions of T, p, and fluid flow velocities for both steady-state and transient conditions.

In the work done by Roelofs et al. [23] a Low-Resolution Geometry Resolving (LRGR) CFD approach and a Coarse-Grid (CG) CFD approach are discussed. The methods are based on resolving the geometry of the fuel assembly to a certain degree using a low-resolution mesh that allows capturing of large and medium-scale flow features that are difficult to be reproduced by the system codes, sub-channel codes and porous media approaches. The approaches can be applied without and with a sub-grid model (SGM) not allowing and allowing, respectively, to take into account the physics which is included at scales with resolution lower than the mesh resolution, such as secondary flows. The approach with SGM is able to represent the non-resolved sub-grid physics by adding volumetric forces accessed by detailed CFD simulations. This method

applies to problems where similar flow situations repeat frequently in a large domain so that instead of simulating the whole domain with many similar flow patterns at distinct locations, the appearing flow patterns are computed just a single time, then the global flow is simulated by assembling local behavior.

Similar approaches, involving volumetric forces and the exploitation of blocks that repeat in a domain, are tested by Viellieber et al. [24] and Viellieber and Class [25]. Their study is based on the observation that in many cases there are repetitive geometry and flow patterns in a complete nuclear reactor that allows to create a parametrized model for a single segment and composing many of these reduced models to obtain the entire reactor simulation. Traditionally, this approach leads to sub-channel analysis codes that are relying heavily on transport models based on experimental and empirical correlations, but instead, this methodology aims to replace the experimental or empirical inputs with CFD data. The method application starts with a detailed, well-resolved, and verified CFD simulation of a single representative segment from which volumetric forces are extracted, then they are associated with all coarse cells upon parametrization. Other studies aiming to avoid the dependency of the simulations on correlations and experimental data are presented by Capone et al. [26] and by Roleofs and Doolaard [27]. The first is a source terms modeling approach for spacer grids with mixing vanes which starts with calculation with a body-fitted mesh of one grid span of a fuel assembly with spacer grids featuring dimples, springs, and mixing vanes. Velocities and Reynolds Stresses are extracted from this mesh, then converted to source terms. A new computational domain is created with a low-resolution mesh and without the presence of dimples, springs, and vanes, but source terms are added to the momentum and Reynolds Stress transport equations to force the solution as the detailed geometry computation. The forcing is imposed in only a few volumes of the domain where dimples, spring, and vanes are located. The second is a reduced-resolution CFD model able to obtain local data taking into account the geometric details of the flow unlike porous medium approaches and at a more affordable computational cost than a well-resolved CFD simulation.

Another approach that can be classified in the same category of the previously mentioned methods is the one proposed by Mikuz and Roelofs [28] which consists in the application of a porosity model with the addition of momentum sources in the governing equations for the simulation of the mixing phenomena in PWR fuel assemblies. The magnitude of the momentum sources have been tuned to generate

similar magnitudes of the secondary flow and stream-wise vorticity as observed in the results of the reference CFD simulation of a PWR fuel assembly with a split-type design of mixing grid.

The common feature of the aforementioned approaches is the addition of momentum sources to the governing equation to take into account the low resolution of the meshes implemented. The momentum sources are in all the cases extracted from well-resolved CFD simulations to reduce as much as possible the dependence on experimental and empirical input. The approach presented by Liu et al. [7], instead, computes the momentum source term, representing the wall shear stress, as a whole using friction correlation and the sub-channel bulk velocity. In fact, their approach consists of a very coarse grid simulation implemented in a standard CFD solver using empirical correlations of the frictional loss and heat transfer to ensure correct integral effects of the solid walls.

Hanna et al.[29]'s study totally differs from the previously mentioned Coarse-Grid CFD approaches. Since the discretization error increases when relying on coarse grids, the idea of the work put forward is to predict the CG-CFD local errors with a surrogate model that relates the local error and the coarse grid features in order to correct the variables of interest.

1.3.3 Implemented Methodology

The methodology developed and implemented in this project is similar to the method developed by Liu et al. [7] exploiting empirical correlations with respect to well-resolved CFD data, but the wall shear stress does not enter the discretized equations as a source term but it is taken into account through a newly developed wall treatment. In the methodology, a very coarse mesh will be implemented in a standard CFD software and to take into account the low resolution of the grid, which does not allow to effective capture the effect of the solid wall on the thermal-hydraulics of the flow, a new wall treatment will be applied to the cells to the wall. The mathematical derivation of the wall treatment will be presented in detail in Chapter 4, while the results obtained with its application will be reported in Chapter 5.

1.4 Stakeholders

There are three primary stakeholders in the project:

- Westinghouse Electric Sweden AB, who are funding the work;

- The examiner and supervisor at KTH - Royal Institute of Technology, who are both involved in the field of thermal-hydraulics research;

- The supervisor at Politecnico di Torino.

1.5   Outline

Chapter 2 of this thesis will deal with all relevant theoretical background to the project with a main focus on CFD general principles. The software used to perform the simulations will be introduced in Chapter 3. Chapter 4 will explain the derivation and implementation of the approach developed for this project. The results and discussion will be addressed in Chapter 5. Chapter 6 will report the conclusions of the project, including suggestions for future work.

Chapter 2

Theoretical Background

This chapter is dedicated to the project's underlying theory. In Section 2.1 a brief introduction to CFD problem description is given. Section 2.2 reports the governing equations in CFD, the derivations of which are not reported in this thesis as they are beyond its scope. In section 2.3 the description of the discretization method used for the approximation of the conservation laws is reported. Section 2.4 covers turbulence modeling and Section 2.5 is focused on the wall treatment performed in CFD analysis.

2.1 CFD Problem Description

As already mentioned in Section 1.1 of Chapter 1, CFD is one of the computational tools used to simulate thermal-hydraulics-related events. It can be defined as the prediction of fluid motion and forces by computation using numerical analysis, generally extended to include heat, thermodynamics, chemistry, and solids when relevant [30].

To perform the calculation of fluid flow, a description of the problem is needed including the domain occupied by the fluid, the equations that represent the fluid behavior, and the conditions at the boundary of the fluid domain and initially within the domain for the fluid properties. This description in CFD is represented by, respectively, a computational mesh for the fluid, "discrete" equations and algorithms to compute the flow parameters, and initial and boundary conditions [30]. The bridges between these descriptions are the numerical methods that CFD uses to solve the equations since closed-form, analytical solutions only exist for very simple geometries and flow

regimes. The finite volume method (FVM) is the numerical method implemented in the software OpenFOAM that was used for this thesis and of which a detailed description will be provided in Chapter 3. The role of the FVM is to represent continuous physical entities by equivalent discrete entities such as:

- **time** is split into intervals of duration Δt;

- **space** becomes cells of a mesh in which the solution domain is subdivided;

- **fields**, e.g. **u**, become discrete values, so one value per each cell;

- **partial differential equations**, e.g. for momentum, become a set of linear equations represented by matrices.

A schematic representation of the operations performed by CFD numerical methods is shown in Figure 2.1.1 [30].
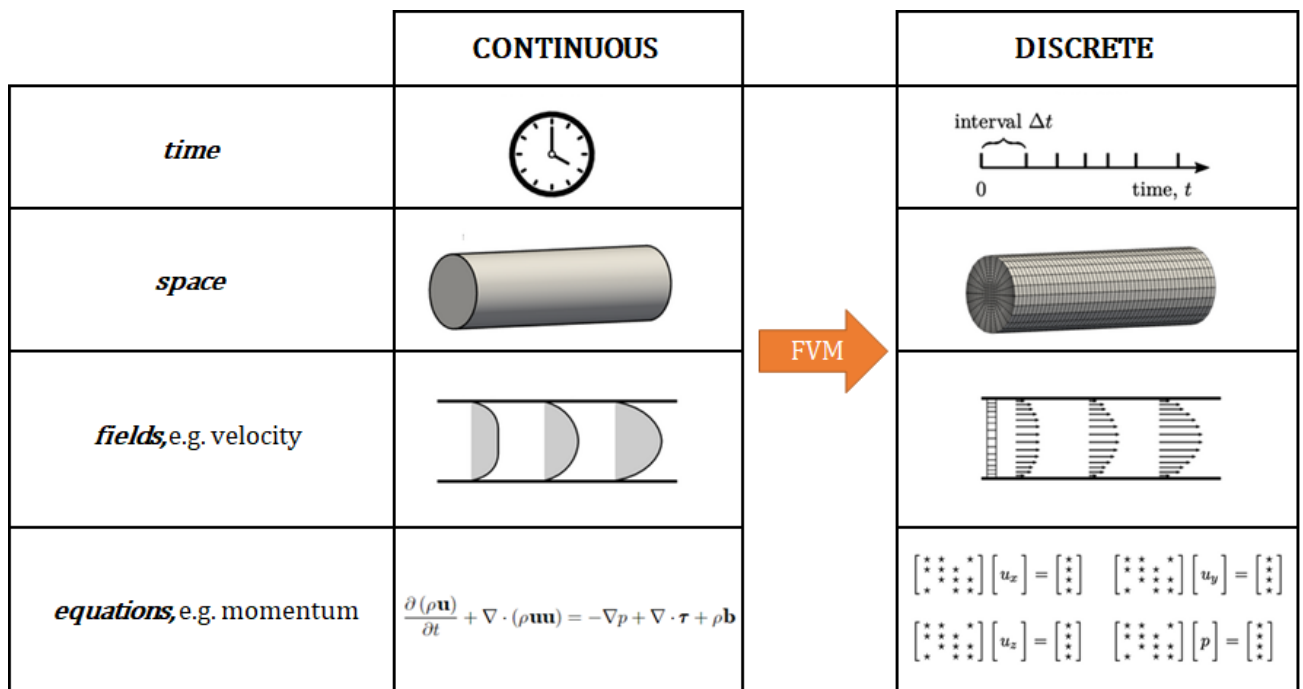
Figure 2.1.1: Schematic representation of CFD numerical method operations.

2.2 Governing equations

The continuity, momentum, and energy equations are the fundamental governing equations of fluid dynamics and serve as the central pillars of CFD. They are the

mathematical statements of three fundamental physical principles upon which all of fluid dynamics is based [31]:

1. conservation of mass;

2. Newton's Second Law of motion;

3. First Law of Thermodynamics.

The derivations of the governing equations will not be reported in this thesis, but their form of partial differential equations will be presented in the following subsections.

2.2.1 Conservation of Mass

The conservation of mass is the first basic principle of fluid dynamics that states that "mass can neither be created nor destroyed, more precisely, the net mass crossing a system boundary must be balanced by an accumulation or depletion of mass in the system" [32]. The mass conservation equation, also called continuity equation, can be expressed by the differential equation Eq. 2.1 [1].

$$\frac{\partial \rho}{\partial t} + \nabla \cdot (\rho \mathbf{u}) = 0 \tag{2.1}$$

Where ρ is the density of the fluid and $\mathbf{u}$ is the fluid velocity vector.

2.2.2 Conservation of Momentum

The momentum conservation equation is simply a restatement of Newton's Second Law of motion [33]. The conservation of momentum can be described by the differential equation Eq.2.2 [1].

$$\frac{\partial (\rho \mathbf{u})}{\partial t} + \nabla \cdot (\rho \mathbf{u} \mathbf{u}) = -\nabla p + \nabla \cdot \boldsymbol{\tau} + \rho \mathbf{b} \tag{2.2}$$

$\mathbf{b}$ represents any body force per unit mass. Assuming that only the gravitational force is involved, the Eq. 2.2 can be rewritten as Eq. 2.3.

$$\frac{\partial (\rho \mathbf{u})}{\partial t} + \nabla \cdot (\rho \mathbf{u} \mathbf{u}) = -\nabla p + \nabla \cdot \boldsymbol{\tau} + \rho \mathbf{g} \tag{2.3}$$

τ is the viscous stress tensor that, in three dimensions, is a 3x3 matrix containing the viscous shear stresses.

2.2.3 Conservation of Energy

The energy conservation equation is a restatement of the first law of thermodynamics which states that "the total energy change in system equals the difference between the heat transferred to the system and the work done by the system to its surroundings" [34]. The conservation of energy can be expressed by the differential equation Eq. 2.4 [1].

$$\frac{\partial \left[\rho \left(e_I + \frac{1}{2}u^2\right)\right]}{\partial t} + \nabla \cdot \left[\rho \mathbf{u} \left(e_I + \frac{1}{2}u^2\right)\right] = -\nabla \cdot \mathbf{q}'' - \nabla \cdot (p \cdot \mathbf{u}) + \nabla \cdot (\boldsymbol{\tau} \cdot \mathbf{u}) + \rho \mathbf{b} \cdot \mathbf{u} + q'''$$
$$(2.4)$$

Assuming, as for Eq. 2.3, that only the gravitational force is involved, the Eq. 2.4 can be written as Eq. 2.5.

$$\frac{\partial \left[\rho \left(e_I + \frac{1}{2}u^2\right)\right]}{\partial t} + \nabla \cdot \left[\rho \mathbf{u} \left(e_I + \frac{1}{2}u^2\right)\right] = -\nabla \cdot \mathbf{q}'' - \nabla \cdot (p \cdot \mathbf{u}) + \nabla \cdot (\boldsymbol{\tau} \cdot \mathbf{u}) + \rho \mathbf{g} \cdot \mathbf{u} + q'''$$
$$(2.5)$$

e_I is the specific internal energy of the fluid, while $\frac{1}{2}u^2$ is the definition of the specific kinetic energy. q''' is a volumetric heat source and $\mathbf{q}''$ is the heat flux vector.

2.3 Finite volume method

The Finite Volume Method (FVM) is a discretization method for the approximation of a single or a system of partial differential equations (PDEs) expressing the conservation, or balance, of one or more quantities [35]. As mentioned previously, the FVM is the numerical method implemented in the software OpenFOAM to discretize the PDEs decsribed in Section 2.2.

2.3.1 Space discretization

FVM adopts the idea of control volumes used to model physical systems. A control volume is a region of space enclosed by a surface through which fluid flows in and

out [30]. In essence, in FVM, the system domain is partitioned into a mesh and the elements of the mesh are control volumes, called cells [35]. Conservation equations are applied to each cells, guaranteeing that the fluxes of mass, momentum, and heat across faces are harmonious and conservative between the volumes they connect. The cells contained in the meshes of modern CFD can have any polyhedral shape and they are contiguous which means that the faces of a given cell are common to its neighbouring cells as shown in Figure 2.3.1.
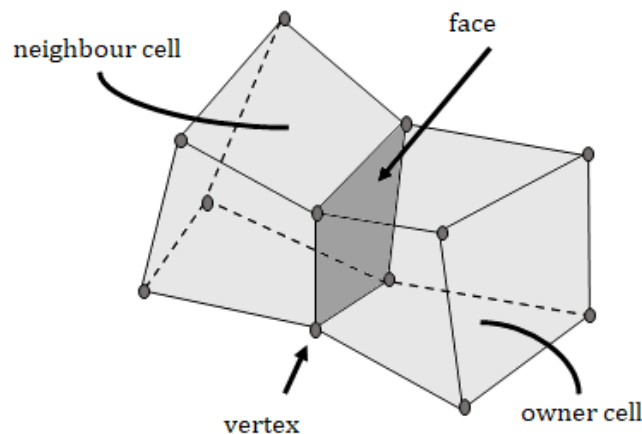
Figure 2.3.1: Two polyhedral contiguous cells.

Each face inside the mesh is common to two cells, one known as the owner cell, and the other as the neighbour cell. At the domain boundary, each face is connected to one owner cell. The cell faces that describe the domain boundary are separated into groups, known as patches, with unique names, on which the boundary conditions can be applied [30].

Meshing plays an important role when performing computational analysis fluid simulation using CFD. The accuracy of the simulation depends heavily on the creation of a high-quality mesh. Some requirements to achieve a high-quality mesh are reported below:

- Minimal skewness of the cell, where the skewness is defined as the difference between the shape of the cell and the shape of an equilateral cell of equivalent volume. Highly skewed cells can decrease the accuracy of the solution. A general rule is that skewness in a mesh must be below 0.95 with an average value lower than 0.33 [36].

- The aspect ratio of the cells in the internal region should be between 0.2 and

5 while the aspect ratio of the cells near the wall should be smaller than 0.2 or bigger than 5 [37]. The aspect ratio is a measure of the stretching of the cell, for example for hexahedral cell it is the ratio of maximum edge length to the minimum edge length. Generally, the recommended aspect ratio in CFD for inner cell is 1 and for wall cells is 10. The maximum allowed for wall cell is 20 [38].

- A high level of non-orthogonality should be avoided since it causes numerical instability. Non-orthogonality is the angle between the vector connecting two contigous cell centers and the normal of the face shared by these cells. Generally, it is recommended to keep the non-orthogonality below 70 [38].

- Avoid rapid changes in cell volume between adjacent cells because it can translate into larger truncation errors where the truncation error is the difference between the partial derivatives in the governing equations and their discrete approximations [36].

- High mesh density. The density and distribution of nodes in the mesh determine how well the important flow characteristics are resolved. Many times, inadequate resolution in crucial areas can significantly change the flow characteristics. Generally, no flow passage should be represented by fewer than 5 cells, however, most cases will require many more cells to adequately resolve the passage [36].

2.3.2 Equation discretization

As mentioned in the previous subsection, the PDEs are applied to each cell and to solve them the equation discretization is needed. The partial differential equations for continuous fields are converted into sets of linear equations for discrete fields. Each cell is associated with a value of the principal fields, in this way a field Φ is represented by an array of values Φ_i, for cell indices $i = 1, 2, 3, ..., N$, where N is the total number of the cells in which the domain is split [30].

For each cell, a linear equation is created with the equation discretization procedure. The discretization procedures of each differential operator appearing in the governing equations presented in section 2.2 is beyond the scope of this thesis so they will not be analyzed, but the form of the resulting linear equation, taking as example cell 14 highlighted in Figure 2.3.2, is reported in Eq. 2.6 [30].

$$a_{14,9}\Phi_9 + a_{14,15}\Phi_{15} + a_{14,14}\Phi_{14} + a_{14,13}\Phi_{13} + a_{14,20}\Phi_{20} = b_{14} \qquad (2.6)$$
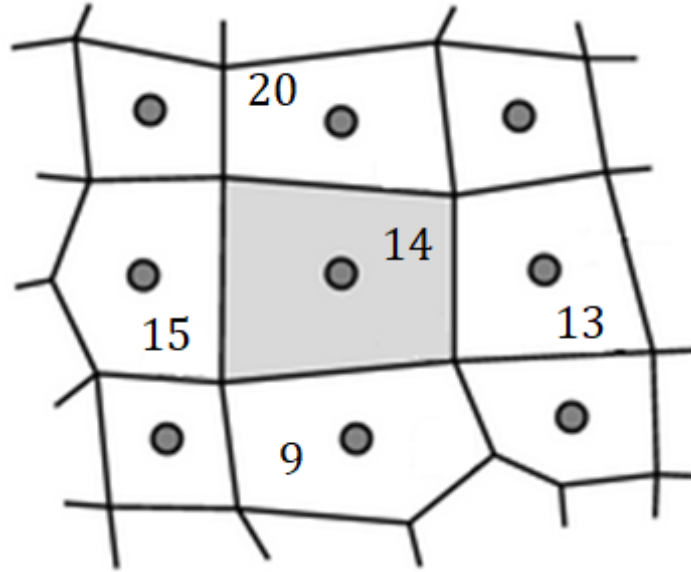
Figure 2.3.2: Zoom on a part of the mesh.

Where $a_{i,j}$ and b_i are coefficients corresponding to cell indices i,j, and $a_{i,i}$ are the diagonal coefficients. The resulting system of linear equations can be written as a matrix equation reported in Eq. 2.7 [30].

$$
\begin{bmatrix}
a_{1,1} & a_{1,2} & a_{1,3} & \cdots & a_{1,N} \\
a_{2,1} & a_{2,2} & a_{2,3} & \cdots & a_{2,N} \\
a_{3,1} & a_{3,2} & a_{3,3} & \cdots & a_{3,N} \\
\vdots & \vdots & \vdots & \ddots & \vdots \\
a_{N,1} & a_{N,2} & a_{N,3} & \cdots & a_{N,N}
\end{bmatrix}
\begin{bmatrix}
\Phi_1 \\ \Phi_2 \\ \Phi_3 \\ \vdots \\ \Phi_N
\end{bmatrix}
=
\begin{bmatrix}
b_1 \\ b_2 \\ b_3 \\ \vdots \\ b_N
\end{bmatrix}
\tag{2.7}
$$

The matrix contains a set of coefficients $a_{i,j}$, and the coefficients in each row correspond to the linear equation for the cell with index i. Each coefficient in the row is non-zero only if j corresponds to the near-neighbour cell indices. All the other coefficients in the row are zero, so the matrix is extremely sparse. The matrix equation in Eq. 2.7 can be represented as the Eq. 2.8

$$
[A][\Phi] = [b]
\tag{2.8}
$$

where $[A]$ are the matrix coefficients, $[b]$ are the source coefficients, and, $[\Phi]$ is the discretized field [30].

2.3.3 Time discretization

The Euler scheme is the time discretization used for the simulations presented in this thesis. The local derivative of a field Φ, $\frac{\partial \Phi}{\partial t}$, appearing in Eqs. 2.1, 2.3, and 2.5, is discretized as a finite difference in time between the field at the current time t and the field at the previous time $t - \Delta t$, where Δt is the discrete interval duration in which the time is split. The time discretization contributes only to the diagonal coefficients of the matrix $[A]$ and to the source vector $[b]$ in Eq. 2.8 [30].

2.4 Turbulence models

Turbulence is the apparent chaotic movement of fluid flows [39]. Fluid flows can be laminar when they are regular and flow in an orderly manner with a relatively straight, narrow path. The transition to a turbulent flow occurs when the speed or characteristic length of the flow is increased and then the convective forces in the flow overcome the viscous forces of the fluid. The turbulent flow is characterized by fluid particles following curved paths which cross one another in a disorderly, irregular manner [39] as shown in Figure 2.4.1.
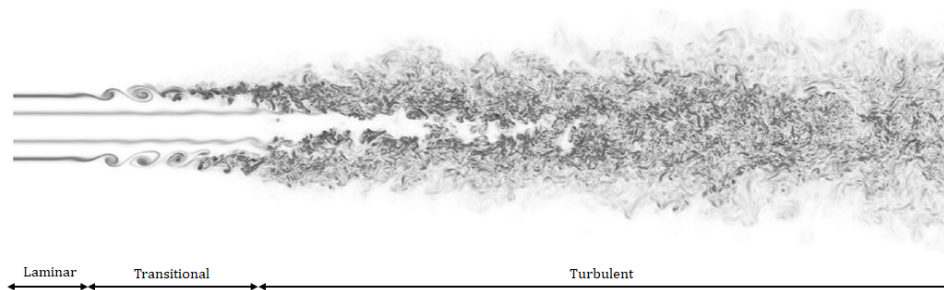
Figure 2.4.1: Laminar to turbulent flow transition [40].

This transition is controlled by the Reynolds number (Re) which is the ratio between convective and viscous forces [41]. This number can be used to classify the type of flows, for example for pipe flow the value of the Reynolds number which establishes the transition from laminar to turbulent flow is from 2000 to 4000 [42].

The vorticity is often used to describe turbulence and it is primarily generated at solid boundaries in the boundary layers [43] due to tangential fluid pressure gradient and relative acceleration of fluid and wall [44].

Turbulent flows are characterized by a large size range of vortical structures, called eddies, which interact with each other, change shape and size rapidly, and exchange

energy. At sufficiently high Re the larger eddies are broken into smaller ones and their kinetic energy is transferred to progressively smaller structures, until they "die out" before they can become any smaller [30]. The process of energy transfer from large to small scale is called energy cascade [39] and the smallest scales of length, velocity, and time that can exist in turbulent flow is the Kolmogorov microscales [45].

Turbulence models in CFD are methods to include the effect of turbulence in the simulation of fluid flows [39]. An overview of the most popular methods for resolving turbulent flows is shown in Figure 2.4.2.
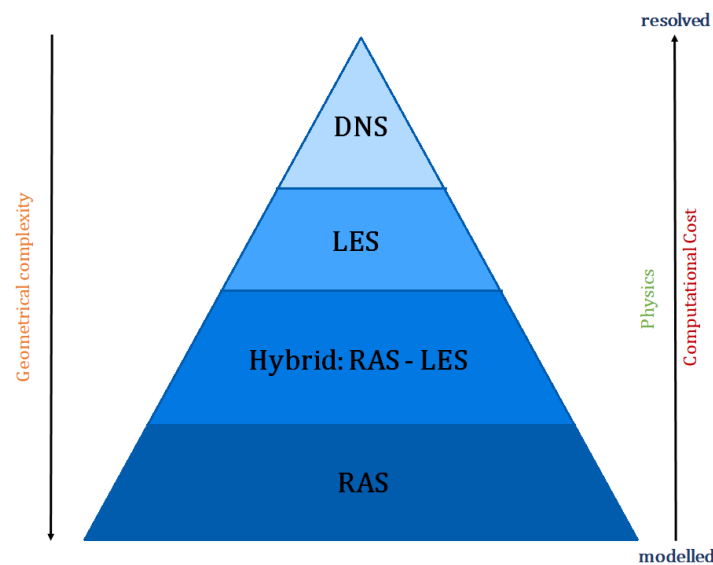
Figure 2.4.2: Approach to solve turbulent flow in CFD.

The computational cost of a CFD simulation rises from RAS to DNS. Until now, scale-resolving methods like DNS and LES are typically applied to simple geometries and academic configurations due to the computational cost, whereas hybrid RAS-LES, and RAS can be applied to complex industrial problems [39].

2.4.1 DNS

The fact that the scales involved in turbulence are so small has important consequences for CFD because to resolve the smallest eddies with CFD without the use of any modelling assumption the mesh resolution and time steps required would be several orders of magnitude bigger than the one actually obtainable. This approach to solve turbulent flow is called Direct Numerical Simulation (DNS), it is virtually impossible for engineering applications for the reasons mentioned, but it is used in academia and research institutions to model simple flow [39].

2.4.2 LES

Large-eddy simulation (LES) makes use of modelling for the unresolved smallest scales while accurately capturing the large eddies that contain most of the energy of the flow. The energy dissipation from the resolved scales to the unresolved ones is performed at a realistic rate by effective models [30]. However, the LESs are still relatively expensive because they are inherently transient, necessitating strong convergence within each time step for accuracy. Long simulation times are required to generate time-averaged properties that are reliable due to still relatively large mesh sizes [39].

2.4.3 Hybrid: RAS-LES

Where LES would be too expensive, a family of turbulence models uses the advantages of LES modelling while maintaining the effectiveness of RAS models that will be explained in the following subsection. These are referred to as hybrid RAS-LES models. Given that the flow in LES must be fully resolved close to the wall, the majority of the mesh resolution typically occurs there. As a result, the cost of LES can be significantly decreased if the limitations of the increased resolution close to the wall can be relaxed. LES modelling away from the walls and RAS modelling close to the wall make up one of the most popular hybrid approaches. This method is called Detached Eddy Simulation (DES). Even in cases where there is a steady state solution, the simulation is always run as an unsteady flow, and the finer spatial resolution allows for the study of the specific behaviour of the flow of interest. This helps overcome some of the limitations of the RAS models and provides increased insight into the solution [39].

2.4.4 RAS

The computational cost of DNS and, to a lower extent, LES is too large for most practical CFD applications. Rather, a Reynolds-Averaged Simulation (RAS) provides a much more affordable approach to calculate turbulence [39]. Since the RAS models are used for the simulations presented in this thesis, a more detailed description of this turbulence modelling approach will be delivered in this subsection.

RAS solves equations for "averaged" field variables to avoid resolving small fluctuations. From the mathematical point of view, the RAS models use the momentum conservation equation Eq. 2.3 in terms of averaged properties only and with an additional term that includes the Reynolds stress tensor σ^t containing the fluctuation

of the field **u**. The resulting equation is reported in Eq. 2.9.

$$\frac{\partial \left(\rho \overline{\mathbf{u}} \right)}{\partial t} + \nabla \cdot \left(\rho \overline{\mathbf{u}\mathbf{u}} \right) = -\nabla \overline{p} + \nabla \cdot \left(\overline{\boldsymbol{\tau}} + \boldsymbol{\sigma^t} \right) + \rho \mathbf{g} \qquad (2.9)$$

Solving this Reynolds-Averaged equation Eq. 2.9 is the key to low cost CFD with turbulence, but it requires a model for the additional unknown tensor $\boldsymbol{\sigma^t}$. The RAS family of turbulence models provide methods to approximate the Reynolds stress tensor. These methods can be based on linear and non-linear eddy viscosity models, and Reynolds stress transport models [46]. In this thesis only the RAS based on the eddy viscosity model of Boussinesq [30] are described since one of them is used in the simulations presented. Boussinesq [47] related the shear stress, due to turbulence, to the velocity gradient through an eddy viscosity ν_t. The $\boldsymbol{\sigma^t}$ obtained from the eddy viscosity model of Boussinesq is reported in Eq. 2.10.

$$\boldsymbol{\sigma^t} = \boldsymbol{\tau^t} - \frac{2}{3} \rho k \mathbf{I} \qquad (2.10)$$

Where $\boldsymbol{\tau^t}$ is the viscous component of Reynolds stress and it is expressed as Eq. 2.11.

$$\boldsymbol{\tau^t} = 2 \rho \nu_t dev \mathbf{D} \qquad (2.11)$$

Where **D** is the deformation tensor defined as the symmetric part of the tensor $\nabla \mathbf{u}$ [30]. Two important quantities arise from this model, the turbulent kinetic energy per unit mass k, and the turbulent viscosity ν_t. The turbulent kinetic energy is expressed as Eq. 2.12.

$$k = \frac{\overline{\mathbf{u}'^2}}{2} \qquad (2.12)$$

Where $\mathbf{u}'$ is the velocity fluctuation due to turbulence. The turbulent viscosity ν_t is proportional to a representative speed u that relates to $\mathbf{u}'$ and length l according to Boussinesq's hypothesis. It can also be expressed as the Eq. 2.13 by absorbing the constant of proportionality within a characteristic speed u_m and a mixing length l_m.

$$\nu_t = u_m l_m \qquad (2.13)$$

In this way two models are required to compute ν_t. The characteristic speed u_m is assumed to be proportional to $k^{\frac{1}{2}}$ since being of the same scale of $\mathbf{u}'$, so in this way the field k is representative of the u_m component of ν_t. The turbulent kinetic energy can be described by a transport equation, but it includes a term for its rate of dissipation

ε. The turbulent dissipation rate can be expressed as the proportion reported in Eq. 2.14.

$$\varepsilon \propto \frac{k^{\frac{3}{2}}}{l_m} \tag{2.14}$$

In this way, the turbulent dissipation rate is representative of the l_m component of ν_t. The turbulent dissipation rate can be described by a transport equation too.

To summarize, RAS models take the form of transport equations for turbulence fields to close the system of PDEs to solve the turbulent fluid flow.

The RAS model used for all the simulations performed in this project is the realizable k-ε model. The mathematical expressions of the transport equations for the turbulent kinetic energy k and its dissipation rate ε that constitute the model are not reported as they are beyond the scope of the thesis.

A good representation of how the accuracy of the simulation of a flow is affected by the turbulence modelling is reported in Figure 2.4.3.
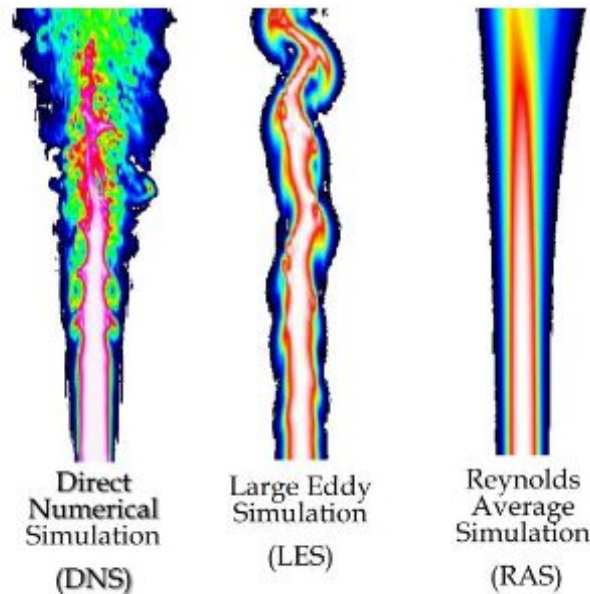
Figure 2.4.3: Comparison of a DNS, LES and RAS simulation of a jet flow.

2.5   Wall treatment

Looking at the behaviour of velocity in a fluid domain, a profile that approaches zero at the wall, due to the no-slip boundary condition, and that has some quite steep gradients as it approaches the wall is expected as shown in Figure 2.5.1 [48].
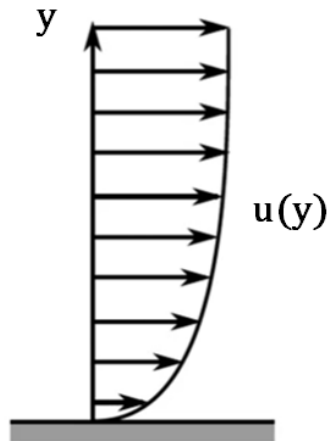
Figure 2.5.1: Velocity behaviour in a fluid domain near the wall.

To capture with CFD code those steep gradients close to the wall and to compute then the wall shear stress that derives from them according to Eq. 2.15 [49], a large number of cells is required.

$$\tau_w = \rho\nu \left(\frac{\partial u}{\partial y}\right)_w \tag{2.15}$$

This is due to the fact that in a CFD code only the value of the flow parameters in the centroid of the cell is computed and the variation between the centroid of the cell and the wall is approximated as linear, so to capture the actual variation of the velocity normal to the wall, a large number of cells getting thinner and thinner as approaching the wall is needed, otherwise gradient errors can occur since the calculated velocity gradient $\left(\frac{\partial u}{\partial y}\right)$ is then significantly lower than its true value as shown in Figure 2.5.2. The necessity of large amount of cells close to the wall leads not only to a high computational cost but may also lead to instabilities due to poor cell quality of the cell at the wall. To face these problems, the basic idea of the wall function approach is to substitute the large amounts of thin cells with linear variation accross them with one single larger cell having a non-linear variation between the cell centroid and the wall as shown in Figure 2.5.2.

This non-linear variation function is reported in Figure 2.5.3 [50] and it is the real variation of velocity normal to the wall extracted from experimental measurements of fully developed turbulent flow between two parallel plates. Figure 2.5.3 reports the plot of the dimensionless tangential velocity against the dimensionless distance normal to the wall on linear and logarithmic scales respectively. The equation for y^+ and u^+ are reported in Eq. 2.16 [51] and Eq. 2.17 [51] respectively, taking into consideration the
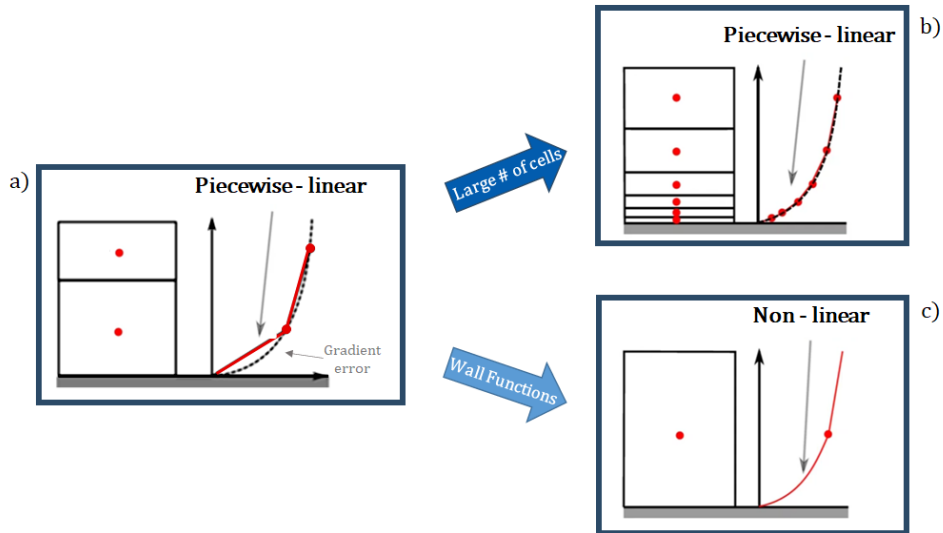
Figure 2.5.2: Possible solutions to the problems due to gradient calculation in CFD. a) Black dashed line: actual velocity profile close to the wall. Red lines: velocity profile close to the wall captured by CFD with large cells at the wall without using the wall function approach. b) Black dashed line: actual velocity profile close to the wall. Red lines: velocity profile close to the wall captured by CFD with small cells at the wall without using the wall function approach. c) Red lines: representation of the idea at the base of the wall function approach.
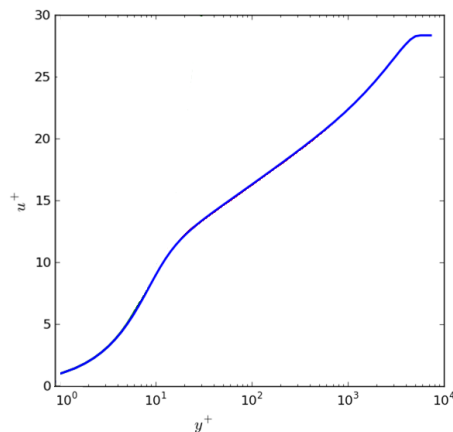
Figure 2.5.3: Real variation of velocity normal to the wall.
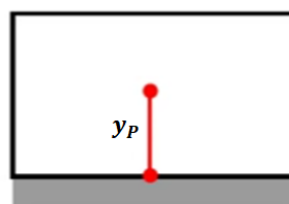
Figure 2.5.4: Cell at the wall with centroid P.

cell at the wall with the centroid in the point P reported in Figure 2.5.4.

$$y^+ = \frac{y_P\, u_\tau}{\nu} \tag{2.16}$$

Where y_P is the normal distance of the centroid of the cell from the wall.

$$u^+ = \frac{u_P}{u_\tau} \tag{2.17}$$

Where u_P is the velocity at the centroid of the cell and u_τ is the friction velocity defined by the Eq. 2.18 [51].

$$u_\tau = \sqrt{\frac{\tau_w}{\rho}} \tag{2.18}$$

The non-linear function in the plot is the variation between the cell centroid and the wall that should be modeled to properly capture the steep gradient of the velocity normal to the wall while avoiding incurring high computational costs due to the use of a large number of cells. Wall functions are the empirical functions that are fitted to the non-linear variation plotted in Figure 2.5.3.

Figure 2.5.5 [50] is again the plot of dimensionless tangential velocity u^+ against dimensionless wall normal distance y^+ with the x-axis on a log scale and the y-axis on a linear scale. The blue solid line shows the actual velocity behaviour close to the wall. The green and red lines show the empirical functions that are used to fit the actual velocity behaviour and they are the wall functions.

As it is possible to see in Figure 2.5.5, the profile is split into four regions.

For y^+ values smaller than five corresponding to the region known as viscous sub-layer, the green profile gives a very good fit to the observed data. It is a linear profile and its mathematical form is reported in Eq. 2.19 [52].

$$u^+ = y^+ \tag{2.19}$$

For y^+ between 30 and 300 [53] corresponding to the region know as inertial sub-layer also called log-law region, the red line gives a very good agreement. It is a logarithmic profile and its mathematical form is reported in Eq. 2.20 [52].

$$u^+ = \frac{1}{\kappa} \log(E y^+) \tag{2.20}$$
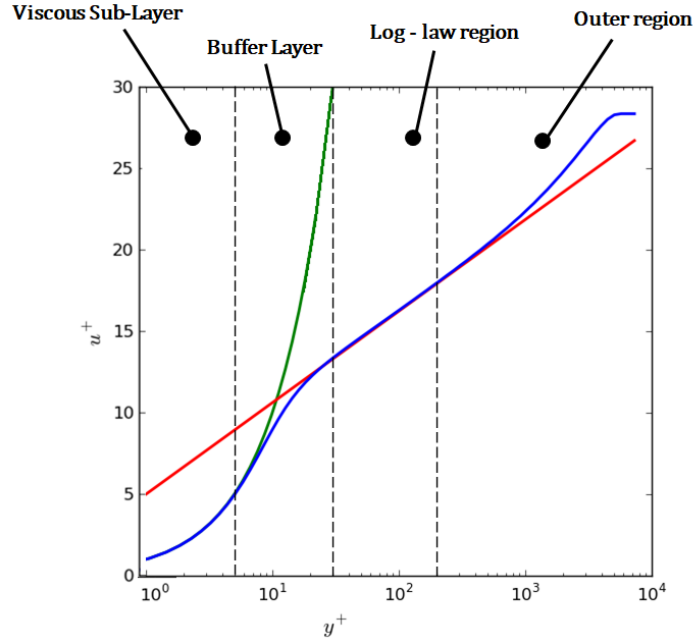
Figure 2.5.5: Real variation of velocity normal to the wall (blue line) fitted with empirical functions (green and red line).

Where κ and E are empirical coefficients equal to 0.4187 and 9.793 respectively [52]. In the buffer layer, in between the viscous sub-layer and the log-law region, the green and red curves give not good agreement with the observed behaviour. The two curves intersect at $y^+ = 11$ [51], so the straightforward approach would be to use a conditional statement reported in Eq. 2.21 [52].

$$u^+ = \begin{cases} y^+, & y^+ < 11 \\ \frac{1}{\kappa}\log(E\,y^+) & y^+ > 11 \end{cases} \tag{2.21}$$

However, this approach can lead to large errors, so in CFD it is generally recommended to not place cells in the buffer layer.

The outer region is of particular interest for this thesis since the meshes used for the simulations presented are really coarse and the y^+ of the first cell at the wall falls in this region. Turbulence shear stress dominates on the laminar scale by two or three orders of magnitude in this area [54]. Due to the deviation of velocity from the free-stream velocity, the velocity defect law can be used in the outer region [55]. However, there is not an established common way to treat the simulations with y^+ falling in the outer region, so in this thesis, an own approach is developed based on the concept of wall function.

From the computational point of view, the wall function approach presented above is

translated into the corrections of the turbulent viscosity at the wall patch faces. As mentioned before, in CFD the velocity variation between the cell centroid and the wall is approximated as linear. The resulting computed wall shear stress for the cell reported in Figure 2.5.4 is expressed as Eq. 2.22 [56].

$$\tau_w = \rho \nu \left(\frac{\partial u}{\partial y} \right)_w = \rho \nu_w \left(\frac{u_P - 0}{y_P} \right) = \rho \nu_w \frac{u_P}{y_P} \qquad (2.22)$$

When the mesh is fine enough near the wall ($y^+ < 5$), the actual variation of the velocity normal to the wall is linear, so the actual wall shear stress coincides with the one of Eq. 2.22. When the mesh is coarse near the wall (y^+ in the log-law region), the actual variation of the velocity normal to the wall is logarithmic, so the actual wall shear stress is expressed as Eq. 2.23 [56].

$$\tau_w = \rho \nu \left(\frac{\partial u}{\partial y} \right)_w = \rho \frac{u_\tau u_P}{\frac{1}{\kappa} \log(Ey^+)} \qquad (2.23)$$

So it seems that using CFD when y^+ falls in the log region, the wall shear stress will be predicted incorrectly since the Eq. 2.22 is different with respect to the Eq. 2.23.

$$\nu_w \frac{u_P}{y_P} = \frac{u_\tau u_P}{\frac{1}{\kappa} \log(Ey^+)} \qquad (2.24)$$

In order to predict the correct wall shear stress with CFD code, the two equations are equated as shown in Eq. 2.24. Dividing both sides by ν and recalling the definition of y^+ reported in Eq. 2.16, the expression for the near wall viscosity is obtained as expressed in Eq. 2.25.

$$\nu_w = \nu \frac{y^+}{\frac{1}{\kappa} \log(Ey^+)} = \nu \frac{y^+}{u^+} \qquad (2.25)$$

y^+ is computed by the code according to Eq. 2.16, ν_w is the near wall viscosity and it is a modified and increased viscosity that allows to obtain the correct wall shear stress even using the linear variation approximation of the velocity across the cell. In CFD code the wall viscosity is expressed as Eq. 2.26 [52].

$$\nu_w = \nu + \nu_t \qquad (2.26)$$

Manipulating the expressions 2.26 and 2.25 is possible to write a conditional statement that allows CFD to switch between the appropriate wall shear stress calculations as

required [56].

$$\nu_t = \begin{cases} 0 & y^+ < 11 \\ \nu \left(\frac{y^+}{\frac{1}{\kappa} \log(E\,y^+)} - 1 \right) & y^+ > 11 \end{cases} \tag{2.27}$$

To summarize, when the mesh is fine enough near the wall ($y^+ < 5$) no modification to the wall viscosity needs to be applied since the linear variation of the flow parameters within the cell foreseen by CFD matches the actual variation of velocity normal to the wall, so the wall shear stress is predicted correctly. When the mesh is coarse near the wall (y^+ in the log-law region) the wall function approach is needed since the linear variation within the cell foreseen by CFD will not capture the actual variation of the velocity normal to the wall. The modification of the wall viscosity is then applied, allowing to obtain a correct prediction of the wall shear stress even with a non-correct velocity gradient.

The wall functions approach is applied to all the flow variables that undergo a steep gradient as approaching the wall.

A really similar formulation of the wall function approach is applied to capture the correct wall heat transfer without using a large amount of cells close to the wall. As in the case of the velocity variation normal to the wall, the temperature gradient normal to the wall is not captured correctly by CFD simulations where not enough cells are used near the wall. So a modified wall thermal diffusivity is introduced to compensate the gradient errors. The mathematical formulation of the final conditional statement that allows CFD to switch between the appropriate wall heat transfer calculations is similar to the Eq. 2.27 since the actual variation of the temperature normal to the wall has an analog behaviour to the one of the velocity in Figure 2.5.3 [57] [58].

The wall function approach is however different when applied to the turbulent statistics, such as k, ε, and ω, because for these cases the wall functions are used to compute directly the values of the turbulence fields [59] [58]. The mathematical expressions of the temperature and turbulent field wall functions will not be investigated further in this thesis while the velocity field wall functions will be the starting point for the methodology developed in this project.

Chapter 3

CFD Software

Nowadays there are several CFD analysis tools on the market. The software chosen to carry out this project is OpenFOAM which stands for "Open-source Field Operation And Manipulation".

OpenFOAM is a free, open-source CFD software written in C++, suite developed by the OpenFOAM Foundation and distributed under the GNU General Public License (GPL). The GPL allows users to alter and redistribute the software while also guaranteeing continuing free usage within the restrictions of the license [60]. OpenFOAM was invented by Henry Weller in 1989 under the name "FOAM" and was published open source as "OpenFOAM" in December 2004 by Henry Weller, Chris Greenshields, and Mattijs Janssens. Since then, OpenFOAM has been controlled and developed, with new versions made available to the public each year [61]. The current version, which was utilized for this thesis, is version 10.

OpenFOAM is a framework for creating application executables that make use of packed functionality found in over 100 libraries. OpenFOAM comes with approximately 250 pre-built applications divided into two categories: solvers, which are each meant to solve a specific issue in fluid or continuum mechanics, and utilities, which are designed to perform data processing tasks. OpenFOAM has pre- and post-processing environments whose interfaces are OpenFOAM utilities. Figure 3.0.1 depicts the general structure of OpenFOAM [62].
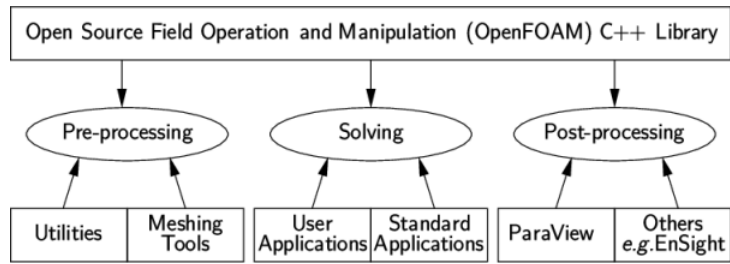
Figure 3.0.1: Overview of OpenFOAM structure.

3.1 Standard Solvers and Utilities

3.1.1 Standard Solvers

The solvers included in OpenFOAM are subdivided into several directories by category of continuum mechanics. The current list of solver categories is reported below with some of the most relevant solvers within them [62].

- 'Basic' CFD codes

    - `laplacianFoam` that solves a simple Laplace equation, e.g. for thermal diffusion in a solid.

- Incompressible flow

    - `boundaryFoam` is a steady-state solver for 1D turbulent flow of incompressible fluids, generally to induce boundary layer conditions at the inlet of the simulation domain.

    - `icoFoam` is a transient solver for incompressible, laminar flow of Newtonian fluids.

    - `pimpleFoam` is a transient solver for turbulent flow of incompressible Newtonian fluids, with optional mesh motion and mesh topology changes.

    - `pisoFoam` is a transient solver for turbulent flow of incompressible fluids, using the PISO algorithm [**PISO**].

    - `simpleFoam` is a steady-state solver for turbulent flow of incompressible fluids, using the SIMPLE algorithm [**SIMPLE**].

- Compressible flow

    - `rhoPimpleFoam` is a transient solver for turbulent flow of compressible

fluids for heating, ventilation, and air conditioning (HVAC) and analogous applications, with optional mesh motion and mesh topology changes.

- `rhoSimpleFoam` is a steady-state solver for turbulent flow of compressible fluids.

- Multiphase flow

    - `interFoam` is a solver using a volume of fluid phase-fraction based interface capturing approach to simulate 2 incompressible, isothermal immiscible fluids. This solver has optional mesh motion and mesh topology changes including adaptive re-meshing.

    - `multiphaseEulerFoam` is a solver to simulate a system of any number of compressible fluid phases with a common pressure, but else separate properties. The type of phase model is run time selectable and can optionally represent multiple species and in-phase reactions. The phase system is also run time selectable and can optionally represent dfferent types of momentun, heat and mass transfer.

- Direct numerical simulation (DNS)

    - `dnsFoam` is a direct numerical simulation solver for boxes of isotropic turbulence.

- Combustion

    - `buoyantReactingFoam` is a solver to simulate combustion with chemical reactions using a density based thermodynamics package with enhanced buoyancy treatment.

- Heat transfer and buoyancy-driven

    - `buoyantFoam` is a solver for steady or transient buoyant, turbulent flow of compressible fluids for ventilation and heat-transfer, with optional mesh motion and mesh topology changes.

- Particle-tracking flows

- Discrete methods

- Electromagnetics

- Stress analysis of solids

  – `solidDisplacementFoam` is a transient solver of linear-elastic, small-strain deformation of a solid body, with optional thermal diffusion and thermal stresses.

- Finance

In all the case studies reported in this thesis, the solver `buoyantFoam` is used.

3.1.2 Utilities

Some of the most relevant utilities used for this project are reported below [62].

- Pre-processing

  – `setFields` that set values on a selected set of cells/patch faces through a dictionary.

- Mesh generation

  – `blockMesh` that is a multi-block mesh generator. It is the most basic meshing tool that comes with OpenFOAM and it is suitable for simple cases but it is not easy to deal with complex geometry.

  – `snappyHexMesh` that is an automatic split hex mesher that can create meshes for objects with triangulated surfaces.

  The mesh can also be created with external meshing software and converted to adapt formats through other specific utilities included in OpenFOAM.

- Mesh manipulation

  – `checkMesh` that checks the validity of a mesh.

- Post-processing

  – `postProcess` that executes the set of `functionObjects` specified in the system/`controlDict` file as it will be described in Section 3.2 or on the command-line for the selected set of times on the selected set of fields.

- Parallel processing

– `decomposPar` that automatically decomposes a mesh and fields of a case for parallel execution of OpenFOAM.

– `reconstructPar` that reconstructs fields of a case that is decomposed for parallel execution of OpenFOAM.

3.2   Case structure

To run a case study in OpenFOAM, the user needs to assign a name to the case that then will be the name of the directory in which all the case files and subdirectories required to run the application are stored. The basic directory structure of an OpenFOAM case is shown in Figure 3.2.1 [62].
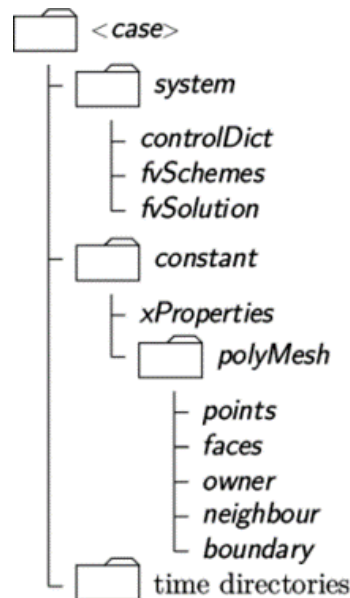
Figure 3.2.1: Basic directory structure of an OpenFOAM case.

3.2.1   `system` directory

The `system` directory is used to set the parameters associated with the solution procedure of the simulation.   It contains at least the three mandatory files: `controlDict`, `fvSchemes` and `fvSolution`. In addition, other files may be included as well, for example if the `blockMesh` tool is being used to generate the mesh a `blockMeshDict` file would be required to specify the parameters of the mesh. Additional files may also be included to control runtime post-processing activities [63]. The `controlDict` file is where run control parameters are specified such as the

solver chosen to run the simulation, the start/end time, the timestep, how often to write solution data, as well as more advanced items such as function objects that should be executed at runtime. The `fvSchemes` file is where all necessary information related to the discretization schemes for the finite volume method are specified such as time discretization scheme, gradient/Laplacian terms discretization scheme, and interpolation scheme. The `fvSolution` file is where to specify how the discretized equations are to be solved. In this file, the list of linear solvers that are used to solve each equation, tolerances and other algorithm controls like relaxation factors are set [63].

Mesh generation with `blockMesh`

Decomposing the domain geometry into a collection of one or more three-dimensional, hexahedral blocks is the fundamental idea behind `blockMesh`. The block edges can be splines, arcs, or straight lines. Each block of the domain is defined by 8 vertices, one at each corner of a hexahedron. The `system` directory of a case contains a dictionary file called `blockMeshDict` that is used to generate the mesh [30]. Generally, the `blockMeshDict` gives the information about:

- vertices

- edges

- blocks

- boundary

All the vertices of the mesh are written in a list of vertex coordinates. Two vertices are connected by an edge that is assumed to be straight by default. If the edge is an arc or spline, it has to be specified in the `blockMeshDict`. The blocks are defined in a list of block definitions. Each block definition includes a list of vertex labels in a specific order defining the corners of the block, a vector indicating the number of cells in which the block needs to be split in each direction, and a list of cell expansion ratios for each direction. The expansion ratio is the ratio between the width of the end cell along one edge of the block and the width of the start cell along that edge. The mesh can be graded, or refined, in specific directions thanks to the expansion ratio [30]. The boundary of the mesh is also described in the `blockMeshDict`. As mentioned in Section 2.3, the domain mesh boundary is broken into patches on which the boundary

conditions are applied. Each patch is described in the `blockMeshDict` with its unique name, its type which can be a generic patch or a wall patch, and a list of block faces that make up the patch. Each block face is defined by a list of 4 vertex numbers [30]. The `blockMesh` utility reads the `blockMeshDict` file, generates the mesh, and writes out points and faces, cells, and boundary files in the `polyMesh` subdirectory that is introduced in the following subsection.

3.2.2 `constant` **directory**

The `constant` directory contains the specifications of the physics of the problem collected in files, including the mesh and any physical properties that are required for the solver. It will always contain a subdirectory called `polyMesh` which contains a full description of the case mesh and which is not written by the user but created by a meshing utility such as `blockMesh` and `snappyHexMesh`. The constant directory normally contains other files that are solver-specific, like `trasnportProperties` and `turbulenceProperties` [63].

Turbulence modeling in OpenFOAM

The `turbulenceProperties` file is included in `constant` directory every time a simulation involves turbulence modeling. In the file, the type of turbulence modeling to be used is selected by the keyword `simulationType` and the input accepted in OpenFOAM are [62]:

- `laminar` that uses no turbulence models.

- `RAS` that uses Reynolds-averaged stress modeling described in Section 2.4 of Chapter 2.

- `LES` that uses large-eddy simulation or detached-eddy simulation modeling described in Section 2.4 of Chapter 2.

As already mentioned in Chapter 2, in all the simulations reported in this thesis, the RAS turbulence modeling is used. OpenFOAM includes RAS turbulence closures based on linear and non-linear eddy viscosity models and Reynolds stress transport models. As mentioned previously, for this thesis the model used is in the category of the linear eddy viscosity models and it is called relaizable k-ε model (`realizableKE`).

3.2.3 Time directories

The time directories contain individual files of data for particular fields such as velocity and pressure. One of the time directories is the 0 directory in which the data stored are the initial conditions and the boundary conditions. This directory is user specified to define the problem [62]. Inside of the 0 directory there is one text file for each field that is required for the particular solver executable that is being run, for example, U for velocity, p for pressure, etc. The remaining directories contain the solution fields written by OpenFOAM as output at specific times during the simulation. The name of these directories is the numerical value of the simulation time at which the data are given as output and the frequency of output is controlled by the `controlDict` file [63].

3.3 Wall functions

The type of wall functions used for the flow fields in a simulation is specified in the text file of each field in the 0 directory as boundary conditions on the wall patches. In OpenFOAM, the wall functions directory for velocity and turbulence fields is located in the path `$FOAM_SRC/MomentumTransportModels/momentumTransportModels/derivedFvPatchFields/wallF` In `wallFunctions` directory there are six types of wall function sub-directories [64]:

- `epsilonWallFunctions`

- `kqRWallFunctions`

- `omegaWallFunctions`

- `fWallFunctions`

- `v2WallFunctions`

- `nutWallFunctions`

The wall functions directory for the temperature fields are located in the path `$FOAM_SRC/ThermophysicalTransportModels/derivedFvPatchFields/alphatWallFunctions`. In `alphatWallFunctions` directory there are two types of wall functions:

- `alphatJayatillekeWallFunction`

- `alphatWallFunction`

In this section the different types of wall functions available in OpenFOAM will be briefly described, more attention will be devoted to the sub-directory `nutWallFunctions` since it will be the starting point for the methodology presented in Chapter 4.

3.3.1 `kqRWallFunctions`

In the `kqRWallFunctions` the wall functions for the turbulent kinetic energy k are stored. There are two kinds of wall functions for k:

- `kqRWallFunction`

- `kLowReWallFunction`

The first provides a pure zero-gradient boundary condition on the patches where it is applied and it is adapted for high-Reynolds number turbulent flow cases. The latter provides a turbulence kinetic energy boundary condition for low- and high- Reynolds number turbulent flow cases based on the position of y^+ [64].

3.3.2 `epsilonWallFunctions`

In `epsilonWallFunctions` the wall functions for the dissipation rate of the turbulent kinetic energy ε are stored. There are two kinds of wall functions for ε:

- `epsilonWallFunction`

- `epsilonLowReWallFunction`

Both provide a boundary condition for the dissipation rate with the difference that the condition of the second type depends on the position of y^+ [64].

3.3.3 `omegaWallFunctions`

`omegaWallFunctions` provide the constraint on turbulence specific dissipation rate ω [30].

3.3.4 `fWallFunctions`

`fWllfunctions` provides a conditional statement for a function used in the low-Re k-ε turbulence models, called damping function [30], for turbulence flow cases based on the position of the y^+ [64].

3.3.5 `v2WallFunctions`

`v2WallFunctions` provide the stress normal to streamlines boundary condition based on the position of the y^+ [64].

3.3.6 `nutWallFunctions`

In `nutWallFunctions` directory seven kinds of turbulence viscosity wall boundary conditions are provided.

- `nutWallFunction` is an abstract class that provides Dirichlet boundary condition.

- `nutLowReWallFunction` simply set the turbulence viscosity to zero.

- `nutkWallFunction` provides a turbulence viscosity condition based on the turbulence kinetic energy. It is exactly the CFD implementation of the Eq. 2.13.

- `nutUWallFunction` provides a turbulence viscosity condition based on the velocity. It has the same mathematical formulation of the `nutkWallFunction` differing only in the calculation of the y^+ in the code since for `nutkWallFunction` y^+ is computed through the turbulent kinetic energy and for `nutUWallFunction` through the velocity.

- `nutUSpaldingWallFunction` uses a continuous wall function [65] to fit the actual variation of the velocity normal to the wall in the viscous sub-layer and log region, resulting in a special relationship between y^+ and u^+ [30].

- `nutkRoughWallFunction` inherits the traits of the `nutkWallFunction` boundary condition manipulating the wall roughness parameter E to account for roughness effects [66].

- `nutURoughWallFunction` inherits the traits of the `nutWallFunction` boundary condition.It provides a wall boundary condition to the turbulent viscosity based on velocity for low- and high-Reynolds number turbulence models for rough

walls [67].

The mathematical formulation of the wall function implemented in CFD as `nutkWallFunction` will be used in this thesis as starting point to develop a new wall function that will take into account the use of a coarse-grid approach. Furthermore, all the test cases presented are performed first with the original `nutkWallFunction` and then with the new wall function developed for comparison. The newly developed methodology will be described in detail in the following chapter.

3.3.7 `alphatJayatillekeWallFunction`

The `alphatJayatillekeWallFunction` provides a thermal wall function for turbulent thermal diffusivity based on the Jayatilleke model [68] [69].

3.3.8 `alphatWallFunction`

The `alphatWallFunction` provides a turbulent thermal diffusivity boundary condition when using the wall function approach for the velocity field [70].

Chapter 4

Method

As already mentioned in Chapter 1, the main goal of this thesis is to develop an innovative solution in thermo-hydraulic analysis that exploit the capabilities of sub-channel codes and CFD methods while overcoming their limitations. The methodology developed in this project falls into the category of coarse grid CFD method approaching the methodology presented by Liu et al. [7] as regards the exploitation of empirical correlations instead of well-resolved CFD data, but departing from the existing approaches of the category by not using additional momentum source terms in the governing equations. In the methodology, a very coarse mesh will be implemented in the CFD software OpenFOAM and a new wall treatment, based on the concept of the wall function, will be applied to the cells at the wall to take into account the low resolution of the grid which does not allow to effectively capture the effect of the solid wall on the thermo-hydraulics of the flow.

In this section, the methodology adopted to reach the goals mentioned in Section 1.2 will be presented. Section 4.1 will be focused on the derivation of the wall function that is implemented in the test cases described in Section 4.2. In Section 4.3, Section 4.4, and Section 4.5, the specifications of the test cases analyzed in this thesis are briefly described. Section 4.6 will focus on the derivation of the 1D analytical pressure profiles with which the CFD results will be compared.

4.1   Wall Treatment

As mentioned before, the methodology developed for this project can be categorized as coarse-grid CFD analysis. The problems with very coarse meshes involved in the

coarse-grid CFD approach are:

1. Coarse meshes do not respect the high mesh density requirement reported in Section 2.3.

2. Coarse meshes will not capture the actual variation of the flow parameters normal to the wall for the reasons explained in Section 2.5.

The idea of the method presented is to face at least one of these problems, the second one. The starting point is the concept of wall function which, in the case of the velocity field for example, attempts to circumvent the need for a large number of cells at the wall to properly capture the velocity gradient normal to the surface by modifying the wall viscosity to obtain finally the correct wall shear stress. This approach is applied when the distance of the centroid of the first cell facing the wall from the wall itself falls into the range of y^+ corresponding to the log-law region. With the very coarse meshes required by the coarse grid CFD analysis, the distance of the centroid of the first cell facing the wall from the wall itself falls into the range of y^+ corresponding to the outer region of which there is no common and well-known wall function to fit the actual variation of the velocity normal to the wall. Consequently, a new approach needs to be developed.

As mentioned in Section 2.5, in CFD, the velocity variation between the cell centroid and the wall is approximated as linear, as a result the computed wall shear stress for a cell with centroid in point P is reported in Eq. 2.22. The idea of the developed methodology is to equate this wall shear stress to the one computed in 1D analysis which is reported in Eq. 4.1 [71].

$$\tau_w = \rho \nu \left(\frac{\partial u}{\partial y} \right)_w = \frac{1}{2} \rho C_f U_{avg}^2 \tag{4.1}$$

U_{avg} is the average velocity on the cross-sectional flow area at each axial position in which the 1D domain is discretized. C_f is the Fanning friction factor [72] and it is defined as the ratio of the shear stress τ_w on the bounding walls of the channel to the kinetic energy of the fluid defined as $\frac{1}{2} \rho U_{avg}^2$ [71].

$$\rho \nu_w \frac{u_P}{y_P} = \frac{1}{2} \rho C_f U_{avg}^2 \tag{4.2}$$

Equating Eq. 2.22 and 4.1 the obtained expression is reported in Eq. 4.2. Dividing both sides of Eq. 4.2 by ν, the expression reported in Eq. 4.3 is obtained.

$$\frac{\nu_w}{\nu} = \frac{1}{2} C_f \frac{y_P}{\nu} \frac{U_{avg}^2}{u_P} \tag{4.3}$$

Substituting the definitions of y^+ Eq. 2.16 in Eq. 4.3 and expressing u_P in function of u^+ and u_τ according to Eq. 2.17, the expression for the wall viscosity ν_w reported in Eq. 4.4 is obtained.

$$\nu_w = \nu \frac{1}{2} \frac{y^+}{u^+} C_f \left(\frac{U_{avg}}{u_\tau} \right)^2 \tag{4.4}$$

Recalling the expression in Eq. 2.26 and manipulating it with Eq. 4.4, it is possible to write a new conditional statement that allows CFD to switch between the appropriate wall shear stress calculations as required.

$$\nu_t = \begin{cases} 0 & y^+ < 11 \\ \nu \left(\frac{y^+}{\frac{1}{\kappa} \log(E y^+)} - 1 \right) & 11 < y^+ < 300 \\ \nu \left(\frac{1}{2} \frac{y^+}{u^+} C_f \left(\frac{U_{avg}}{u_\tau} \right)^2 - 1 \right) & y^+ > 300 \end{cases} \tag{4.5}$$

u^+ is computed according to Eq. 2.17 where both the velocity in the centroid of the cell at the wall u_P and the friction velocity u_τ are computed by the code. u_τ is computed according to Eq. 4.6 [73].

$$u_\tau = C_\mu^{\frac{1}{4}} k^{\frac{1}{2}} \tag{4.6}$$

C_μ is the empirical model constant. The turbulent kinetic energy k is computed by the code in each cell at the wall. The local kinematic viscosity ν is computed by the code as well as the dimensionless distance of the centroid of the cell from the wall y^+. y^+ is computed according to Eq. 2.16. The friction factor C_f is dependent on Reynolds number and it is imposed to be computed by the code according to the empirical correlation reported in Eq. 4.7 [71].

$$C_f = \frac{0.046}{Re^{0.2}} = \frac{0.046}{\left(\frac{U_{avg} D_h}{\nu} \right)^{0.2}} \tag{4.7}$$

The hydraulic diameter value D_h is given in input when applying the wall function as boundary condition for the turbulent viscosity on the wall patches giving then the opportunity to the user to switch between different values of hydraulic diameter

depending on the wall patches being treated while the average velocity U_{avg} is imposed as constant and equal to the value u_{IN} inside the script describing the modified wall function for the turbulent viscosity not giving the possibility to be modified without having to compile again during the simulation the library where the modified wall function is stored. The assumption of constant average velocity on each cross-sectional flow area along the channel is made for the preliminary analysis reported in this thesis due to the complexity of computing the average value of the velocity at each layer of cells during the simulation with OpenFOAM, but it should eventually be generalized for future investigations of the method. To make the constant average velocity assumption as correct as possible at least for the test cases in which the cross-sectional area of the flow does not change along the channel, the density is assumed to be constant in the channel disregarding the dependence on the temperature. For one of the test cases, Test Case 4, which will be described in the following section, the assumption of constant average velocity along the channel is not correct and a different solution has to be found for future investigations of the methodology presented since the assumption can cause large errors.

Furthermore, the method developed will be applied in this project only to compute the wall shear stress, regarding the temperature field, the wall function approach based on the log-law explained in Section 2.5 will be implemented. In future investigations, a modification similar to the one applied to the turbulent viscosity shown in Eq. 4.5 could be developed for the turbulent thermal diffusivity to extend the approach also to correctly predict the wall heat transfer.

Being an innovative approach, during the simulations aimed at testing the developed methodology, several problems emerged in the obtained results as will be described in detail in Chapter 5. As a result, the development process has become an iterative process of which only the most relevant version has been described in the current chapter, and the results of which will be reported in the next chapter.

4.2 Case Studies

In this Section, the four case studies implemented in the project are presented. The four test cases are:

- Test Case 1 : single-phase flow in a pipe.

- Test Case 2 : single-phase flow in the sub-channel of a PWR.

- Test Case 3 : single-phase flow in the sub-channel located in the corner of a fuel assembly of a PWR.

- Test Case 4 : single-phase flow in the 2x2 fuel bundle of a PWR.

4.2.1 Pipe

The first case study, Test Case 1, is a very simple case, a single-phase fluid flowing in a pipe with diameter d and length L. The geometry of the test case is reported in Figure 4.2.1. For computational reasons, two adiabatic layers are inserted at the beginning

| (a) Pipe geometry | (b) Pipe cross-section |
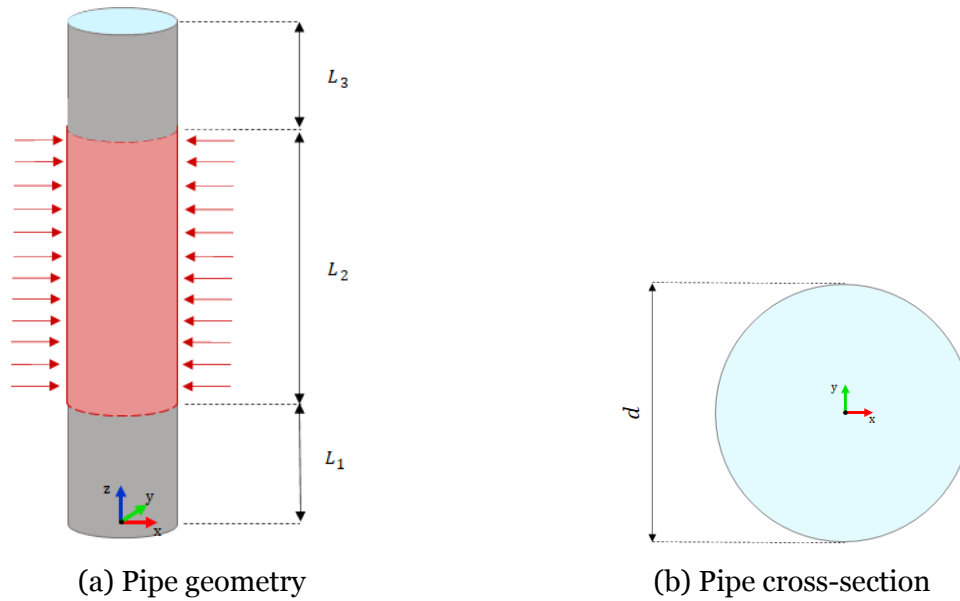
Figure 4.2.1: Geometry of the pipe: a) pipe geometry and b) cross-section of the pipe

and at the end of the pipe, so the total pipe is divided into three layers of length L_1, L_2, and L_3. A uniform heat flux q'' is applied on the lateral surface of the pipe in the layer of length L_2. The fluid simulated is water and it is assumed to enter the pipe with uniform inlet velocity profile of magnitude u_{IN} and inlet temperature T_{IN}. The outlet pressure of the fluid is assumed to be equal to p_{OUT}. Being a circular pipe the hydraulic diameter D_h [74] is equal to the diameter of the pipe d. The test case data are reported in Table 4.2.1.

4.2.2 Single sub-channel

The second test case, Test Case 2, is a single-phase fluid flowing in the sub-channel of a PWR [75] with pitch pit, fuel rod diameter d_{rod} and channel lenght L. The geometry of the test case is reported in Figure 4.2.2. As for the previous test case, for computational

Data	
d	12 mm
D_h	12 mm
L	5000 mm
L_1	1000 mm
L_2	3000 mm
L_3	1000 mm
u_{IN}	8 m/s
T_{IN}	290 °C
p_{OUT}	155 bar
q''	4.24×10^5 W/m^2
Re	$7.75 \cdot 10^5$
C_f	0.0031

Table 4.2.1: Data of test case of single-phase fluid flow in a pipe.

(a) Sub-channel geometry

(b) Sub-channel cross-section
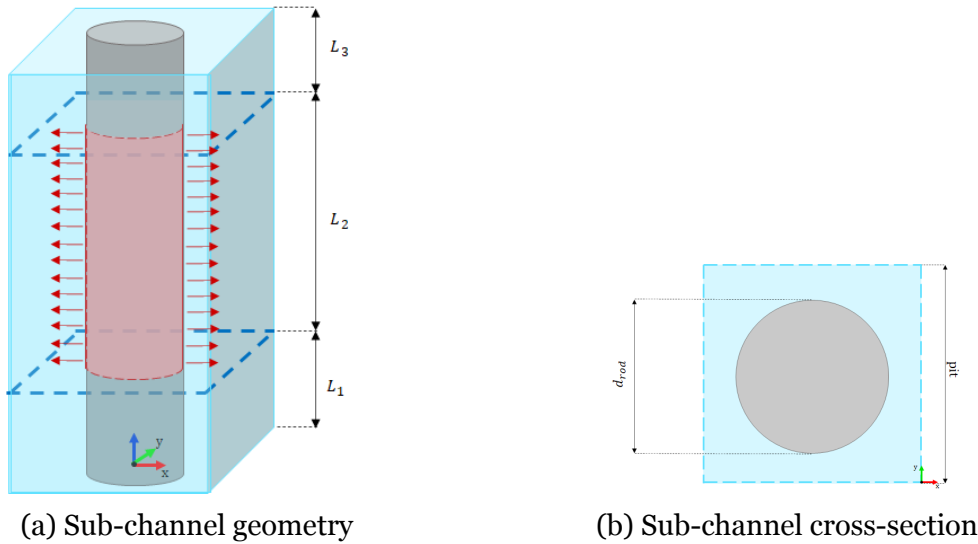
Figure 4.2.2: Geometry of the sub-channel of a PWR: a) sub-channel geometry and b) cross-section of the subchannel

reasons, two adiabatic layers are inserted at the beginning and at the end of the sub-channel, so the total channel is divided into three layers of length L_1, L_2, and L_3. The power generated in the fuel rod is assumed to be equal to q and it is translated as a uniform heat flux boundary condition on the fluid flowing in the sub-channel in the layer of length L_2. The fluid simulated is water and it is assumed to enter the sub-channel with a uniform inlet velocity profile of magnitude u_{IN} and inlet temperature T_{IN}. The outlet pressure of the fluid is assumed to be equal to p_{OUT}. The hydraulic diameter D_h [74] is computed according to the expression in Eq. 4.8 [74].

$$D_h = \frac{4A}{P} \tag{4.8}$$

Where A is the cross-sectional area of the flow and P is the wetted perimeter of the cross-section. For this test case, the cross-sectional area of the flow is reported in Figure 4.2.2b and the hydraulic diameter is computed according to the expression in Eq. 4.9

$$D_h = 4\frac{\left(pit^2 - \pi\frac{d_{rod}^2}{4}\right)}{\pi d_{rod}} \tag{4.9}$$

The test case data are reported in Table 4.2.2.

Data	
d_{rod}	$9.5\ mm$
pit	$12.6\ mm$
D_h	$11.8\ mm$
L	$6158\ mm$
L_1	$1500\ mm$
L_2	$3658\ mm$
L_3	$1000\ mm$
u_{IN}	$4\ m/s$
T_{IN}	$280\ °C$
p_{OUT}	$155\ bar$
q	$46300\ W$
q''	$4.24 \times 10^5\ W/m^2$
Re	$3.74 \cdot 10^5$
C_f	0.0035

Table 4.2.2: Data of test case of a single-phase fluid flow in the sub-channel of a PWR.

4.2.3 Single sub-channel with solid walls on two edges

The third test case, Test Case 3, differs from the second one just for the presence of adiabatic solid walls on two edges of the sub-channel. In this case, the sub-channel is located in a hypothetical corner of the fuel assembly of a PWR, so it has two solid walls in the right and bottom edges. The geometry of the test case is reported in Figure 4.2.3. As for the previous test cases, for computational reasons, two adiabatic layers are inserted at the beginning and at the end of the sub-channel, so the total channel is divided into three layers of length L_1, L_2, and L_3. The power generated in the fuel rod is assumed to be equal to q and it is translated as a uniform heat flux boundary condition on the fluid flowing in the sub-channel in the layer of length L_2. The fluid simulated is water and it is assumed to enter the sub-channel with a uniform inlet velocity profile of magnitude u_{IN} and inlet temperature T_{IN}. The outlet pressure of the fluid is assumed to be equal to p_{OUT}. For this test case, the cross-sectional area of the flow is reported

(a) Sub-channel geometry

(b) Sub-channel cross section

Figure 4.2.3: Geometry of sub-channel with solid walls on two edges: a) sub-channel geometry and b) cross-section of the sub-channel

in Figure 4.2.3b and the hydraulic diameter is computed according to the expression in Eq. 4.10

$$D_h = 4 \frac{\left(pit^2 - \pi \frac{d_{rod}^2}{4}\right)}{\pi d_{rod} + 2pit} \qquad (4.10)$$

The test case data are reported in Table 4.2.3.

Data	
d_{rod}	9.5 mm
pit	12.6 mm
D_h	6.4 mm
L	6158 mm
L_1	1500 mm
L_2	3658 mm
L_3	1000 mm
u_{IN}	4 m/s
T_{IN}	280 °C
p_{OUT}	155 bar
q	46300 W
q''	4.24×10^5 W/m^2
Re	$2.03 \cdot 10^5$
C_f	0.0040

Table 4.2.3: Data of test case of a single-phase fluid flow in a sub-channel located in the corner of a fuel assembly in a PWR .

4.2.4 2x2 Fuel bundle with three full-length pins and one half-length pin

The final test case, Test Case 4, is a single-phase fluid flowing in the 2x2 fuel bundle of a PWR [75] having three full-length pins and one pin of half channel length. The geometry of Test Case 4 is selected to test the new methodology in problems where secondary flows are present. The geometry is reported in Figure 4.2.4. As for the

(a) 2x2 Fuel bundle geometry

(b) 2x2 Fuel bundle cross-section for the first half of the channel

(c) 2x2 Fuel bundle cross-section for the second half of the channel
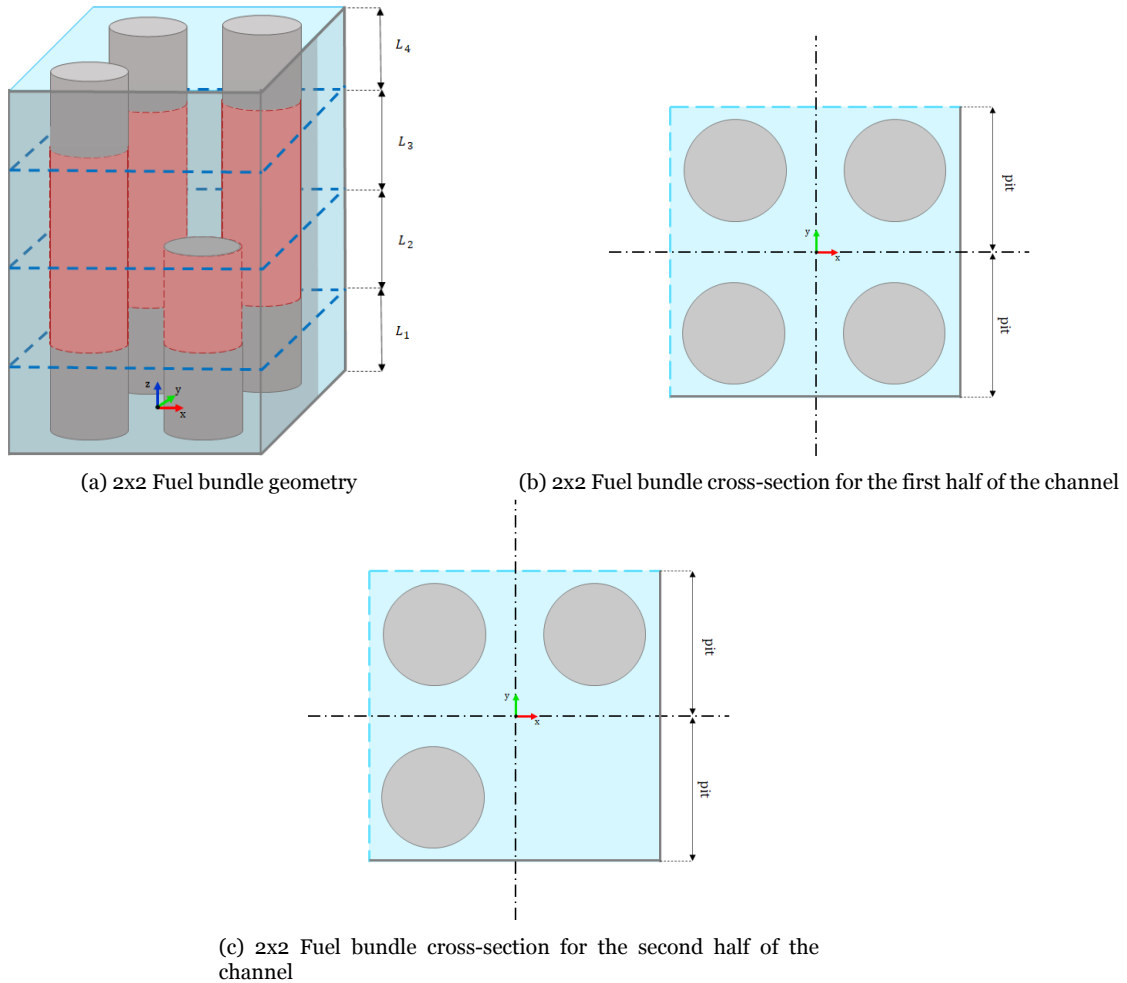
Figure 4.2.4: Geometry of 2x2 fuel bundle: a) fuel bundle geometry, b) cross-section of the fuel bundle for the first half of the channel, and c) cross-section of the fuel bundle for the second half of the channel

previous test cases, for computational reasons, two adiabatic layers are inserted at the beginning and at the end of the fuel bundle, so the total length is divided into four layers of length L_1, L_2, L_3, and L_4. The power generated in the full-length fuel rod is assumed to be equal to q and it is translated as a uniform heat flux boundary condition on the flowing fluid facing the three full-length pins in the layers of length L_2 and L_3. The power generated in the half-length fuel rod is assumed to be equal to half of the power

generated in the full-length pin and it is translated as a uniform heat flux boundary condition on the flowing fluid facing the half-length rod in the layer of length L_2. The fluid simulated is water and it is assumed to enter the fuel bundle with a uniform inlet velocity profile of magnitude u_{IN} and inlet temperature T_{IN}. The outlet pressure of the fluid is assumed to be equal to p_{OUT}. For 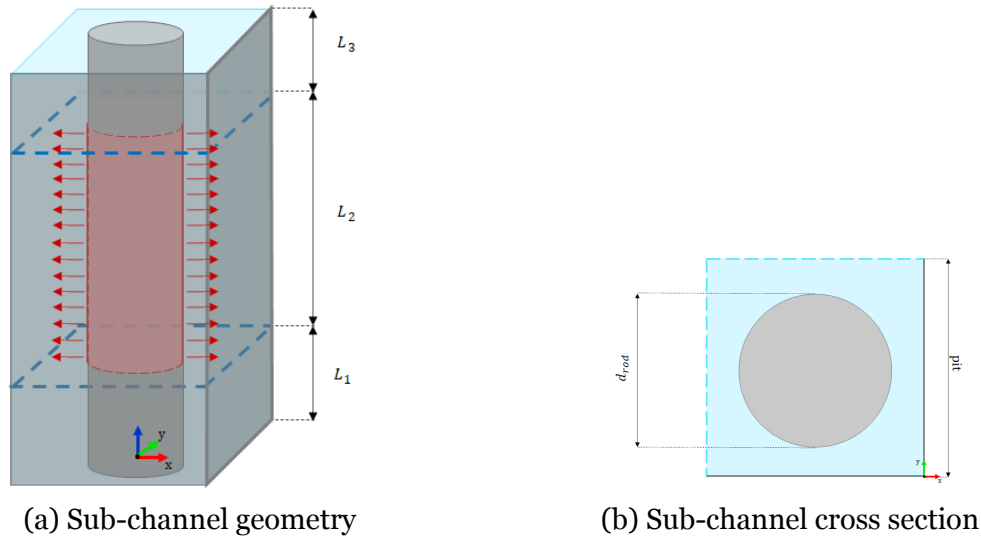this test case, the cross-sectional area of the flow for the first half of the channel and for the second half of the channel are reported in Figure 4.2.4b and Figure 4.2.4c respectively. The fuel bundle is treated as four adjacent sub-channels across which the flow is free to flow. The hydraulic diameter of each sub-channel is computed separately according to the cross-sectional areas of the flow reported in Figure 4.2.5 and Figure 4.2.6 for the first and the second half of the channel respectively.

(a) Sub-channel 1.　　(b) Sub-channel 2.　　(c) Sub-channel 3　　(d) Sub-channel 4.
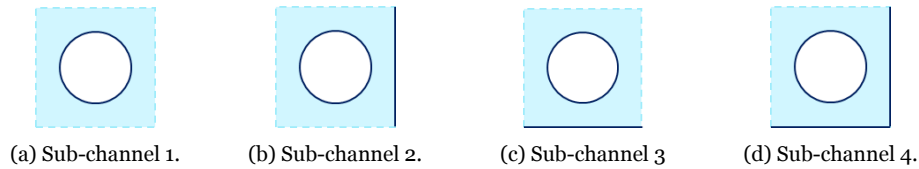
Figure 4.2.5: Cross-sectional flow area of the sub-channels that make up the 2x2 fuel bundle in the first half of the channel. a) cross section of sub-channel 1. b) cross section of sub-channel 2. c) cross section of sub-channel 3. d) cross section of sub-channel 4.

In the first half of the channel the hydraulic diameter of the sub-channel in the top-left of the fuel bundle, identified as sub-channel 1, is computed according to the expression reported in Eq. 4.9 and the hydraulic diameter of the sub-channel in the top-right of the fuel bundle, identified as sub-channel 2, is computed according to the expression reported in Eq. 4.11.

$$D_h = 4 \frac{\left(pit^2 - \pi \frac{d_{rod}^2}{4} \right)}{\pi d_{rod} + pit} \tag{4.11}$$

In the first half of the channel the hydraulic diameter of the sub-channel in the bottom-left of the fuel bundle, identified as sub-channel 3, is computed according to the expression reported in Eq. 4.11 and the hydraulic diameter of the sub-channel in the bottom-right of the fuel bundle, identified as sub-channel 4, is computed according to the expression reported in Eq. 4.10.

In the second half of the channel the hydraulic diameters of the sub-channel 1, sub-channel 2 and sub-channel 3 do not change with respect to the first half of the channel. Instead, the hydraulic diameter of the sub-channel 4 in the second half of the channel,

(a) Sub-channel 1.   (b) Sub-channel 2.   (c) Sub-channel 3.   (d) Sub-channel 4.   (e) Top of the half-length rod.
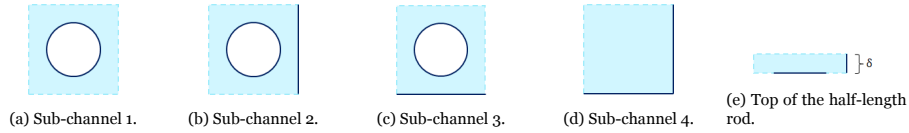
Figure 4.2.6: Cross-sectional flow area of the sub-channels that make up the 2x2 fuel bundle in the second half of the channel. a) cross section of sub-channel 1. b) cross section of sub-channel 2. c) cross section of sub-channel 3. d) cross section of sub-channel 4. e)Assumed cross-sectional area of the flow just above the top of the half-length rod.

is computed according to the expression reported in Eq. 4.12.

$$D_h = 2pit \tag{4.12}$$

The top of the rod is seen by the fluid as a wall on which to flow, consequently, the new wall function approach developed must also be applied to the patch corresponding to the top of the rod. In order to apply the new wall function method, an hydraulic diameter has to be given as input. To compute the hydraulic diameter, it is assumed that the fluid flows horizontally in a small layer of arbitrary thickness δ on the top of the rod, the flow passage is assumed to be the cross-sectional area shown in Figure 4.2.6e and the average velocity is assumed to be equal to u_{IN}. According to this assumption, the hydraulic diameter given in input to implement the new wall function approach on the patch corresponding to the top of the half-length rod is computed according to Eq. 4.13.

$$D_h = 4\frac{pit\,\delta}{d_{rod} + \delta} \tag{4.13}$$

This assumption is made for the preliminary analysis reported in this thesis, other solutions should be found for future investigations, for example computing the hydraulic diameter using the 3D geometry or directly using the standard wall function approach using a slightly axially refined mesh since the correlation implemented in the new wall function approach is not suitable for the flow scenario on the top surface of the rod. The test case data are reported in Table 4.2.4.

4.3   0 directory

All the initial and boundary conditions mentioned in the previous section are specified for all the test cases analyzed in the 0 directory. The `noSlip` boundary condition

Data	
d_{rod}	9.5 mm
pit	12.6 mm
δ	1 mm
D_h	sub-channel 1 11.8 mm sub-channel 2 8.3 mm sub-channel 3 8.3 mm sub-channel 4 first half of the channel 6.4 mm sub-channel 4 second half of the channel 25.2 mm fluid flowing on the top of the half-length rod 4.8 mm
L	6158 mm
L_1	1500 mm
L_2	1829 mm
L_3	1829 mm
L_4	500 mm
u_{IN}	4 m/s
T_{IN}	280 ºC
p_{OUT}	155 bar
q	46300 W
q''	4.24×10^5 W/m^2
Re_1	$2.63 \cdot 10^5$
Re_2	$3.19 \cdot 10^5$
$C_{f,1}$	0.0038
$C_{f,2}$	0.0036

Table 4.2.4: Data of test case of a single-phase fluid flow in the 2x2 fuel bundle of a PWR .

is applied to the velocity field at each wall patch present in the domains. The uniform inlet velocity profile is imposed on the inlet patch with `fixedValue` boundary condition and the initial value of velocity is imposed to be equal to u_{IN} of the different test cases. The outlet pressure is imposed with `fixedValue` boundary condition on the outlet patch. The external constant heat flux is imposed on the heated layers through the boundary condition `externalWallHeatFluxTemperature`, while in the adiabatic boundary layers the boundary condition `zeroGradient` is imposed to the temperature field. The initial value of the temperature field is assumed to be equal to T_{IN} of the different test cases. The modification to the turbulent kinematic viscosity is applied through the `nutkWallFunction` boundary condition on the wall patches. The standard modification of the turbulent kinematic viscosity contained in the `nutkWallFunction` script described by Eq. 2.27 is substituted by the conditional statement reported in Eq. 4.5. On the same patches where the `nutkWallFunction` is applied also the boundary conditions `kqRWallFunction`, `epsilonWallFunction`, and

`alphatJayatillekeWallFunction` based on the standard wall function approach need to be applied to the turbulent kinetic energy, its dissipation rate and the turbulent thermal diffusivity respectively. The initial values for the turbulent kinetic energy and the energy dissipation rate are imposed according to the Eq. 4.14 and Eq. 4.15 respectively [76].

$$k = \frac{3}{2} \left(u_{IN} I \right)^2 \tag{4.14}$$

I is the initial turbulent intensity and it is assumed to be equal to 5%.

$$\varepsilon = C_\mu^{\frac{3}{4}} k^{\frac{3}{2}} l^{-1} \tag{4.15}$$

C_μ is a k-epsilon model parameter typically given as 0.09 [30] and l is the turbulent length scale and it is assumed to be equal to half channel length. The initial values of the turbulent thermal diffusivity and the turbulent kinematic viscosity are set to zero.

4.4 `constant` **directory**

The `constant` directories of the test cases analyzed are made of three files and the `polyMesh` folder which is created directly by OpenFOAM after running the `blockMesh` utility. One file specifies the gravitational acceleration vector. The other file specified the turbulence model category chosen and the turbulence model implemented for the simulation, in all the test cases the turbulence model category is `RAS` and the turbulence model used is the realizable k-epsilon model set with the keyword `realizableKE`. In the last file, the physical properties and the thermophysical model used for the simulation of the problems analyzed are specified. For the test cases the thermophysical model chosen is `heRhoThermo` [62] which is a model for flow with fixed composition based on density. The dynamic viscosity, the Prandtl number, and the heat capacity are assumed constant. The density is assumed constant in the whole geometry domain for all the test cases. The thermophysical properties of the water are computed with XSteam using the inlet temperature and the outlet pressure values.

4.5 `system` **directory**

In the `system` directories of the test cases the `blockMeshDict` file is contained where all the information to build the mesh domain are stored. The solver chosen for the

simulations is `buoyantFoam`, and the time step is adjusted during the simulations through the keywords `adjustTimeStep` according to the maximum Courant number imposed as 0.9. The time discretization scheme used for all the test cases is the implicit Euler scheme set with the keyword `Euler` in the `fvSchemes` file where also the schemes for the discretization of the differential operators are specified. In the `fvSolution` file the solvers used to solve each equation and the tolerances are set, for all the test cases the PIMPLE algorithm is chosen. PIMPLE algorithm combines pressure and velocity coupling algorithms and forces the equations to be solved using variables updated within the time step [30].

4.6   Analytical pressure profile

The pressure drop across a channel is the result of the wall shear stress acting along the surface of the channel against the direction of the flow [77]. Given the close relation between pressure drop and wall shear stress, to understand if the implemented methodology gives results of wall shear stress at least as good as the sub-channel code ones, the axial pressure profiles obtained from the simulations of the test cases described in section 4.2 will be compared with the empirical-based 1D axial pressure profiles that reflect well how pressure drops are actually calculated in a sub-channel code. The latter will be identified as analytical pressure profiles in this thesis. This section will be dedicated to the mathematical formulations of the analytical pressure drops for the four test cases simulated for this project.

4.6.1   Pipe

The total analytical pressure drop across the pipe in the test case described in Subsection 4.2.1 is computed according to the Eq. 4.16 [1].

$$\Delta p = \Delta p_{fric} + \Delta p_{grav} = f \frac{L}{d} \rho \frac{U_{avg}^2}{2} + \rho g L \tag{4.16}$$

f is the Darcy-Weisbach friction factor [78] and it is equal to $4C_f$ where C_f is computed according to the empirical correlation reported in Eq. 4.7. U_{avg} is the average velocity on the cross-sectional area of the pipe which, being the flow area and the density constant along the pipe, is constant as well.

4.6.2 Single sub-channel

The total analytical pressure drop across the sub-channel in the test case described in Subsection 4.2.2 is computed according to the Eq. 4.17 [1].

$$\Delta p = \Delta p_{fric} + \Delta p_{grav} = f \frac{L}{D_h} \rho \frac{U_{avg}^2}{2} + \rho g L \tag{4.17}$$

U_{avg}, as for the previous test case, is the average velocity on the cross-sectional area of the sub-channel which, being the flow area and the density constant along the pipe, is constant as well.

4.6.3 Single sub-channel with solid walls on two edges

The total analytical pressure drop across the sub-channel in the test case described in Subsection 4.2.3 is computed according to the Eq. 4.17 as well. Only the hydraulic diameter D_h and, as a result, the Darcy friction factor f have different values with respect to the test case of Subsection 4.2.2.

4.6.4 2x2 Fuel bundle with three full-length pins and one half-length pin

The total analytical pressure drop across the 2x2 fuel bundle in the test case described in Subsection 4.2.4 is computed according to the Eq. 4.18 [1].

$$\Delta p = \Delta p_{fric} + \Delta p_{grav} + \Delta p_{loc} \tag{4.18}$$

Δp_{fric} is computed as expressed in Eq. 4.19.

$$\Delta p_{fric} = f_1 \frac{L_1 + L_2}{D_{h,1}} \rho \frac{U_{avg,1}^2}{2} + f_2 \frac{L_3 + L_4}{D_{h,2}} \rho \frac{U_{avg,2}^2}{2} \tag{4.19}$$

$D_{h,1}$ and $D_{h,2}$ are the hydraulic diameters in the first and second halves of the fuel bundle respectively and they are computed according to Eq. 4.20 and Eq.4.21.

$$D_{h,1} = \frac{4 A_1}{P_1} = \frac{4 \left((2pit)^2 - 4\pi \frac{d_{rod}^2}{4} \right)}{4\pi d_{rod} + 4pit} \tag{4.20}$$

$$D_{h,2} = \frac{4\,A_2}{P_2} = \frac{4\left((2\,pit)^2 - 3\pi\frac{d_{rod}^2}{4}\right)}{3\pi\,d_{rod} + 4\,pit} \tag{4.21}$$

A_1 and A_2 are the cross-sectional flow area in the first and second halves of the fuel bundle respectively and P_1 and P_2 are their wetted perimeters. The cross-sectional flow area changes between the first half of the channel and the second half of the channel due to the presence of the half-length rod. Due to the constant density of the fluid along the whole channel, the change of the flow area implies different values of the average velocity in the first half of the channel and in the second half of the channel, defined as $U_{avg,1}$ and $U_{avg,2}$ respectively. f_1 and f_2 are the Darcy friction factors computed using $D_{h,1}$, and $U_{avg,1}$ and $D_{h,2}$, and $U_{avg,2}$ respectively. Δp_{grav} is computed as expressed in Eq. 4.22.

$$\Delta p_{grav} = \rho g L \tag{4.22}$$

Δp_{loc} comes from the deceleration of the fluid due to the expansion of the flow area and it is computed as expressed in Eq. 4.23 [79].

$$\Delta p_{loc} = \Delta p_{loc,I} + \Delta p_{loc,R} = k_{enl}\rho\frac{U_{avg,1}^2}{2} - \rho\frac{U_{avg,1}^2}{2}\left[1 - \left(\frac{A_1}{A_2}\right)^2\right] \tag{4.23}$$

$\Delta p_{loc,I}$ and $\Delta p_{loc,R}$ are the irreversible and reversible local pressure drops respectively. k_{enl} is the local loss coefficient for sudden expansion and it is computed according to Eq. 4.24 [79].

$$k_{enl} = \left(1 - \frac{A_1}{A_2}\right)^2 \tag{4.24}$$

Chapter 5

Results and Discussion

The results obtained by the simulations of the test cases presented in Chapter 4 are reported in this chapter. Per each test case three simulations are performed:

- A simulation using a very coarse mesh in which the y^+ falls in the outer region and in which the new wall function approach described in Section 4.1 is implemented.

- A simulation using a very coarse mesh in which the y^+ falls in the outer region and in which the traditional wall function approach described in Section 2.5 is implemented.

- A simulation with a more refined mesh in which the y^+ falls in the log-law region and in which the traditional wall function approach described in Section 2.5 is implemented.

The velocity and temperature profiles on the outlet cross-sectional flow area of the test cases obtained from the three simulations listed above are compared. The axial wall temperature profiles along arbitrary points on the domain of the test cases are reported as well. The wall shear stresses computed in the cells close to the wall obtained with the developed methodology are compared with the ones obtained with more refined mesh simulations with y^+ falling in the log-law region and in which the traditional wall function approach is implemented since they should represent the correct wall shear stresses as explained in Section 2.5. Additionally, the axial pressure profiles obtained with the three different simulations for each test case are compared with the analytical axial pressure profiles described in Section 4.5 which well represent the pressure profiles that would be obtained with a sub-channel code analysis. The

comparison between the axial pressure profiles obtained with the newly developed methodology and the analytical pressure profiles aims to test the capabilities of the new approach. For Test Case 1, Test Case 2, and Test Case 3, if the obtained pressure profiles coincide with the analytical ones, it means that the new methodology is able to give results at least as good as those of the sub-channel codes for problems in which the sub-channel codes are the state-of-the-art methodology since they are single-phase flow problems in which there are no prevailing 3D flow conditions. Test Case 4 is instead a test aimed at verifying the behavior of the new approach in cases where secondary flows are present, given the sudden expansion of the flow area between the two halves of the fuel bundle. If the obtained results are satisfactory, the methodology could be extended to two-phase problems. The possible extension of the developed methodology to multi-phase problems is also the main reason for using OpenFOAM as the CFD software for this project.

5.1 Pipe

The simulations of Test Case 1 which represents a single-phase flow through a heated pipe are carried out by simulating only one slice of the pipe with amplitude $\theta = 1°$ exploiting the advantage of the axisymmetry of the geometry. The very coarse mesh implemented in the simulation is reported in Figure 5.1.1. This very coarse mesh is used for both the simulation with the traditional wall function approach and the new one developed for this project. The mesh in Figure 5.1.1 is obtained by discretizing the

Figure 5.1.1: Slice of the pipe discretized with a very coarse mesh having y^+ falling in the outer region.

domain with 4 cells in the radial direction, 1 cell in the circumferential direction, and 500 cells in the axial direction resulting in $y^+ = 1747.9$ for the simulation with the traditional wall function approach and $y^+ = 1788.4$ for the simulation with the new wall function method. The more refined mesh with y^+ falling in the log-law region that is implemented with the traditional wall function approach is shown in Figure 5.1.2. The relatively refined mesh is obtained by discretizing the domain with 40 cells in the radial direction, 1 cell in the circumferential direction, and 500 cells in the axial direction resulting in $y^+ = 185.3$. The velocity magnitude and the temperature surface

Figure 5.1.2: Slice of the pipe discretized with a relatively refined mesh having y^+ falling in the log-law region.

plots on the outlet cross-sectional flow area of the pipe are reported in Figure 5.1.4 and Figure 5.1.6 respectively. The temperature surface plots on the cross-sectional flow area of the pipe at the end of the heated length are reported in Figure 5.1.8.

Figure 5.1.3: Velocity range in Test Case 1.

Figure 5.1.4: Velocity surface plots on the outlet cross-sectional flow area of Test Case 1 obtained with a) very coarse mesh and traditional wall function approach, b) very coarse mesh and new wall function approach, and c) relatively refined mesh and traditional wall function approach.

As mentioned previously, OpenFOAM computes the value of the flow fields in the centroid of each cell in which the domain is discretized, and then the variation of the field is assumed to be linear across the cell. For a more intuitive understanding of the obtained results, during the post-processing, a constant value is associated with each cell corresponding to the cell centroid value computed directly by OpenFOAM. The surface plots in Figure 5.1.4, Figure 5.1.6, and Figure 5.1.8 are obtained with ParaView that is an open-source, multi-platform data analysis and visualization application [80]. The velocity and the temperature profiles over the line crossing the outlet cross-sectional flow area of the pipe as shown in Figure 5.1.9a, are reported in Figure 5.1.10 and Figure 5.1.11 respectively. The velocity profile obtained with the relatively refined mesh and implementing the traditional wall function approach agrees with the fully-developed turbulent flow velocity profiles in the literature for turbulent flows of incompressible fluids in circular pipes [54]. In fact, the velocity profile shows a nearly

5.8e+02

576.59

576.585

576.58

5.8e+02

(a)

(b)

(c)

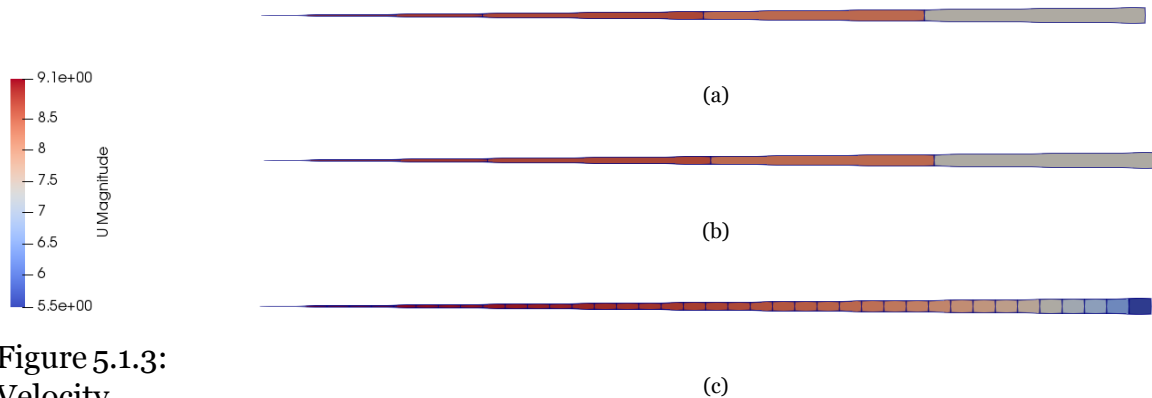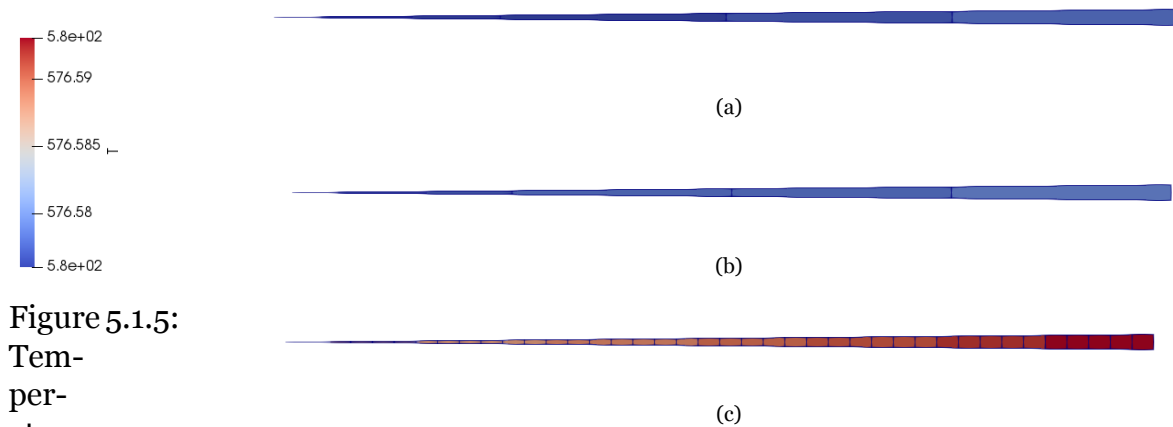Figure 5.1.5: Temperature range in Test Case 1.

Figure 5.1.6: Temperature surface plots on the outlet cross-sectional flow area of Test Case 1 obtained with a) very coarse mesh and traditional wall function approach, b) very coarse mesh and new wall function approach, and c) relatively refined mesh and traditional wall function approach.

linear rapid increase close to the wall and nearly constant velocity in the central part of the flow.

The markers in the plot represent the velocity values calculated by OpenFOAM in the centroids of the cells crossed by the line used for the post-processing depicted in Figure 5.1.9a. In other words, each marker corresponds to the value of a cell and the line joining them is a linear interpolation between two adjacent cell values. The markers are not used for the velocity profile obtained with the relatively refined mesh just for visual purposes. The results obtained with the very coarse mesh implementing the traditional wall function approach and the new wall function approach developed in this project are similar to each other and not really representative of the actual variation of the velocity near the wall unlike the results obtained with the more refined mesh, but however they are able to capture the overall expected behavior.

Having inserted an adiabatic layer at the end of the pipe, the expected temperature profile is a constant line along the radius of the slice and all three simulations agree on this behavior. However, it is interesting to look at the temperature profiles over the pipe cross-section at the axial height of $4m$ to better understand the performance of the implementation of the new methodology and the differences in the results obtained with a very coarse mesh and a more refined one. The temperature profiles over a line crossing the cross-sectional flow area at $4m$ height is reported in Figure 5.1.11a. The
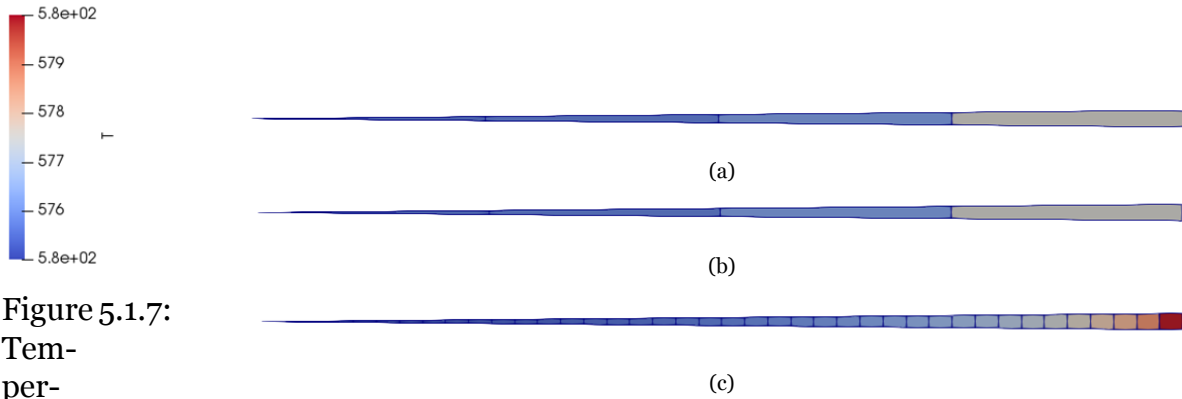
Figure 5.1.7: Temperature range at the end of heated length in Test Case 1.

Figure 5.1.8: Temperature surface plots on the cross-sectional flow area at the end of the heated length of Test Case 1 obtained with a) very coarse mesh and traditional wall function approach, b) very coarse mesh and new wall function approach, and c) relatively refined mesh and traditional wall function approach.
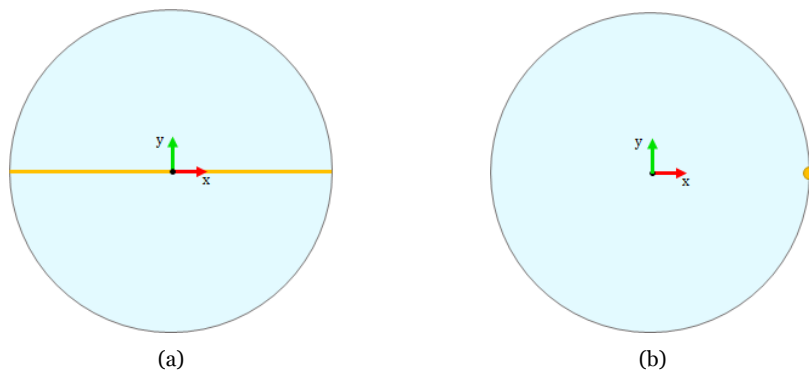
Figure 5.1.9: a) Post-processing line over which the velocity and temperature profile at the outlet of the pipe are plotted. b) Arbitrary point chosen to evaluate the axial wall temperature profile.

temperature profile obtained with the more refined mesh implementing the traditional wall function approach agrees with the fully-developed turbulent flow temperature profiles in the literature for turbulent flows in a heated circular pipe [81]. As for the outlet velocity profile, the results obtained with the very coarse mesh implementing the traditional wall function approach and the new wall function approach developed in this project are similar to each other and not really representative of the actual variation of the temperature near the wall unlike the results obtained with the more refined mesh, but however, they are able to capture the overall expected behavior.

The axial wall temperature profile over a line perpendicular to the cross-sectional area and passing through the point shown in Figure 5.1.9b is shown in Figure 5.1.12. The
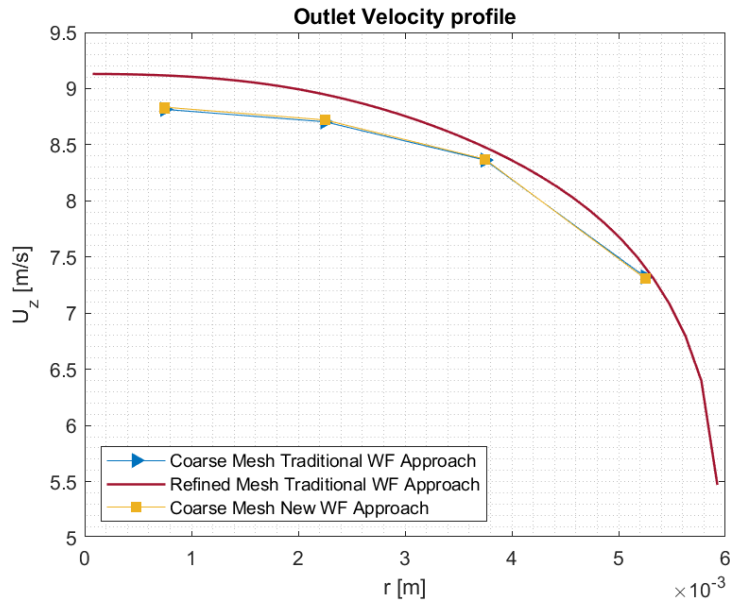
Figure 5.1.10: Outlet velocity profile over a line crossing the pipe.
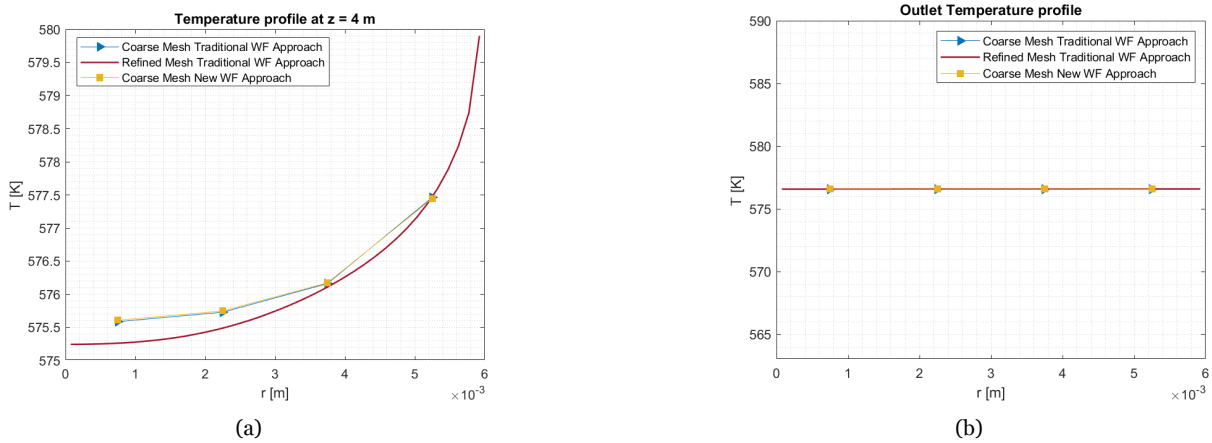
Figure 5.1.11: a) Temperature profile over a line crossing perpendicularly the pipe at 4 m height. b) Temperature profile over a line crossing perpendicularly the pipe at the outlet.

obtained results with all three simulations properly capture the physics of the problem having constant values along the first and last adiabatic layers and having a linear increase in the layer with constant heat flux boundary condition as expected from the literature [81]. The difference between the results obtained with the very coarse mesh and the more refined one can be seen mostly in the transition of the temperature profile between the two adiabatic layers and the heated layer. One of the most important reasons why the wall temperature profiles of the coarse mesh simulation with the new wall function approach and the coarse mesh simulation with the traditional wall function approach are so close is that in the first simulation the wall temperature is calculated based on the same traditional wall function of the second one.
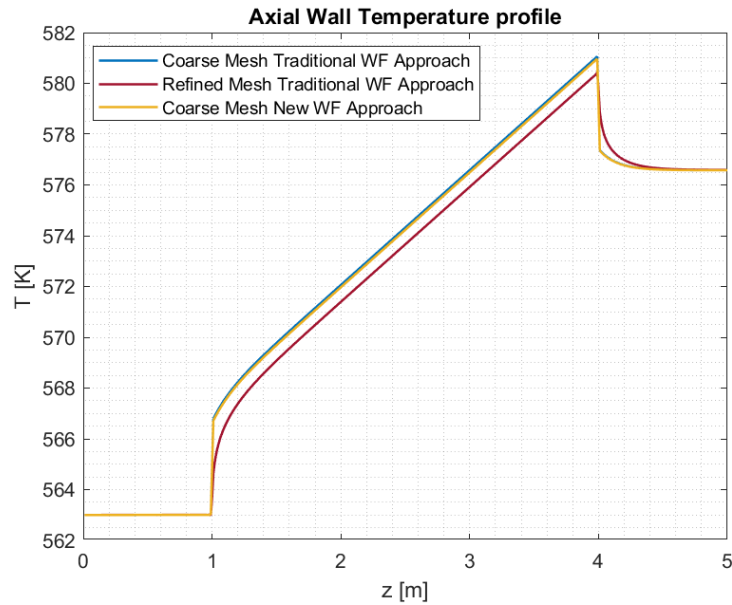
Figure 5.1.12: Axial wall temperature profile in Test Case 1.

Finally, the axial pressure profile along the central axis of the pipe is reported in Figure 5.1.13. As can be seen, the pressure profile obtained with the very coarse
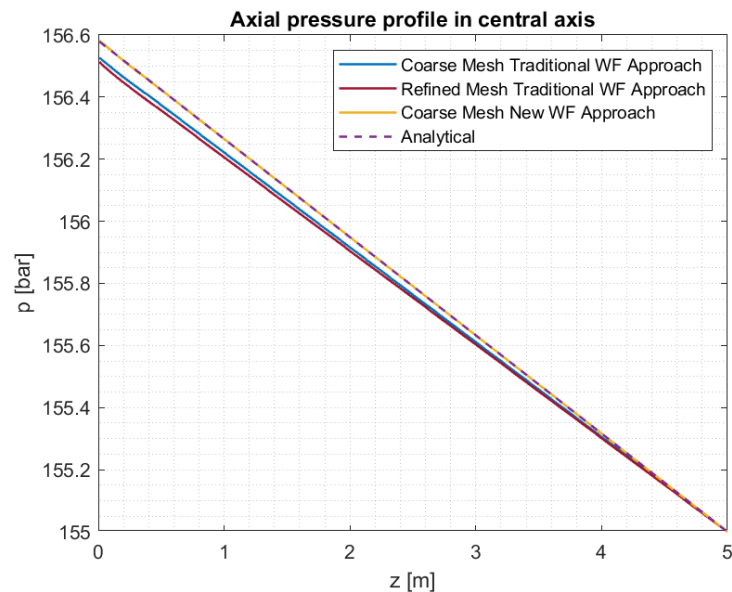
Figure 5.1.13: Axial pressure profile along the central axis of the pipe.

mesh simulation implementing the new wall function approach perfectly matches the analytical pressure profile, described by Eq. 4.16 in Chapter 4, suggesting that the implementation of the friction correlation in the new wall function approach is correct. The wall shear stresses computed by OpenFOAM in the simulation with the very coarse mesh and the new wall function approach and the simulation with the more refined mesh and the traditional wall function approach based on the log-law region are listed

in Table 5.1.1. Only one value of wall shear stress computed in the refined mesh

Simulation	Wall Shear Stress Values
Coarse mesh and new wall function approach	72.9 Pa
Refined mesh and traditional wall function approach	68.6 Pa

Table 5.1.1: Wall shear stresses obtained for Test Case 1 in the simulation with the very coarse mesh and the new wall function approach and the simulation with the more refined mesh and the traditional wall function method.

simulation is listed because being the pipe an axisymmetric geometry the wall shear stress is the same for all the cells at the wall. On the other hand, the wall shear stress computed in the simulation with the new wall function approach should always be constant in all the wall cells for all the test cases since the methodology is based on the 1D wall shear stress calculation as explained in Chapter 4. From the results presented in Figure 5.1.13 and in Table 5.1.1, the new methodology developed in this project seems to work correctly for the simple test case of a flow in a heated pipe since the results obtained for the axial pressure profile are matching the analytical profile that should well represent the pressure results of a generic sub-channel code implementing the same empirical correlation for the Fanning friction factor used in the new wall function approach. Furthermore, the wall shear stress obtained with the new wall function approach is very close to the value obtained from the simulation with a more refined mesh using the traditional wall function methodology which should well capture the true wall shear stress values of the cells at the wall for the reasons explained in Section 2.5.

5.2   Single sub-channel

Test Case 2 consists of a single-phase flow through the sub-channel of a PWR. The very coarse mesh used to discretize the domain is reported in Figure 5.2.1. The mesh is used for both the simulation with the traditional wall function approach and the new one developed for this project. The mesh in Figure 5.2.1 is obtained by discretizing the domain with 8 blocks and each block is discretized with 2 cells in the radial direction, 2 cells in the circumferential direction, and 300 cells in the axial direction resulting in an average $y^+ = 802.3$ in the first adiabatic layer and an average $y^+ = 805.5$ in the heated layer and in the last adiabatic layer at the end of the last time step for the simulation with the traditional wall function approach and an average $y^+ = 833.4$ in
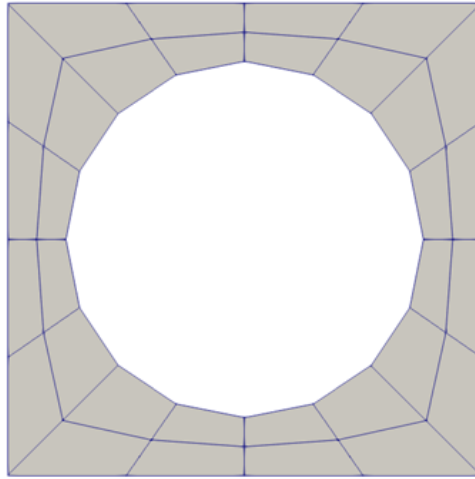
Figure 5.2.1: Sub-channel of Test Case 2 discretized with a very coarse mesh having y^+ falling in the outer region.

the first adiabatic layer and an average $y^+ = 838$ in the heated layer and in the last adiabatic layer at the end of the last time step for the simulation with the new wall function method. The more refined mesh with y^+ falling in the log-law region that is implemented with the traditional wall function approach is shown in Figure 5.3.4. The
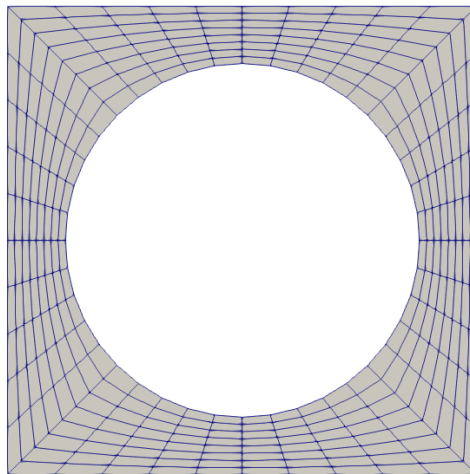
Figure 5.2.2: Sub-channel of Test Case 2 discretized with a relatively refined mesh having y^+ falling in the log-law region.

relatively refined mesh is obtained by discretizing the domain in 8 blocks and each block is discretized with 8 cells in the radial direction, 5 cells in the circumferential direction, and 300 cells in the axial direction resulting in an average $y^+ = 201.4$ in the first adiabatic layer and an average $y^+ = 201.6$ in the heated layer and in the last adiabatic layer at the end of the last time step.

The velocity and the temperature surface plots on the outlet cross-sectional flow area of the sub-channel are reported in Figure 5.2.4 and Figure 5.2.6 respectively. The

temperature surface plots on the cross-sectional flow area of the pipe at the end of the heated length are reported in Figure 5.2.8.

(a)

(b)

(c)
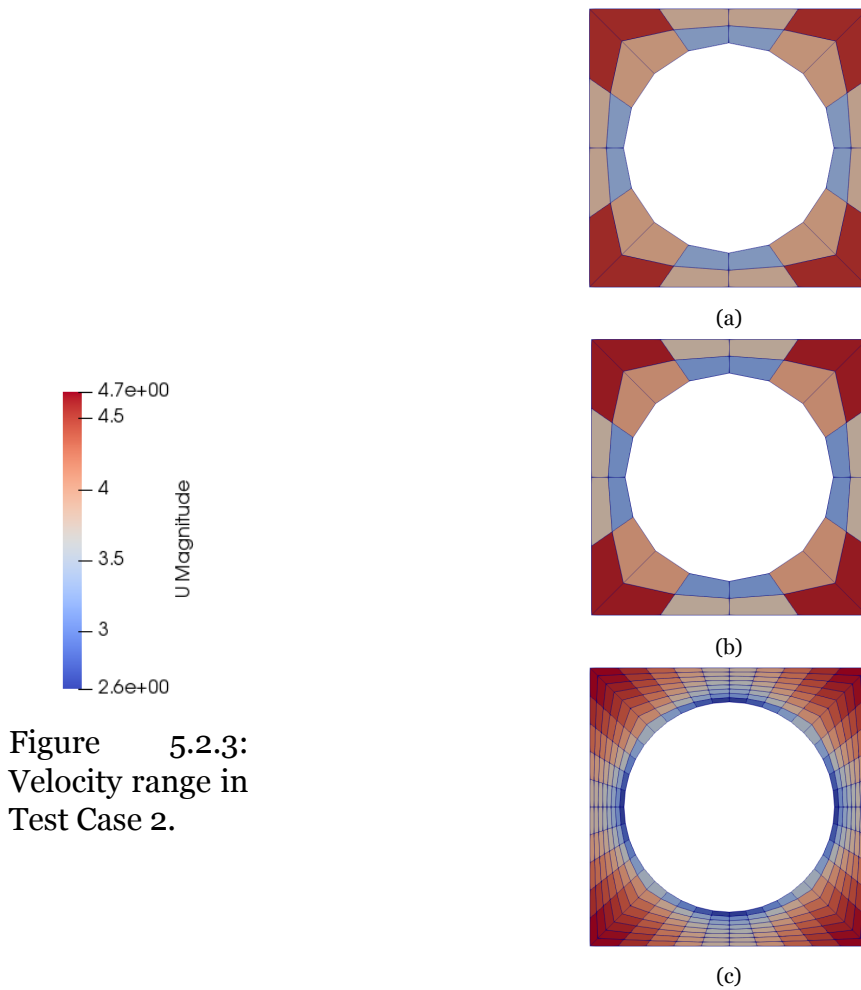
Figure 5.2.3: Velocity range in Test Case 2.

Figure 5.2.4: Velocity surface plots on the outlet cross-sectional flow area of Test Case 2 obtained with a) very coarse mesh and traditional wall function approach, b) very coarse mesh and new wall function approach, and c) relatively refined mesh and traditional wall function approach.

As for Test Case 1, for a more intuitive understanding of the obtained results, during the post-processing, a constant value is associated with each cell corresponding to the cell centroid value computed directly by OpenFOAM. The surface plots in Figure 5.2.4, Figure 5.2.6 and Figure 5.2.8 are obtained with ParaView. The velocity and the temperature profiles over the lines crossing the outlet cross-sectional flow area of the sub-channel as shown in Figure 5.2.9, are reported in Figure 5.2.10 and Figure 5.2.11 respectively. The velocity profiles obtained look reasonable since they capture the expected profile of velocity tending to zero at the rod wall, due to the no-slip boundary condition imposed, and having the highest values at sub-channel edges, due to the

(a)

(b)

(c)

Figure 5.2.5: Temperature range in Test Case 2.
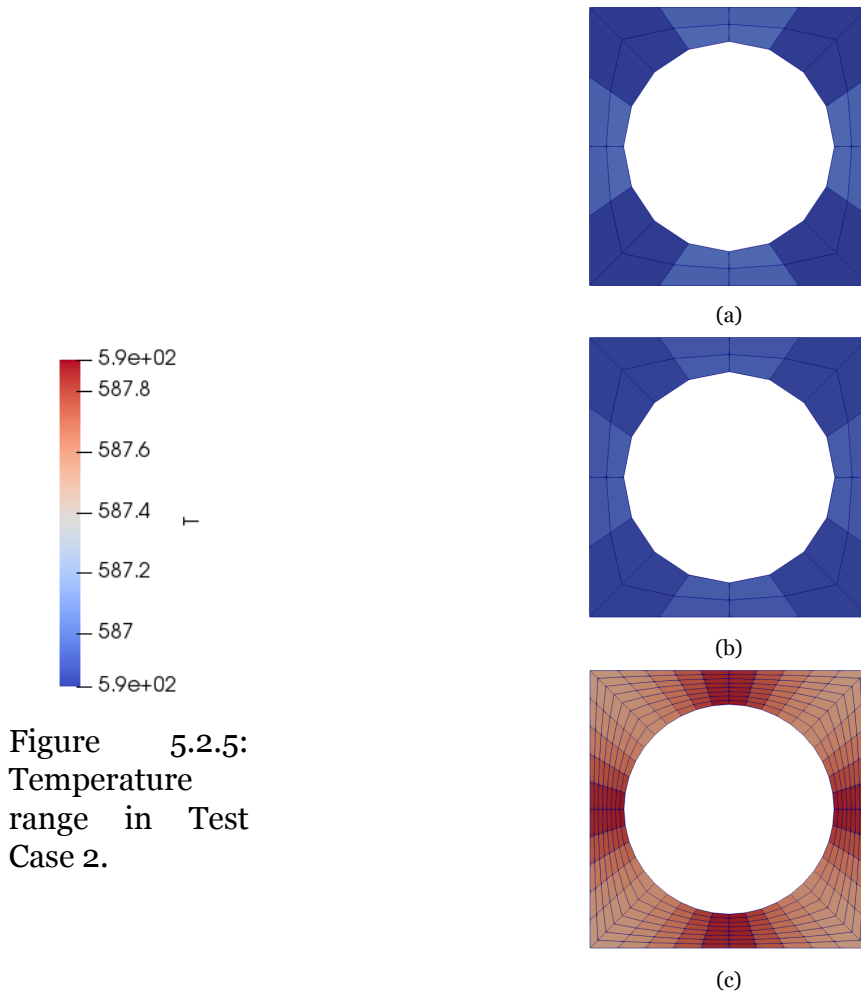
Figure 5.2.6: Temperature surface plots on the outlet cross-sectional flow area of Test Case 2 obtained with a) very coarse mesh and traditional wall function approach, b) very coarse mesh and new wall function approach, and c) relatively refined mesh and traditional wall function approach.

symmetric boundary condition imposed. Additionally, the two post-processing lines diagonal 1 and diagonal 2 are chosen symmetric about the 45° line to check if the respective captured profiles are identical. The outlet velocity profiles obtained for Test Case 2 are the same as expected. The velocity results obtained with the very coarse mesh implementing the traditional wall function approach and the new wall function approach developed in this project are similar to each other and close to the refined mesh simulation with the traditional wall function method. As already mentioned for Test Case 1, the markers in the plot represent the velocity values calculated by OpenFOAM in the centroids of the cells crossed by the lines used for the post-processing depicted in Figure 5.2.9 and they are not used for the velocity profile obtained with the relatively refined mesh just for visual purposes. As for the

(a)

(b)

(c)

6.0e+02

595

590

585

5.8e+02
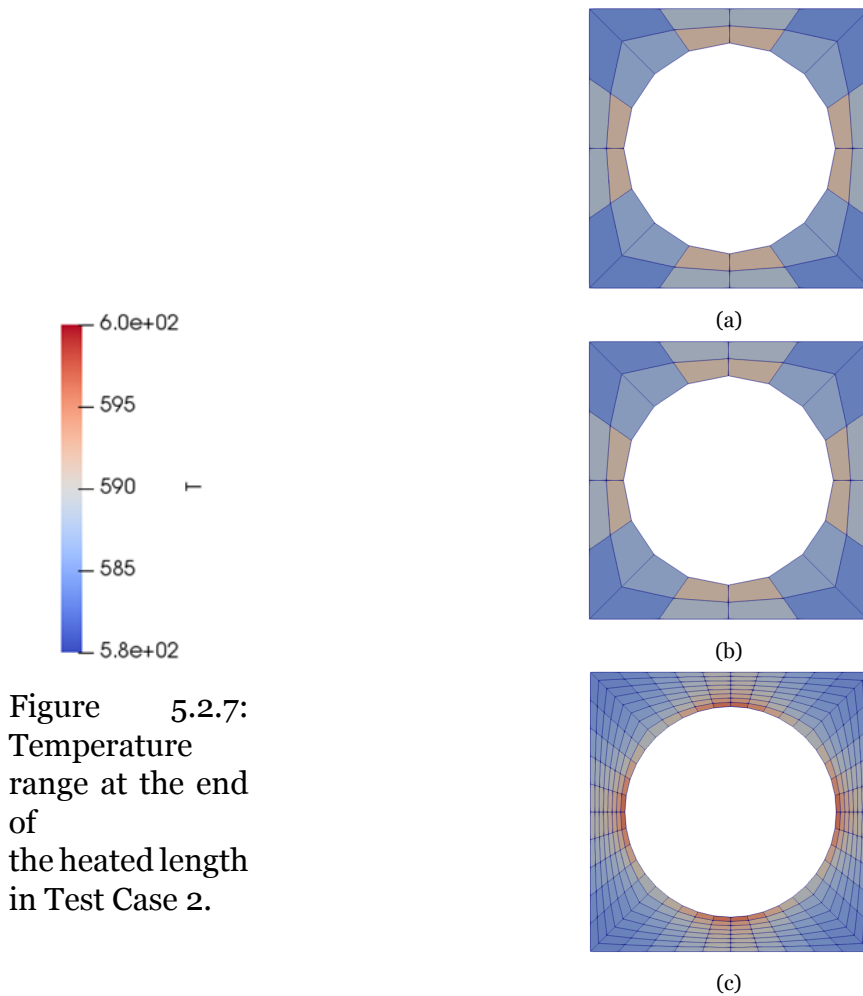
Figure 5.2.7: Temperature range at the end of the heated length in Test Case 2.

Figure 5.2.8: Temperature surface plots on the cross-sectional flow area at the end of the heated length of Test Case 2 obtained with a) very coarse mesh and traditional wall function approach, b) very coarse mesh and new wall function approach, and c) relatively refined mesh and traditional wall function approach.

pipe test case, having an adiabatic layer at the end of the sub-channel, the expected temperature profile is a constant over the outlet cross-sectional flow area and all three simulations agree on this behavior. The axial pressure profile along the bottom left corner of the sub-channel is reported in Figure 5.2.12. As can be seen in Figure 5.1.13, the pressure profile obtained with the very coarse mesh simulation implementing the new wall function approach is closer to the analytical pressure profile described by Eq. 4.17 in Chapter 4 with respect to the simulations in which the traditional wall function approach is implemented, but it is not matching exactly the analytical profile. A possible explanation for this behavior will be provided in Section 5.5.

The wall shear stresses of the cells facing the wall patches at the outlet cross-sectional flow area of the sub-channel are listed in Table 5.2.1. The range of values of the
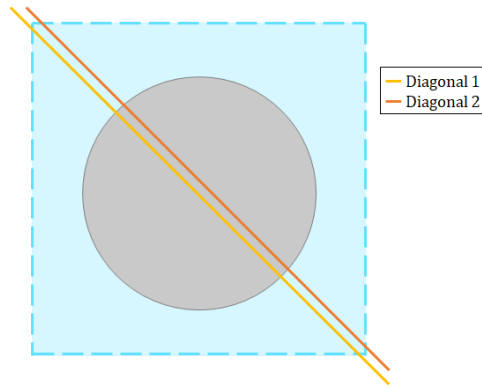
Figure 5.2.9: Post-processing lines over which the velocity and temperature profile at the outlet of the sub-channel of Test Case 2 are plotted.

(a) Outlet velocity profile over diagonal 1.

(b) Outlet velocity profile over diagonal 2.
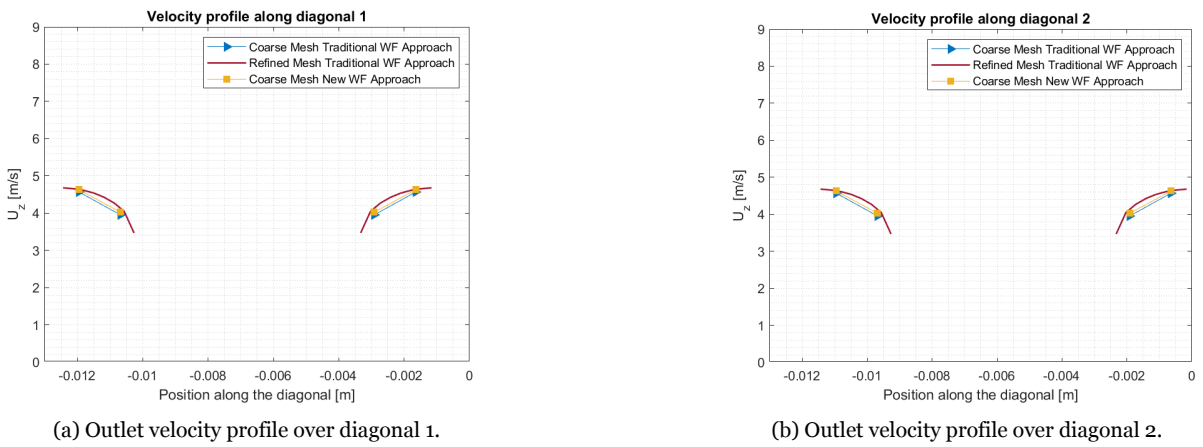
Figure 5.2.10: Outlet velocity profile over a) diagonal 1 and b) diagonal 2 of Test Case 2.

actual wall shear stresses in the cells close to the rod wall is relatively small and the constant wall shear stress imposed with the new wall function approach is within this range. The variations of the wall shear stresses obtained in the simulation with the very coarse mesh and the new wall function approach and the simulation with the more refined mesh and the traditional wall function approach based on the log-law region are reported in Figure 5.2.13. The cell ID on the x-axis of the plot in Figure 5.2.13 is simply the identification index of the cells facing the wall patches in the domain. It can be noticed that the wall shear stresses computed in the refined mesh simulation are not constant as in Test Case 1 since the geometry of the problem is no longer axisymmetric. From the results presented in Figure 5.2.12 and in Figure 5.2.13, the new methodology developed in this project seems to work quite well for the test case of the flow in the sub-channel of a PWR since the results obtained for the axial pressure profile are close enough to the analytical profile that should well represent the pressure results of a generic sub-channel code implementing the same empirical correlation for the Fanning

(a) Outlet temperature profile over diagonal 1.

(b) Outlet temperature profile over diagonal 2.
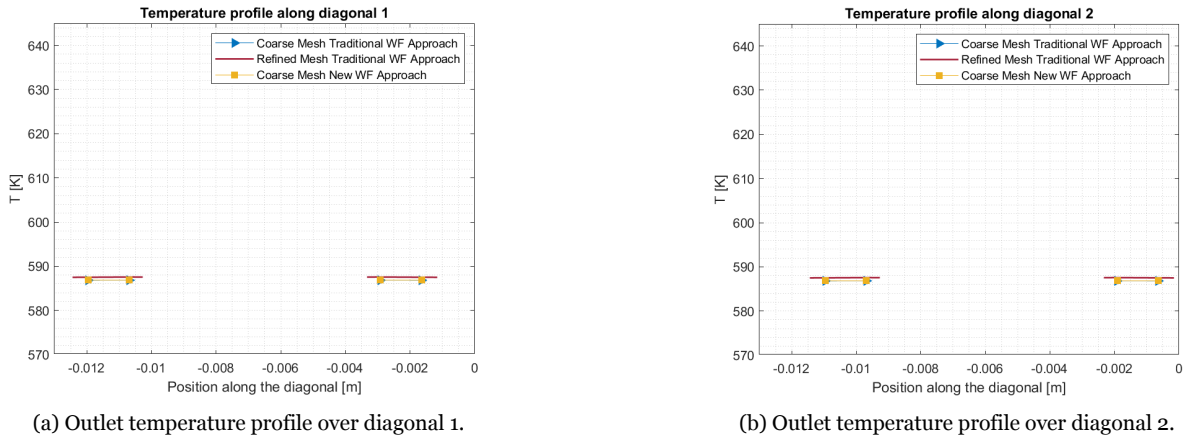
Figure 5.2.11: Outlet temperature profile over a) diagonal 1 and b) diagonal 2 of Test Case 2.
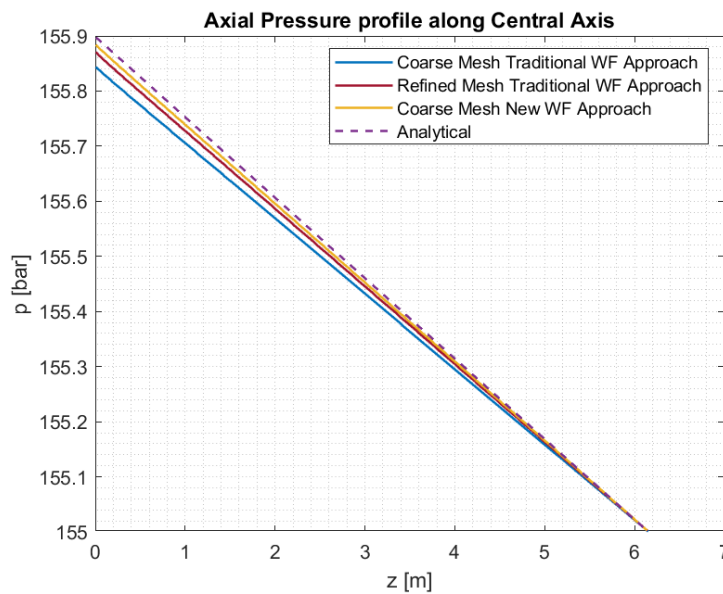
Figure 5.2.12: Axial pressure profile along the bottom left corner of the sub-channel of Test Case 2.

friction factor used in the new wall function approach and the wall shear stress imposed with the new wall function approach is within the range of variation of the wall shear stresses obtained from the simulation with a more refined mesh using the traditional wall function methodology which should well capture the actual wall shear stress values of the cells at the wall for the reasons explained in Section 2.5.

69

Simulation	Wall Shear Stress Values
Coarse mesh and new wall function approach	$21.2\ Pa$
Refined mesh and traditional wall function approach	between $[17, 23]\ Pa$

Table 5.2.1: Wall shear stresses obtained for Test Case 2 in the simulation with the very coarse mesh and the new wall function approach and the simulation with the more refined mesh and the traditional wall function method.
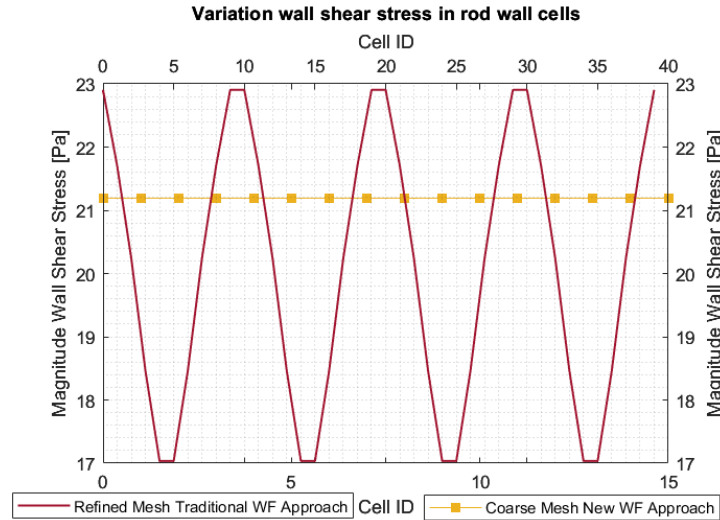
Figure 5.2.13: Comparison of wall shear stresses obtained in the coarse mesh simulation with new wall function approach and the refined mesh one with traditional wall function approach in Test Case 2.

5.3 Single sub-channel with solid walls on two edges

Test Case 3 consists of a single-phase flow through the sub-channel located in the corner of a fuel assembly in a PWR. The wall boundaries in Test Case 3 are mostly irrelevant in a PWR core, but they are included because relevant for experimental test sections. Two different coarse meshes are tested to discretize the domain. The first mesh is the one used for the previous test case and it is reported in Figure 5.3.1a and the second one is reported in Figure 5.3.1b. The two meshes are tested for both the simulation with the traditional wall function approach and the new one developed for this project.

5.3.1 Mesh with 2 cells in the radial direction

The mesh in Figure 5.3.1a is obtained by discretizing the domain with 8 blocks and each block is discretized with 2 cells in the radial direction, 2 cells in the circumferential

Figure 5.3.1: Sub-channel of Test Case 2 discretized with two coarse meshes having y^+ falling in the outer region. a) Coarse mesh having 2 cells in the radial direction. b) Coarse mesh having 4 cells in the radial direction.

direction, and 300 cells in the axial direction resulting in average $y^+ = 619.7$, $y^+ = 584.3$, and $y^+ = 582.8$ of the cells at the sub-channel solid walls in the first adiabatic layer, in the heated layer and in the last adiabatic layer respectively at the end of the last time step for the simulation with the traditional wall function approach and average $y^+ = 711.6$, $y^+ = 722.4$, and $y^+ = 726.7$ of the same cells at the end of the last time step for the simulation with the new wall function method. The average y^+ of the cells at the rod wall are equal to $y^+ = 855.7$, $y^+ = 858.7$, and $y^+ = 858.9$ in the first adiabatic layer, in the heated layer and in the last adiabatic layer respectively at the end of the last time step for the simulation with the traditional wall function approach and $y^+ = 910.4$, $y^+ = 956.8$, and $y^+ = 970$ of the same cells at the end of the last time step for the simulation with the new wall function method. The velocity profiles over
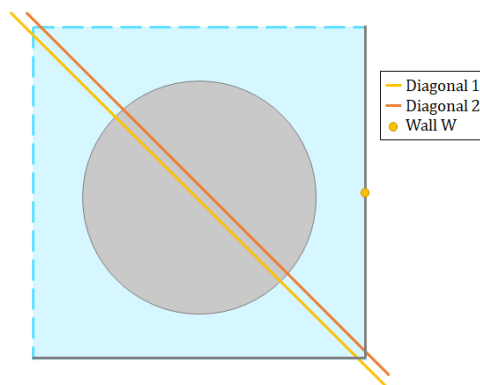
Figure 5.3.2: Post-processing lines over which the velocity and temperature profile at the outlet of the sub-channel of Test Case 3 are plotted.

the lines crossing the outlet cross-sectional flow area of the sub-channel as shown in Figure 5.3.2, are reported in Figure 5.3.3. The coarse mesh simulation implementing

(a) Outlet velocity profile over diagonal 1.

(b) Outlet velocity profile over diagonal 2.
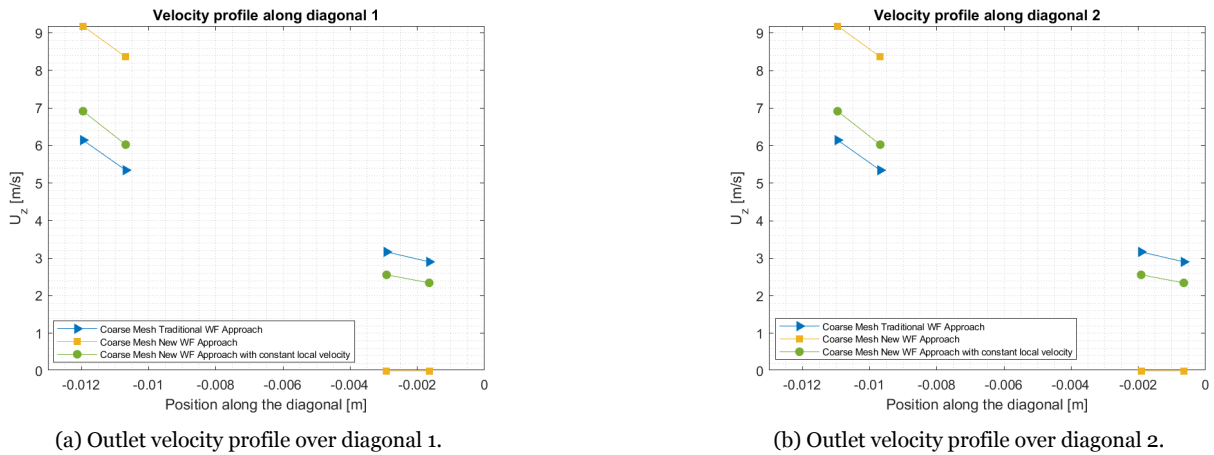
Figure 5.3.3: Outlet velocity profile over a) diagonal 1 and b) diagonal 2 for Test Case 3 obtained with a coarse mesh having two cells between the rod wall and the sub-channel solid wall.

the new wall function approach seems to not work properly since the velocity between the rod wall and the solid wall of the sub-channel is captured as equal to zero while in the coarse mesh simulation with the traditional wall function method implemented the velocity profile between these walls is different from zero as it is expected to be. To understand the reasons why the new methodology is unable to give reasonable velocity values between the rod wall and the sub-channel solid wall, a further simulation was carried out by modifying the conditional statement reported in Eq. 4.5 by replacing the velocity u_P, corresponding to the local velocity in the centroid of the cell at the wall and calculated by OpenFOAM during the simulation, with an arbitrary constant speed equal to $3m/s$. The velocity profiles plotted along diagonals 1 and 2 are shown in Figure 5.3.3. As it is possible to see from the plot, the coarse mesh simulation using the new wall function method with the constant local velocity gives more reasonable results since the velocity between the rod wall and the sub-channel wall has values different from zero. Taking into account the results obtained from the simulation where the new wall function approach with the constant local velocity is implemented, a possible explanation for the performance of the simulation with the new wall function approach but with the local velocity calculated by OpenFOAM could be the combination of the mathematical form foreseen by the new methodology developed in this thesis which requires the presence of the local velocity at the denominator and the discretization used between the two solid walls with no-slip boundary condition applied. To verify

this possible explanation, a simulation with a more refined mesh in the radial direction has been tested and the obtained results are reported in the following subsection.

5.3.2 Mesh with 4 cells in the radial direction

The mesh in Figure 5.3.1b is obtained by discretizing the domain with 8 blocks and each block is discretized with 4 cells in the radial d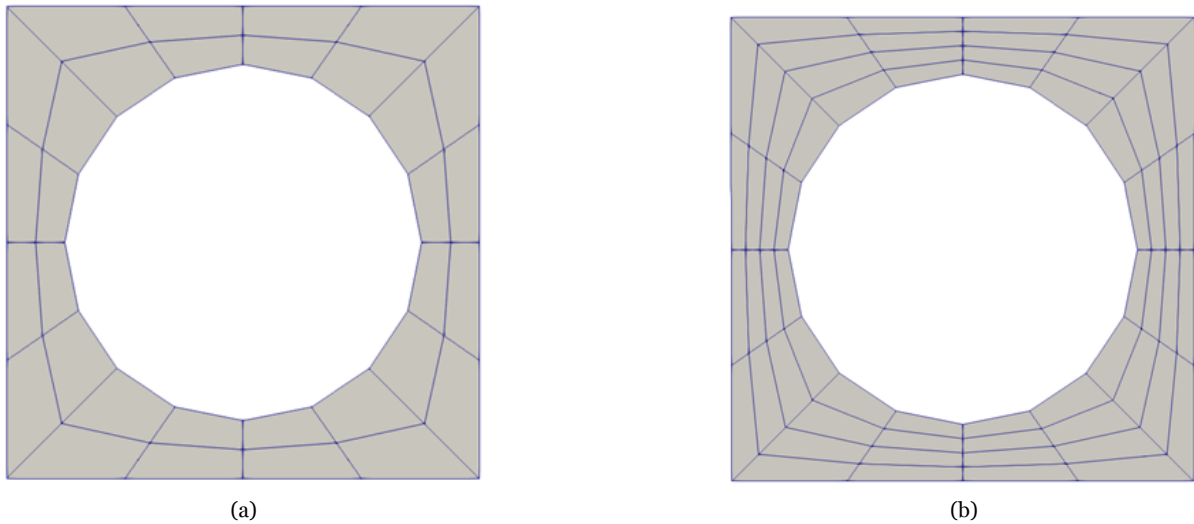irection, 2 cells in the circumferential direction, and 300 cells in the axial direction resulting in average $y^+ = 305.8$, $y^+ = 288.1$, and $y^+ = 287.4$ of the cells at the sub-channel solid walls in the first adiabatic layer, in the heated layer and in the last adiabatic layer respectively at the end of the last time step for the simulation with the traditional wall function approach and average $y^+ = 355.4$, $y^+ = 353, 8$, and $y^+ = 352.6$ of the same cells at the end of the last time step for the simulation with the new wall function method. The average y^+ of the cells at the rod wall are equal to $y^+ = 421.2$, $y^+ = 422.2$, and $y^+ = 422.2$ in the first adiabatic layer, in the heated layer and in the last adiabatic layer respectively at the end of the last time step for the simulation with the traditional wall function approach and $y^+ = 444.4$, $y^+ = 444.4$, and $y^+ = 442.2$ of the same cells at the end of the last time step for the simulation with the new wall function method. The results obtained in the coarse mesh simulation with the traditional wall function approach and the coarse mesh simulation with the new wall function method developed for this project are compared with the results obtained with a more refined mesh simulation with y^+ falling in the log-law region that is implemented with the traditional wall function approach. The more refined mesh is shown in Figure 5.3.4. The relatively
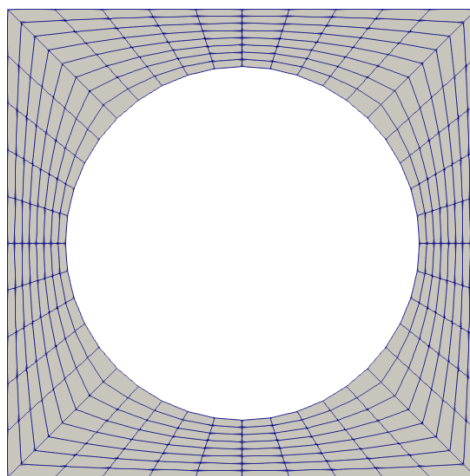

Figure 5.3.4: Sub-channel of Test Case 3 discretized with a relatively refined mesh having y^+ falling in the log-law region.

refined mesh is obtained by discretizing the domain in 8 blocks and each block is discretized with 8 cells in the radial direction, 5 cells in the circumferential direction, and 300 cells in the axial direction resulting in average $y^+ = 152, 2$, $y^+ = 143.1$, and $y^+ = 142.7$ of the cells at the sub-channel solid walls in the first adiabatic layer, in the heated layer and in the last adiabatic layer respectively at the end of the last time step and an average $y^+ = 208.6$ of the cells at the rod wall in the first adiabatic layer, in the heated layer and in the last adiabatic layer at the end of the last time step. The velocity profiles over the lines crossing the outlet cross-sectional flow area of the sub-channel as shown in Figure 5.3.2, are reported in Figure 5.3.5. The new

(a) Outlet velocity profile over diagonal 1.

(b) Outlet velocity profile over diagonal 2.
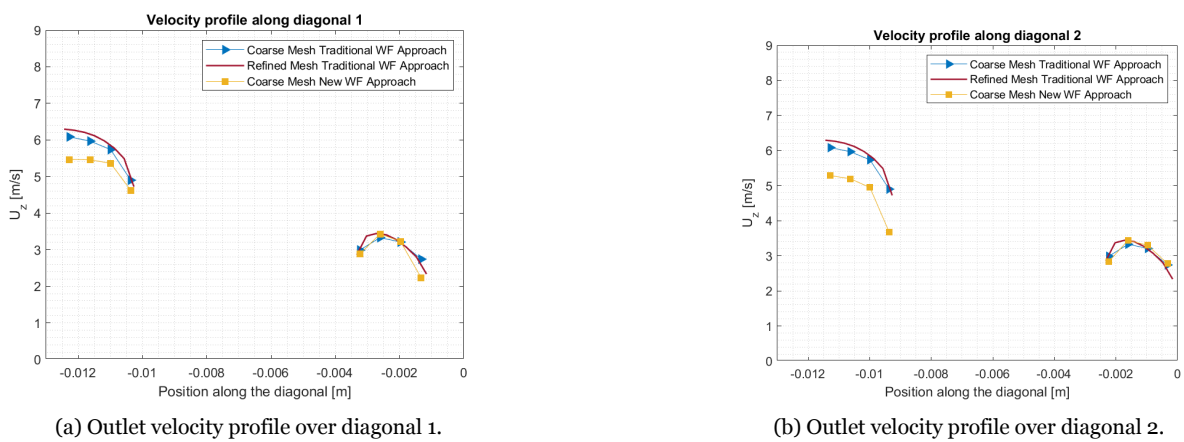
Figure 5.3.5: Outlet velocity profile over a) diagonal 1 and b) diagonal 2 obtained for Test Case 3 with a coarse mesh having four cells between the rod wall and the sub-channel solid wall.

coarse mesh simulation implementing the new wall function approach with the local velocity computed by OpenFOAM during the simulation seems to properly capture the velocity between the rod wall and the solid wall of the sub-channel now since it is different from zero as it is expected to be. Comparing the velocity profiles over diagonal 1 and diagonal 2 which are obtained with the new wall function approach, it can be noticed that they are not symmetric as instead they are expected to be and as they are for the simulations with the traditional wall function approach implemented. The reason for this is that the new methodology implemented causes convergence issues that lead the simulation to not reach convergence within a reasonable number of time iterations. From a computational point of view, therefore, the results presented in this subsection are not valid since the simulation does not reach convergence, but they are equally presented because they are useful to draw conclusions on the applicability of the new methodology developed for this project. The temperature profiles over the lines crossing the outlet cross-sectional flow area of the sub-channel

as shown in Figure 5.3.2, are reported in Figure 5.3.6. It can be noticed that the outlet

(a) Outlet temperature profile over diagonal 1.

(b) Outlet temperature profile over diagonal 2.
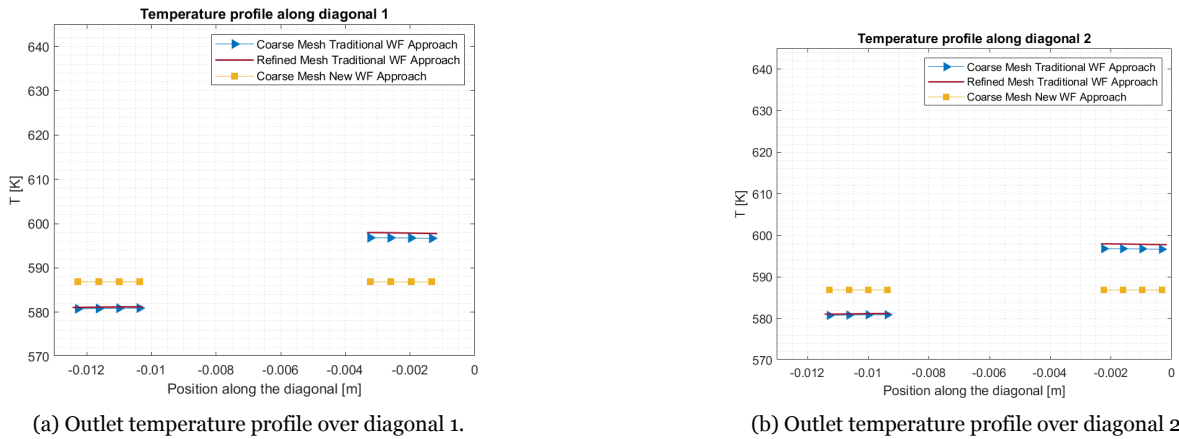
Figure 5.3.6: Outlet temperature profile over a) diagonal 1 and b) diagonal 2 obtained for Test Case 3 with a coarse mesh having four cells between the rod wall and the sub-channel solid wall.

temperature profiles obtained with coarse mesh and refined mesh with the traditional wall function approach applied are not constant over the cross-sectional flow area of the sub-channel, as they were in Test Case 2, since the velocity in the bottom right corner between the rod wall and the sub-channel solid wall is smaller than the velocity in the top left corner of the sub-channel where the symmetry boundary conditions are applied. This behavior is not captured by the simulation with the new wall function approach probably due to the convergence issues. The velocity and the temperature surface plots on the outlet cross-sectional flow area of the sub-channel are reported in Figure 5.3.8 and Figure 5.3.10 respectively.

As for the previous test cases, for a more intuitive understanding of the obtained results, during the post-processing, a constant value is associated with each cell corresponding to the cell centroid value computed directly by OpenFOAM. The axial wall temperature profile over a line perpendicular to the cross-sectional area and passing through the point shown in Figure 5.3.2 is shown in Figure 5.3.11. The obtained results with the two simulations with the traditional wall function approach properly capture the physics of the problem having constant temperature values along the first and last adiabatic layers and having a linear increase in the layer with constant heat flux boundary condition as expected. The simulation with the new wall function approach captures the overall expected behavior but the convergence issues led to a temperature profile that fluctuates in the heated layer. The axial pressure profile along the bottom left corner of the sub-channel is reported in Figure 5.3.12. As can

(a)

(b)

(c)

Figure 5.3.7: Velocity range in Test Case 3.

Figure 5.3.8: Velocity surface plots on the outlet cross-sectional flow area of Test Case 3 obtained with a) very coarse mesh and traditional wall function approach, b) very coarse mesh and new wall function approach, and c) relatively refined mesh and traditional wall function approach.

be seen in Figure 5.3.12, the pressure profile obtained with the very coarse mesh simulation implementing the new wall function approach is closer to the analytical pressure profile described by Eq. 4.17 in Chapter 4 with respect to the simulations in which the traditional wall function approach is implemented. In particular, it quite matches the analytical profile in the heated layer and the last adiabatic layer, but it shows an unexpected behavior at the inlet of the heated layer where also convergence issues-related fluctuations can be seen.

The wall shear stresses of the cells facing the sub-channel wall patches and the rod wall patches at the outlet cross-sectional flow area of the sub-channel are listed in Table 5.3.1. The range of values of the actual wall shear stresses in the cells close to the sub-channel wall is relatively small and the constant wall shear stress imposed with the new

(a)

(b)

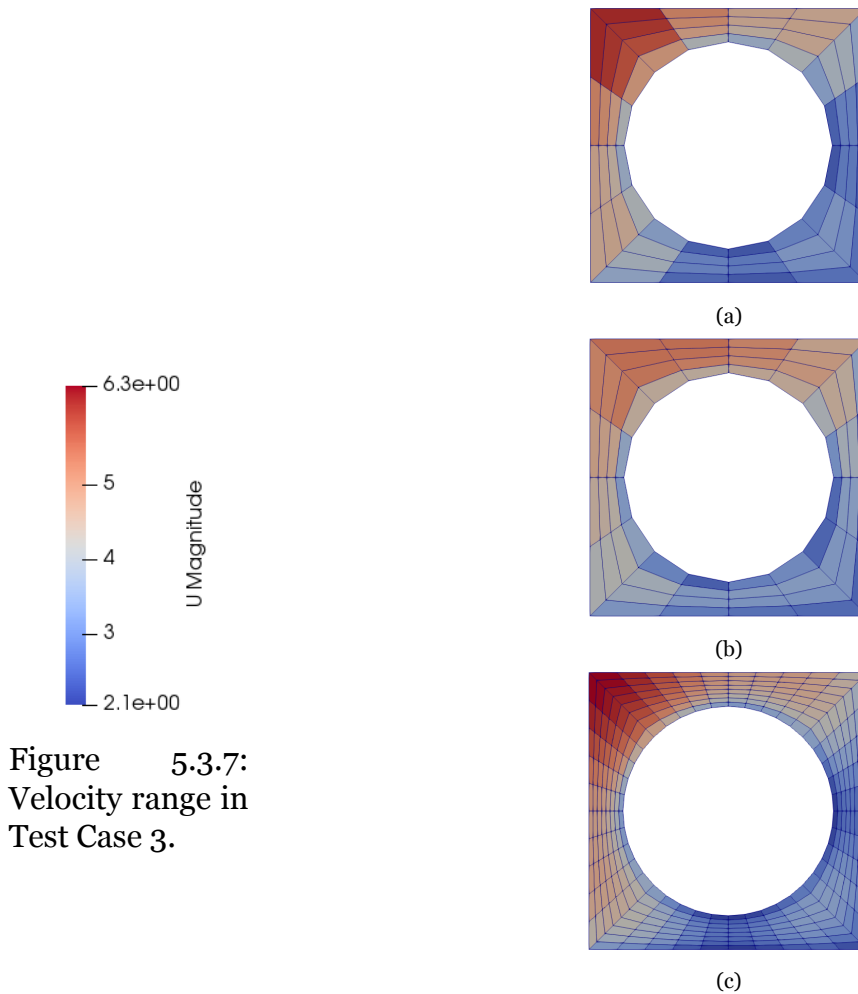(c)

Figure 5.3.9: Temperature range in Test Case 3..
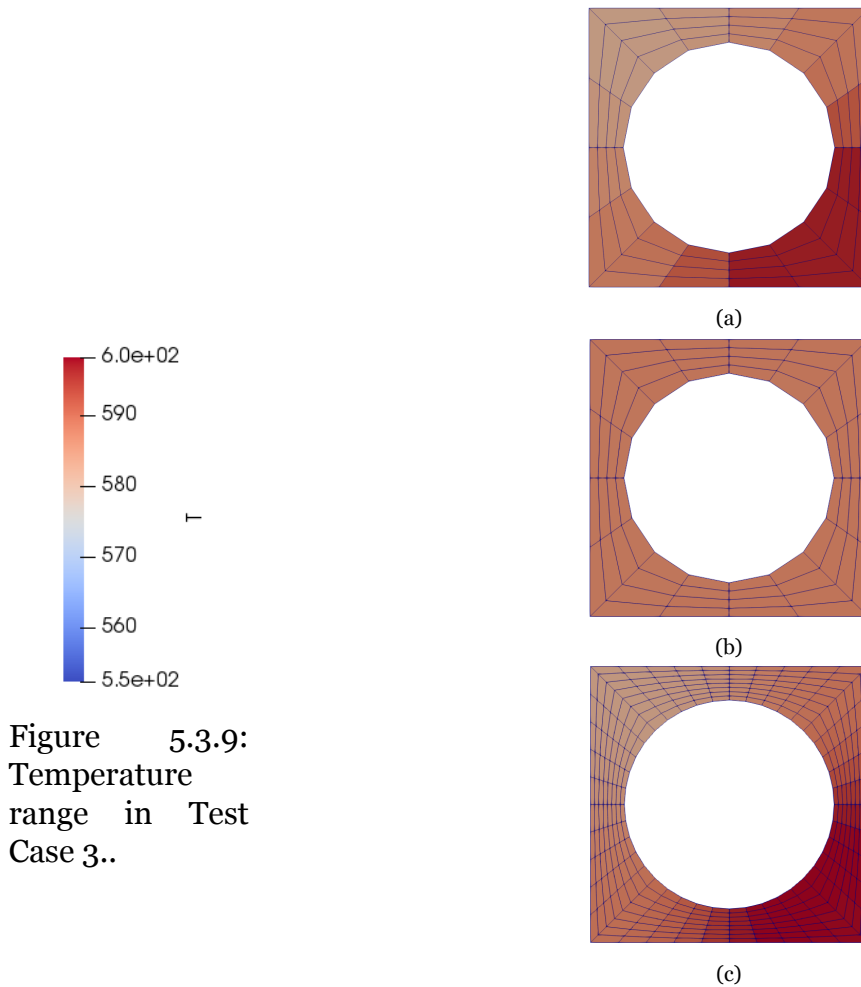
Figure 5.3.10: Temperature surface plots on the outlet cross-sectional flow area of Test Case 3 obtained with a) very coarse mesh and traditional wall function approach, b) very coarse mesh and new wall function approach, and c) relatively refined mesh and traditional wall function approach.

wall function approach is close to this range. Instead, the range of values of the actual wall shear stresses in the cells close to the rod wall is quite large and the constant wall shear stress imposed with the new wall function approach is within the range, but it is not representative at all of the actual variation of the wall shear stresses. The variations of the wall shear stresses obtained in the simulation with the very coarse mesh and the new wall function approach, and the simulation with the more refined mesh and the traditional wall function approach based on the log-law region are reported in Figure 5.3.13. The cell ID on the x-axis of the plot in Figure 5.3.13 is simply the identification index of the cells facing the wall patches in the domain. As for Test Case 2, the wall shear stresses computed in the refined mesh simulation are not constant since the geometry of the problem is not axisymmetric.
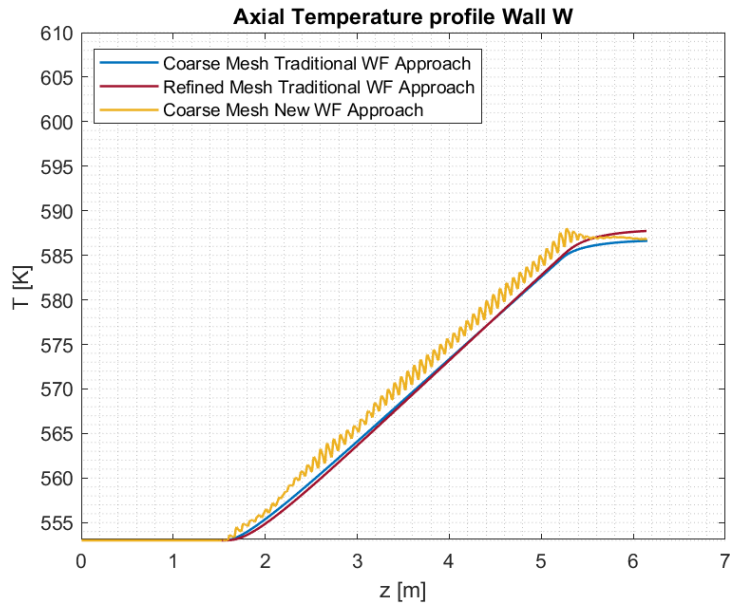
Figure 5.3.11: Axial wall temperature profile in Test Case 3.

Patches	Simulation	Wall Shear Stress Values
Rod Wall	Coarse mesh and new wall function approach	$23.7\ Pa$
	Refined mesh and traditional wall function approach	between $[11, 40]\ Pa$
Sub-channel Wall	Coarse mesh and new wall function approach	$23.7\ Pa$
	Refined mesh and traditional wall function approach	between $[11, 23.5]\ Pa$

Table 5.3.1: Wall shear stresses obtained for Test Case 3 in the simulation with the very coarse mesh and the new wall function approach and the simulation with the more refined mesh and the traditional wall function method.

Given the convergence issues that emerge when the methodology developed in this thesis is implemented, it can be deduced that the new wall function approach does not work correctly for Test Case 3. The convergence issues may be related to the fact that, as can be seen from Figure 5.3.13, the actual wall shear stresses of the cells at the rod wall sweep a fairly wide range of values while instead with the developed methodology a constant value of wall shear stress is forced to all the cells at the wall. This forcing could lead to the convergence problems encountered. To test this possible explanation two additional simulations were performed. The first simulation is carried out using the coarse mesh of Figure 4.2.3 applying the new wall function approach to the cells at the rod wall, where the actual wall shear stress values have a fairly wide range, and applying the traditional wall function approach to the cells at the sub-channel wall where the actual wall shear stress values vary over a relatively small range. The second simulation, on the other hand, is carried out again using the coarse mesh of Figure 4.2.3 applying the traditional wall function approach to the rod wall cells whose wall
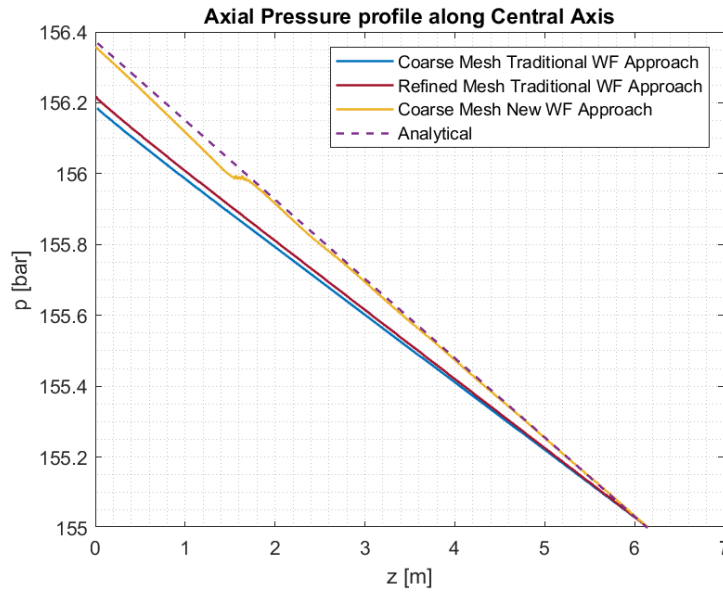
Figure 5.3.12: Axial pressure profile along the bottom left corner of the sub-channel of Test Case 3.

shear stress values vary in a fairly wide range and the new wall function approach to the cells at the sub-channel wall whose wall shear stress values are in a relatively small range. The second simulation did not present any convergence problems while the first presented the same problems encountered with the simulation by applying the new wall function approach to all the wall patches. Consequently, it can be assumed that the imposition of a constant value of the wall shear stresses on all the wall cells envisaged by the newly developed methodology causes problems of convergence if the actual range of variation of the wall shear stresses in these cells is wide. If, instead, the range of variation is limited, the methodology does not create convergence problems and gives quite satisfactory results as in the case of Test Case 2.

5.4   2x2 Fuel bundle with 3 full-length pins and 1 half-length pin

Test Case 4 consists of a single-phase flow through a 2x2 fuel bundle in a PWR with three full-length rods and one half-length rod. The coarse mesh used to discretize the domain is reported in Figure 5.4.1. The meshes is used for both the simulation with the traditional wall function approach and the new one developed for this project. The mesh in Figure 5.4.1 is obtained by combining 4 contiguous sub-channels. Each sub-channel is discretized with 8 blocks and each block is discretized with 2 cells in
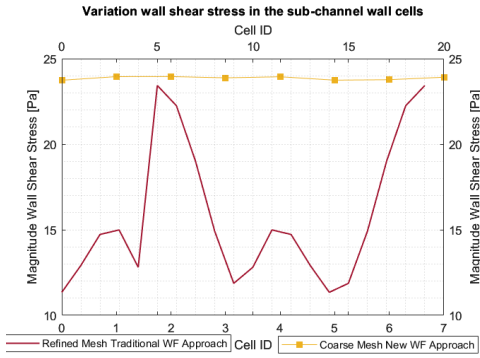
(a) Wall shear stress of the cells at the sub-channel wall of Test Case 3.
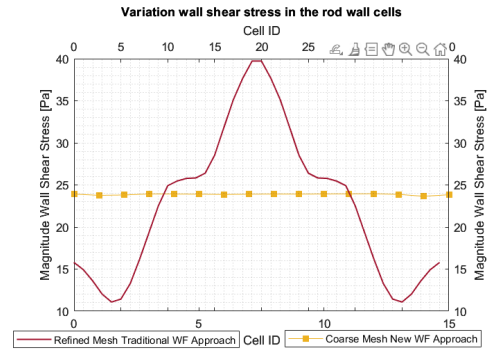
(b) Wall shear stress of the cells at the rod wall of Test Case 3.

Figure 5.3.13: Comparison of wall shear stresses obtained in the coarse mesh simulation with new wall function approach and the refined mesh one with traditional wall function approach in Test Case 3.
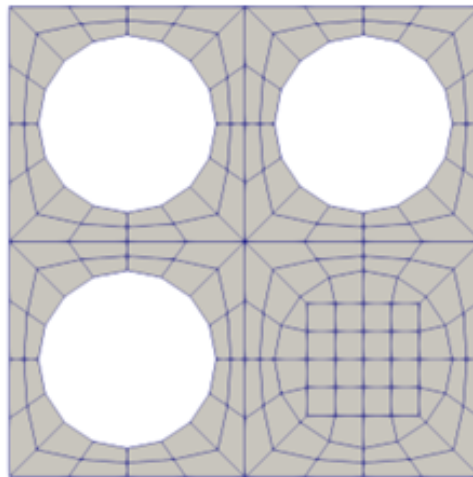
Figure 5.4.1: Fuel bundle discretized with a coarse mesh having y^+ falling in the outer region.

the radial direction, 2 cells in the circumferential direction, and 300 cells in the axial direction. In the part of the fuel bundle where the half-lenght rod is located the rod space will be occupied by the fluid in the second half of the channel and it is discretized with 12 blocks as shown in Figure 5.4.1. The results obtained in the coarse mesh simulation with the traditional wall function approach and the coarse mesh simulation with the new wall function method developed for this project are compared with the results obtained with a more refined mesh simulation with y^+ falling in the log-law region that is implemented with the traditional wall function approach. The more refined mesh is shown in Figure 5.4.2. The relatively refined mesh is obtained by discretizing each sub-channel in 8 blocks and each block is discretized with 8 cells in the radial direction, 5 cells in the circumferential direction, and 300 cells in the axial
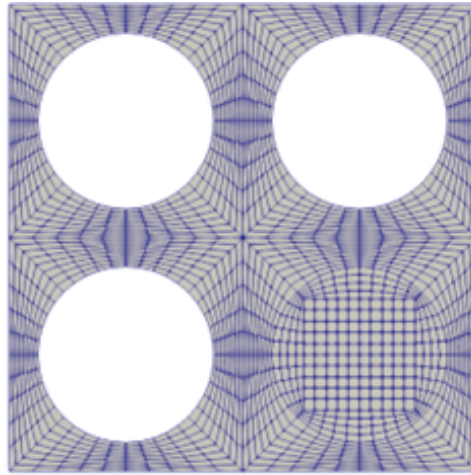
Figure 5.4.2: Fuel bundle discretized with a relatively refined mesh having y^+ falling in the log-law region.

direction. In the part of the fuel bundle where the half-length rod is located the rod space will be occupied by the fluid in the second half of the channel and it is discretized with 12 blocks as shown in Figure 5.4.2. The average y^+ of the cells at the walls at the end of the last time step are reported in Table 5.4.1.

The velocity and the temperature surface plots on the outlet cross-sectional flow area of the sub-channel are reported in Figure 5.4.4 and Figure 5.4.6 respectively.

As for the previous test cases, for a more intuitive understanding of the obtained results, during the post-processing, a constant value is associated with each cell corresponding to the cell centroid value computed directly by OpenFOAM. The velocity and temperature profiles over the lines crossing the outlet cross-sectional flow area of the fuel bundle as shown in Figure 5.4.7, are reported in Figure 5.4.8 and Figure 5.4.9 respectively.

The new coarse mesh simulation implementing the new wall function approach with the local velocity computed by OpenFOAM during the simulation seems to not capture the expected velocity profile between the rod wall and the solid wall of the fuel bundle probably for the same reasons explained in Subsection 5.3.2. Comparing the velocity profiles on diagonal 1 and diagonal 2 obtained with the new wall function approach, it can be seen that they are not equal. Being the diagonals symmetric about the 45° line the velocity profiles should be identical as happens for the simulations with the traditional wall function approach implemented. The reason for the obtained result is that the new methodology implemented causes convergence issues as in Test Case 3 that lead the simulation to not reach convergence within a reasonable number of time

Sub-channel	Patches	Simulation	Average y^+
Sub-channel 1	Rod wall	Coarse mesh and traditional WF approach	[688.4 927.4
		Refined mesh and traditional WF approach	[167.6 231.6]
		Coarse mesh and new WF approach	[840.3 876.3
Sub-channel 2	Rod wall	Coarse mesh and traditional WF approach	[645.1 826.9
		Refined mesh and traditional WF approach	[156.1 204.3]
		Coarse mesh and new WF approach	[891.0 945.3
	Sub-channel wall	Coarse mesh and traditional WF approach	[421.7 591.8]
		Refined mesh and traditional WF approach	[102.2 144.8
		Coarse mesh and new WF approach	[694.5 707.4
Sub-channel 3	Rod wall	Coarse mesh and traditional WF approach	[645.1 826.9
		Refined mesh and traditional WF approach	[156.1 204.3]
		Coarse mesh and new WF approach	[892.0 948.0
	Sub-channel wall	Coarse mesh and traditional WF approach	[421.7 591.8]
		Refined mesh and traditional WF approach	[102.2 144.8
		Coarse mesh and new WF approach	[697.9 706.3
Sub-channel 4	Rod wall	Coarse mesh and traditional WF approach	[741.2 774.4
		Refined mesh and traditional WF approach	[180.6 188.7
		Coarse mesh and new WF approach	[923.8 959.0
	Sub-channel wall	Coarse mesh and traditional WF approach	[502.6 577.4
		Refined mesh and traditional WF approach	[123.7 142.9]
		Coarse mesh and new WF approach	[630.7 715.9
	Top half-length rod	Coarse mesh and traditional WF approach	7525
		Refined mesh and traditional WF approach	9222
		Coarse mesh and new WF approach	11635

Table 5.4.1: Average y^+ values of the cells at the wall patches of the domain of Test Case 4 for the three simulations.

iterations. From a computational point of view, therefore, the results presented in this subsection are not valid since the simulation does not reach convergence, but they are equally presented because they are useful to draw conclusions on the applicability of the new methodology developed for this project. The overall expected behavior for the outlet temperature profile is captured by the three simulations. The difference between the results obtained with the simulation with the new wall function approach and the ones obtained with the simulations implementing the traditional wall function approach is probably due to the convergence issues as in Test Case 2.

The axial wall temperature profiles over the lines perpendicular to the cross-sectional area and passing through the points shown in Figure 5.4.7 are shown in Figure 5.4.10. As it is possible to notice, the simulation with the new wall function approach does not give reasonable results probably due to convergence issues that arise. Regarding the simulations with the traditional wall function approach, the temperature profiles

(a)

(b)

(c)

6.3e+00

5

4

U Magnitude

3

2

1

3.1e-06

Figure 5.4.3: Velocity range in Test Case 4.

Figure 5.4.4: Velocity surface plots on the outlet cross-sectional flow area of Test Case 4 obtained with a) very coarse mesh and traditional wall function approach, b) very coarse mesh and new wall function approach, and c) relatively refined mesh and traditional wall function approach.

along the bottom wall of the fuel bundle present roughly constant profiles in the first and last adiabatic layers and a linear increase in the first heated layer as expected. They are affected by the sudden expansion of the flow as can be seen by the peak occurring exactly at the top of the half-length rod. To better understand the behavior of the temperature near the sudden expansion of the fluid flow, the surface plots of the cross-sectional flow area of the fuel bundle at different heights after the end of the half-length rod obtained with the coarse mesh simulation and the traditional wall function approach are reported in Figure 5.4.11. The range of temperature is the one shown in Figure 5.4.5.

Looking at the surface plots, it can be seen that few millimeters after the sudden expansion the fluid flows towards the empty space above the half-length rod cooling
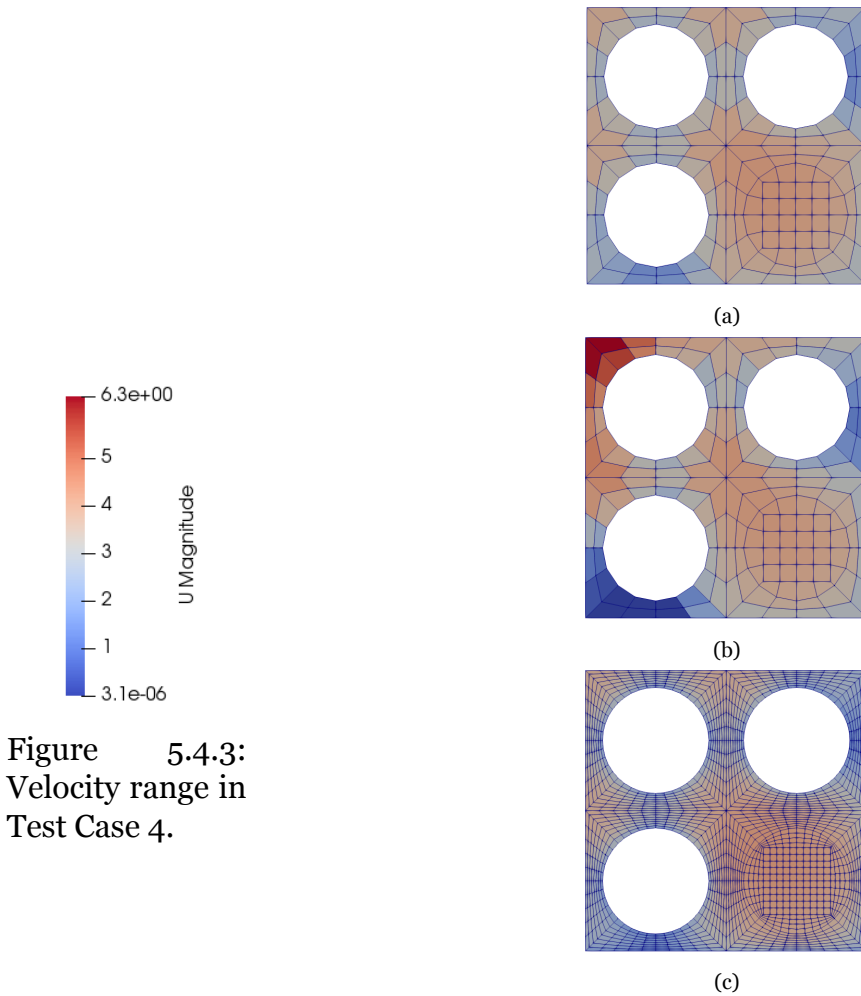
(a)

(b)

(c)

Figure 5.4.5: Temperature range in Test Case 4.
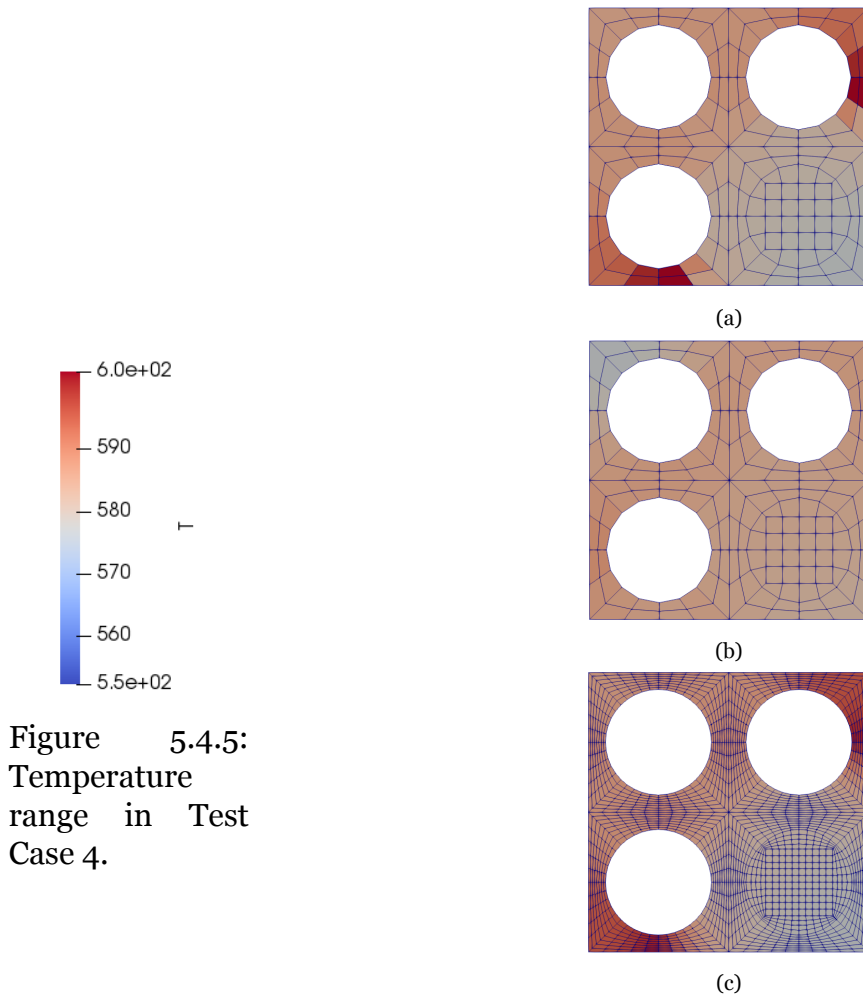
Figure 5.4.6: Temperature surface plots on the outlet cross-sectional flow area of Test Case 4 obtained with a) very coarse mesh and traditional wall function approach, b) very coarse mesh and new wall function approach, and c) relatively refined mesh and traditional wall function approach.

down less the part to the left of the center of the bottom wall and cooling down more the part to the right of the center of the bottom wall which explains the peak in temperature along the line crossing the point S_{left} and the small trough in the temperature along the line crossing the point S_{right}. Then the flow reaches a new equilibrium and the temperatures along the two lines reach the same value and subsequently start to grow linearly again given the presence of the constant heat fluxes generated by the other rods. The axial pressure profiles along the central axis of the fuel bundle are reported in Figure 5.4.12. As can be seen, the pressure profile obtained with the coarse mesh simulation implementing the new wall function approach is closer to the analytical pressure profile described by Eq. 4.18 in Chapter 4 with respect to the simulations in which the traditional wall function approach is implemented, but they don't share the

Figure 5.4.7: Post-processing lines over which the velocity and temperature profile at the outlet of the fuel bundle are plotted.
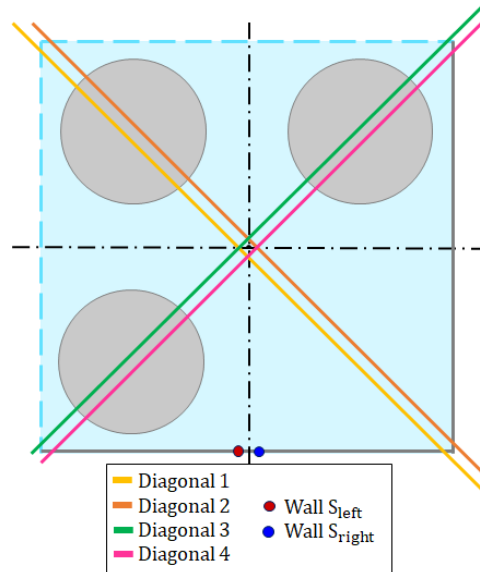
same slope in any layers of the domain. It should be also remembered that the average velocity in Eq. 4.5 used in the new wall function approach is not the actual average velocity, that is instead used to compute the analytical profile, but it is assumed to be the same along the whole fuel bundle disregarding the effect of the sudden expansion. This assumption is due to implementation issues as mentioned in Section 4.1 and the difference between the pressure profile obtained with the new methodology and the analytical profile is for sure due also to this assumption. The wall shear stresses of the cells facing the fuel bundle wall patches and the rod wall patches at the outlet cross-sectional flow area of the sub-channel are listed in Table 5.4.2. Except for the wall shear stress variations in the cell at the rod wall of the top left sub-channel in the fuel bundle, sub-channel 1, and in the cells at the sub-channel wall of the bottom right sub-channel in the fuel bundle, sub-channel 4, all the wall shear stresses vary in fairly wide ranges and the wall shear stress imposed as constant in the newly developed methodology is not even within the range. The variations of the wall shear stresses obtained in the simulation with the very coarse mesh and the new wall function approach and the simulation with the more refined mesh and the traditional wall function approach based on the log-law are reported in Figure 5.4.13, Figure 5.4.14, Figure 5.4.15, and Figure 5.4.16 for the different sub-channels.

The cell ID on the x-axis of the plots is simply the identification index of the cells facing the wall patches in the domain. As for Test Case 2, the wall shear stresses computed in
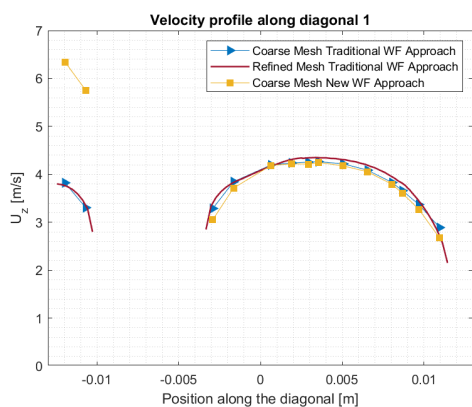
(a) Outlet velocity over diagonal 1.
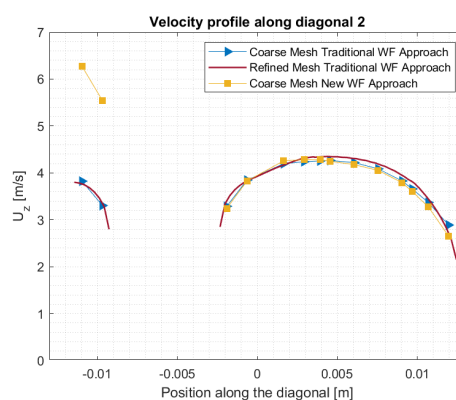
(b) Outlet velocity over diagonal 2.
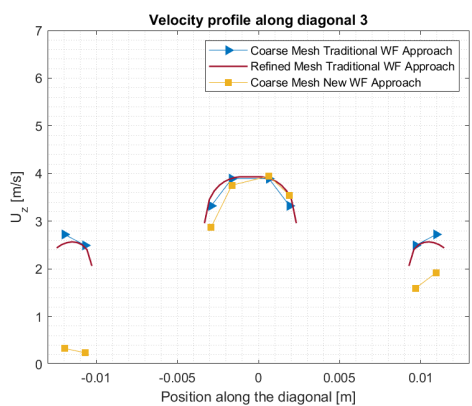
(c) Outlet velocity over diagonal 3.
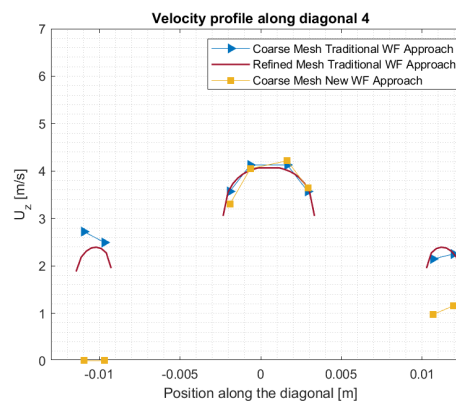
(d) Outlet velocity over diagonal 4.

Figure 5.4.8: Outlet velocity over diagonals in Test Case 4.
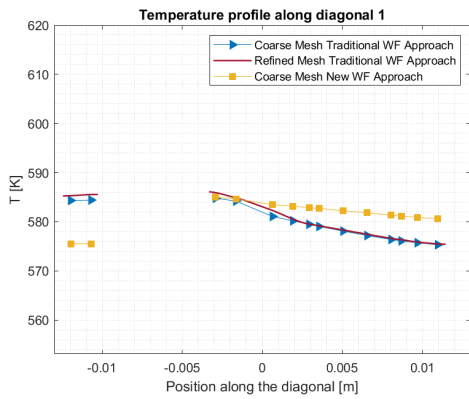
(a) Outlet temperature over diagonal 1.
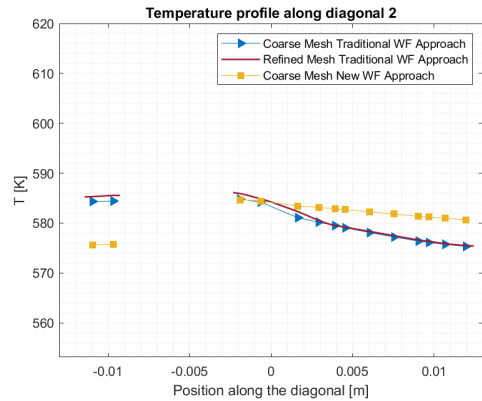
(b) Outlet temperature over diagonal 2.
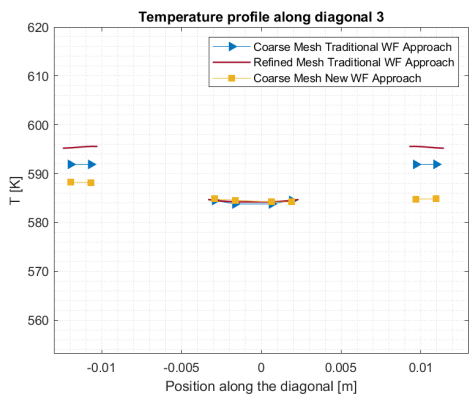
(c) Outlet temperature over diagonal 3.
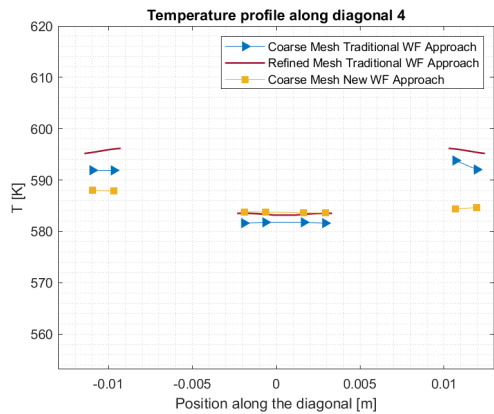
(d) Outlet temperature over diagonal 4.

Figure 5.4.9: Outlet temperature over diagonals in Test Case 4.
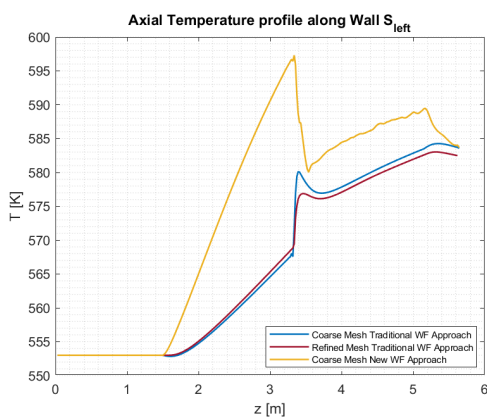
(a) Wall temperature profile over the line perpendicular to the cross-sectional area and passing through the point S_{left}.
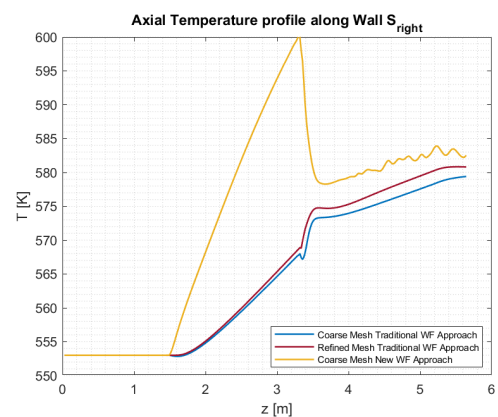
(b) Wall temperature profile over the line perpendicular to the cross-sectional area and passing through the point S_{right}.

Figure 5.4.10: Axial wall temperature profiles in Test Case 4.

(a) At z = 3.329 m. (b) At z = 3.334 m. (c) At z = 3.429 m. (d) At z = 3.55 m. (e) At z = 3.75 m.
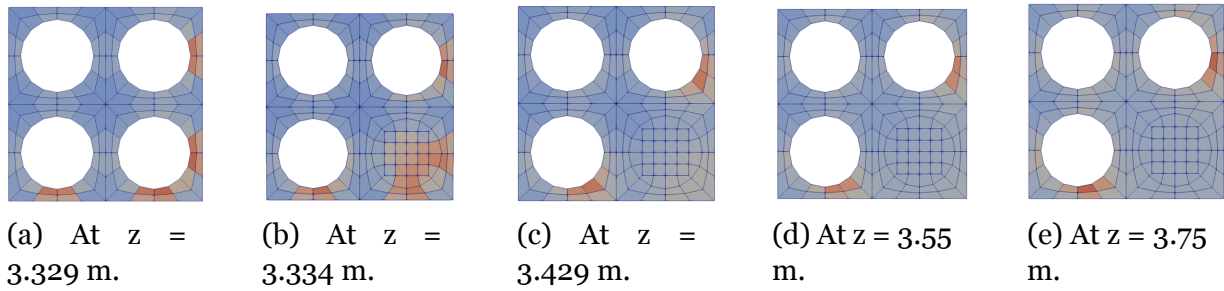
Figure 5.4.11: Temperature surface plots at different heights around the sudden expansion obtained with coarse mesh simulation with traditional wall function approach.
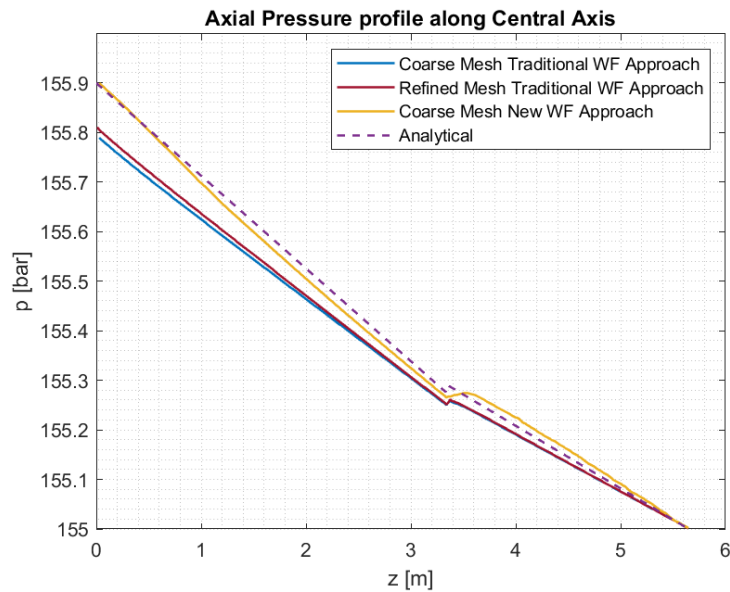
Figure 5.4.12: Axial pressure profile along the central axis of the fuel bundle.

the refined mesh simulation are not constant since the geometry of the problem is not axisymmetric.

The wall shear stresses in the rod wall cells and the sub-channel wall cells imposed by the new wall function approach in sub-channel 3 are not constant in all the wall cells. This is probably due to the fact that the velocity between the rod wall and the solid wall of sub-channel 3 is equal to zero implementing the new wall function approach for the reasons explained in Subsection 5.3.1, so it can be deduced that the new approach does not work as expected in this part of the fuel bundle between the two solid walls in sub-channel 3. The simulation of Test Case 3 applying the new wall function approach and implementing a more refined mesh between the solid walls still led to convergence issues and the intention of this project is to test the developed methodology in a mesh as coarse as possible, therefore a simulation that increases the discretization of the flow passage between the two solid walls is not performed as it could not lead to further

Sub-channel	Patches	Simulation	Wall shear stres
Sub-channel 1	Rod wall	Refined mesh and traditional WF approach	[11.4, 16.4]
		Coarse mesh and new WF approach	21.2 Pa
Sub-channel 2	Rod wall	Refined mesh and traditional WF approach	[4, 19] Pe
		Coarse mesh and new WF approach	22.7 Pa
	Sub-channel wall	Refined mesh and traditional WF approach	[4, 14.2] P
		Coarse mesh and new WF approach	22.7 Pa
Sub-channel 3	Rod wall	Refined mesh and traditional WF approach	[4, 19] Pe
		Coarse mesh and new WF approach	22.7 Pa
	Sub-channel wall	Refined mesh and traditional WF approach	[4, 14.2] P
		Coarse mesh and new WF approach	22.7 Pa
Sub-channel 4	Sub-channel wall	Refined mesh and traditional WF approach	[11.6, 17.5]
		Coarse mesh and new WF approach	18.2 Pa

Table 5.4.2: Wall shear stresses obtained for Test Case 4 in the simulation with the very coarse mesh and the new wall function approach and the simulation with the more refined mesh and the traditional wall function method.

Figure 5.4.13: Comparison of wall shear stresses obtained in the coarse mesh simulation with new wall function approach and the refined mesh one with traditional wall function approach for sub-channel 1 in Test Case 4.

relevant results.

Given the convergence issues, it can be deduced that the new wall function approach does not work correctly for Test Case 4 too as for Test Case 3. The possible explanation for the convergence issues could be the one discussed already in the previous test case.

5.5 Discussion

The results presented in the previous chapter can be summarized by three main points.

1. The new methodology developed in this project fails to capture reasonable velocity values between two solid walls if the flow passage between them is not discretized with a reasonable number of cells, as seen in Test Case 3 and Test Case
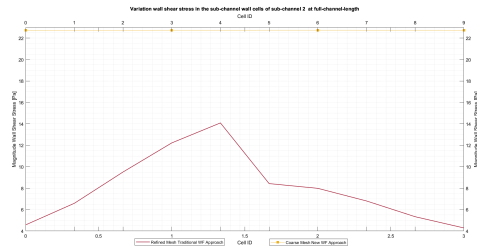
(a) Wall shear stress of the cells at the sub-channel wall of subchannel 2 in Test Case 4.
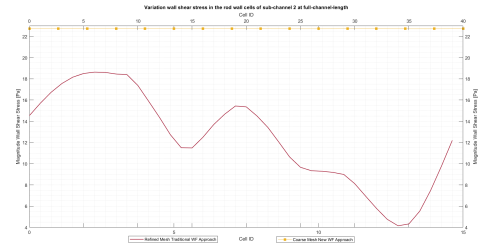
(b) Wall shear stress of the cells at the rod wall of subchannel 2 in Test Case 4.

Figure 5.4.14:   Comparison of wall shear stresses obtained in the coarse mesh simulation with new wall function approach and the refined mesh one with traditional wall function approach for sub-channel 2 in Test Case 4.
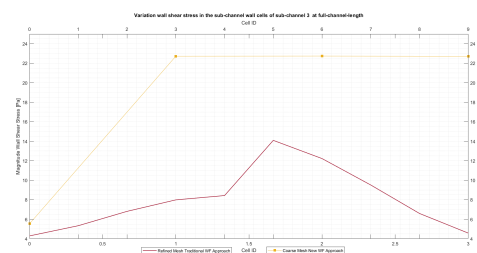
(a) Wall shear stress of the cells at the sub-channel wall of subchannel 3 in Test Case 4.
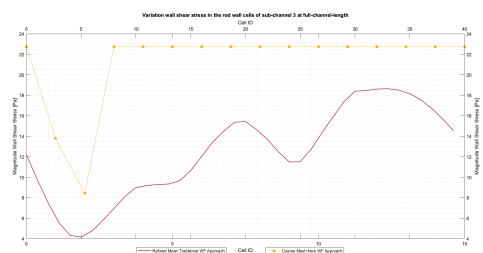
(b) Wall shear stress of the cells at the rod wall of subchannel 3 in Test Case 4.

Figure 5.4.15:   Comparison of wall shear stresses obtained in the coarse mesh simulation with new wall function approach and the refined mesh one with traditional wall function approach for sub-channel 3 in Test Case 4.

4. Probably the need to use a minimum number of cells between two solid walls is related to the mathematical formulation of the new wall function approach which presents the local velocity of a cell at the wall to the denominator.

2. The perfect match between the axial pressure profile obtained with the new wall function approach and the analytical pressure profile was obtained only in Test Case 1, while in Test Case 2 the two profiles are similar but not identical. The explanation is probably due to the axisymmetry of the considered geometries. In the case of Test Case 1, the geometry is axisymmetric, therefore the actual value of the wall shear stress is constant as well as that imposed by the new methodology, while in Test Case 2, the current values of the wall shear stress of the cells at the wall are not constant but they sweep in a range. Since this range is relatively small and the constant value imposed by the new methodology is within it, the new wall function approach seems to still give quite satisfactory results.
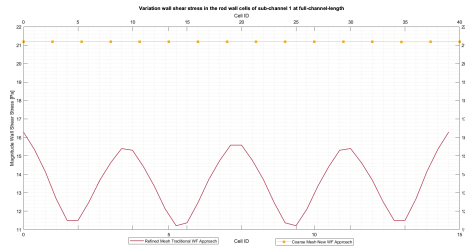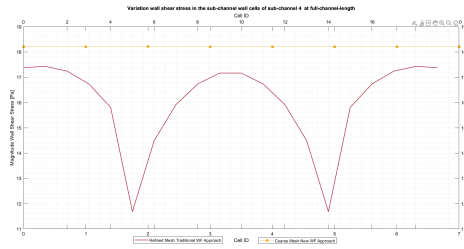
Figure 5.4.16: Comparison of wall shear stresses obtained in the coarse mesh simulation with new wall function approach and the refined mesh one with traditional wall function approach for sub-channel 4 in Test Case 4.

3. The relationship between the actual variation of the wall shear stresses of the wall cells and the wall shear stress imposed as constant by the newly developed methodology is the fundamental factor on which the applicability of the methodology itself depends. If the actual variation of the wall shear stress sweeps a wide range, the imposition of a constant wall shear stress on all the cells at the walls foreseen by the new wall function approach leads to considerable convergence problems, not giving conclusive results. On the other hand, if instead the range of variation is relatively small, the methodology seems to give acceptable results as in Test Case 2.

Chapter 6

Conclusions

The main objective of this thesis was to develop an innovative approach able to exploit the capabilities of sub-channel and CFD codes and at the same time overcome their limitations. To reach this goal, a new methodology was developed and tested on four test cases for which the sub-channel codes are the state-of-the-art analysis method. The intention behind the new methodology is to produce 3D CFD-level results with accuracy at least as good as those obtained with sub-channel codes while avoiding the geometrical approximation associated with traditional codes and circumventing the prohibitive computational costs associated with conventional CFD simulation. From the results obtained with the four test cases summarized in the three points listed in Section 5.5, it can be concluded that the methodology has a limited applicability and before proceeding with the extension of this new wall function approach to single-phase problems with 3D prevailing phenomena and two-phase problems it is necessary to solve the convergence issues that emerge for some types of cases. Additionally, the methodology, due to its mathematical formulation, should be applied exclusively in mesh with enough refined discretization to properly capture the velocity behavior between two solid walls, leading to a dependency between the performance of the method and the mesh used to discretize the domain. This thesis served also as feasibility study for the use of the CFD software OpenFOAM with the aim to extend the methodology to two-phase problems. It can be stated that OpenFOAM is adequate for the developed methodology, but has limitations in cases where the average flow parameters have to be evaluated and used during the simulation and not in the post-processing phase.

6.1 Future Work

In the event that convergence issues arising in the application of the new methodology developed for this project are resolved, possible next steps for future investigations of the methodology are listed below.

6.1.1 Average velocity over cross-sectional flow area

The assumption of using in the mathematical formulation of the new wall function approach a constant mean velocity given in user input for the entire problem domain reduces the applicability of the methodology to problems in which the mean velocity can be correctly evaluated before the simulation and in which the density and cross-sectional flow area remain constant throughout the domain. To reduce these limitations a method for calculating and inputting the average flow parameters on the cross-sections at the different axial positions has to be developed.

6.1.2 Temperature-dependent density of the fluid

The dependence of the fluid density on the temperature has to be introduced.

6.1.3 New wall function approach for the turbulent thermal diffusivity

The realization of a new wall function approach equivalent to the one applied to the turbulent kinematic viscosity applicable to the turbulent thermal diffusivity can be investigated.

6.1.4 Substitute the local velocity computed by OpenFOAM in the denominator

The mathematical formulation of the conditional statement applied to the turbulent kinematic viscosity has limitations due to the presence of the local velocity of the cells at the wall in the denominator which, in the presence of relatively narrow flow passages, creates a strong dependence on the applicability of the methodology to the discretization of the mesh used for split the domain. This limitation can be evaded if the local velocity of the cell at the wall is described by an expression and not computed

directly from OpenFOAM. Two possible modification of the developed methodology using expressions to describe the local velocity are reported in Appendix A and Appendix B and they can be used as starting points for further investigation.

6.2   Final Words

The methodology developed in this thesis is only one of the many possible options to achieve the objectives underlying the development of the coarse grid CFD approach. Coarse-grid CFD approach can be employed as a complementary and potentially substitutive approach to resolved CFD and subchannel codes/porous medium modeling and for this reason it will still be an interesting area of research in the coming years.

Bibliography

[1] Anglart, Henryk. *Thermal-Hydraulics in Nuclear Systems*. Henryk Anglart, 2010.

[2] Schultz, R.R. "4 - Role of thermal-hydraulics in nuclear power plants: Design and safety". In: *Thermal-Hydraulics of Water Cooled Nuclear Reactors*. Ed. by Francesco D'Auria. Woodhead Publishing, 2017, pp. 143–166. isbn: 978-0-08-100662-7. url: https://www.sciencedirect.com/science/article/pii/B978008100662700004X.

[3] Thunberg, Wilhelm. "Thermal Hydraulics Simulations for Nuclear Energy". Uppsala, Sweden, 2022.

[4] Bestion, D. "11 - The structure of system thermal-hydraulic (SYS-TH) code for nuclear energy applications". In: *Thermal-Hydraulics of Water Cooled Nuclear Reactors*. Ed. by Francesco D'Auria. Woodhead Publishing, 2017, pp. 639–727. isbn: 978-0-08-100662-7. url: https://www.sciencedirect.com/science/article/pii/B9780081006627000117.

[5] Avramova, Maria. "Developments in thermal-hydraulic sub-channel modeling for whole core multi-physics simulations". In: *Nuclear Engineering and Design* 358 (2020), p. 110387. issn: 0029-5493. url: https://www.sciencedirect.com/science/article/pii/S0029549319304182.

[6] Moorthi, A., Kumar Sharma, Anil, and Velusamy, K. "A review of sub-channel thermal hydraulic codes for nuclear reactor core and future directions". In: *Nuclear Engineering and Design* 332 (2018), pp. 329–344. issn: 0029-5493. url: https://www.sciencedirect.com/science/article/pii/S0029549318302681.

[7] Liu, B., He, S., Moulinec, C., and Uribe, J. "Sub-channel CFD for nuclear fuel bundles". In: *Nuclear Engineering and Design* 355 (2019), p. 110318. issn: 0029-5493. url: https://www.sciencedirect.com/science/article/pii/S002954931930353X.

[8] Yang, Bao-Wen, Ninokata, Hisashi, Long, Jianping, Liu, Aiguo, and Han, Bin. "Subchannel analysis – Current practice and development for the future". In: *Nuclear Engineering and Design* 385 (2021), p. 111477. issn: 0029-5493. url: https://www.sciencedirect.com/science/article/pii/S0029549321004295.

[9] Wang Jun, Allison Chris and Judy, Hohorst. *Nuclear Power Plant Design and Analysis Codes. Development, Validation, and Application.* Woodhead Publishing Series in Energy, 2021.

[10] Agency, IAEA International Atomic Energy. *Summary review on the application of computational fluid dynamics in nuclear power plant design.* Tech. rep. NR-T-1.20. International Atomic Energy Agency, 2022. url: https://www.pub.iaea.org/MTCD/Publications/PDF/PUB1932_web.pdf.

[11] Andersson, Ronnie, Andersson, Bengt, Chopard, Fabrice, and Norén, Tommy. "Development of a multi-scale simulation method for design of novel multiphase reactors". In: *Chemical Engineering Science* 59.22 (2004). ISCRE18, pp. 4911–4917. issn: 0009-2509. url: https://www.sciencedirect.com/science/article/pii/S000925090400538X.

[12] Martelli, Daniele, Forgione, Nicola, Barone, Gianluca, and di Piazza, Ivan. "Coupled simulations of the NACIE facility using RELAP5 and ANSYS FLUENT codes". In: *Annals of Nuclear Energy* 101 (2017), pp. 408–418. issn: 0306-4549. url: https://www.sciencedirect.com/science/article/pii/S0306454916302407.

[13] Aumiller, D.L., Tomlinson, E.T., and Weaver, W.L. "An integrated relap5-3d and multiphase cfd code system utilizing a semi-implicit coupling technique". In: *Nuclear Engineering and Design* 216.1 (2002), pp. 77–87. issn: 0029-5493. url: https://www.sciencedirect.com/science/article/pii/S0029549301005222.

[14] Anderson, Nolan, Hassan, Yassin, and Schultz, Richard. "Analysis of the hot gas flow in the outlet plenum of the very high temperature reactor using coupled RELAP5-3D system code and a CFD code". In: *Nuclear Engineering and Design* 238.1 (2008), pp. 274–279. issn: 0029-5493. url: `https://www.sciencedirect.com/science/article/pii/S0029549307003925`.

[15] Guelfi, Antoine, Bestion, Dominique, Boucker, Marc, Boudier, Pascal, Fillion, Philippe, Grandotto, Marc, Hérard, Jean-Marc, Hervieu, Eric, and Péturaud, Pierre. "NEPTUNE: A New Software Platform for Advanced Nuclear Thermal Hydraulics". In: *Nuclear Science and Engineering* 156.3 (2007), pp. 281–324. url: `https://doi.org/10.13182/NSE05-98`.

[16] Bestion, D., Lucas, D., Anglart, Henryk, Niceno, Bojan, and Vyskocil, Ladislav. "Multi-Scale Thermalhydraulic Analyses Performed in NURESIM and NURISP Projects". In: vol. 4. July 2012. doi: `10.1115/ICONE20-POWER2012-54891`.

[17] Papukchiev, A, Lerchl, G, Weis, J, Scheuerer, M, and Austregesilo, H. "Development of a coupled 1D-3D thermal-hydraulic code for nuclear power plant simulation and its application to a pressurized thermal shock scenario in PWR". In: (2011).

[18] Li, Wei, Wu, Xiaoli, Zhang, Dalin, Su, Guanghui, Tian, Wenxi, and Qiu, Suizheng. "Preliminary study of coupling CFD code FLUENT and system code RELAP5". In: *Annals of Nuclear Energy* 73 (2014), pp. 96–107. issn: 0306-4549. url: `https://www.sciencedirect.com/science/article/pii/S0306454914003053`.

[19] Toti, A., Vierendeels, J., and Belloni, F. "Improved numerical algorithm and experimental validation of a system thermal-hydraulic/CFD coupling method for multi-scale transient simulations of pool-type reactors". In: *Annals of Nuclear Energy* 103 (2017), pp. 36–48. issn: 0306-4549. url: `https://www.sciencedirect.com/science/article/pii/S030645491630843X`.

[20] ANSYS, Inc. *7.2.3 Porous Media Conditions*. 2009. url: `https://www.afs.enea.it/project/neptunius/docs/fluent/html/ug/node233.htm#sect-porous-mv`.

[21] Hu, Rui and Fanning, Thomas H. "Development of a momentum source model for wire-wrapped rod bundles". In: The 14th International Topical Meeting on Nuclear Reactor Thermal Hydraulics (NURETH-14) (2011).

[22] Hu, Rui and Fanning, Thomas H. "A momentum source model for wire-wrapped rod bundles—Concept, validation, and application". In: *Nuclear Engineering and Design* 262 (2013), pp. 371–389. issn: 0029-5493. url: `https://www.sciencedirect.com/science/article/pii/S0029549313002495`.

[23] Roelofs, F., Gopala, V.R., Chandra, L., Viellieber, M., and Class, A. "Simulating fuel assemblies with low resolution CFD approaches". In: *Nuclear Engineering and Design* 250 (2012), pp. 548–559. issn: 0029-5493. url: `https://www.sciencedirect.com/science/article/pii/S0029549312003056`.

[24] Viellieber, Mathias, Dietrich, Philipp, and Class, Andreas. "Coarse☐Grid☐CFD for a Wire Wrapped Fuel Assembly". In: *PAMM* 13 (Dec. 2013). doi: `10.1002/pamm.201310154`.

[25] Viellieber, Mathias and Class, Andreas. "Coarse-Grid-CFD for the Thermal Hydraulic Investigation of Rod-Bundles". In: vol. 15. Mar. 2015. doi: `10.1002/pamm.201510239`.

[26] Capone, Luigi, Benhamadouche, Sofiane, and Hassan, Yassin A. "Source terms modeling for spacer grids with mixing vanes for CFD simulations in nuclear reactors". In: *Computers Fluids* 126 (2016), pp. 141–152. issn: 0045-7930. url: `https://www.sciencedirect.com/science/article/pii/S0045793015003825`.

[27] Roelofs, F. and Doolaard, H. "Towards 3D CFD Models of PWR Fuel Assemblies at Reasonable Computational Costs". In: The 17th International Topical Meeting on Nuclear Reactor Thermal Hydraulics (NURETH-17) (2017).

[28] Mikuž, B. and Roelofs, F. "Low resolution modelling of mixing phenomena in PWR fuel assemblies". In: *Nuclear Engineering and Design* 360 (2020), p. 110504. issn: 0029-5493. url: `https://www.sciencedirect.com/science/article/pii/S0029549319305357`.

[29] Hanna, Botros, Dinh, Nam, Youngblood, Robert, and Bolotnov, Igor. "Coarse-Grid Computational Fluid Dynamic (CG-CFD) Error Prediction using Machine Learning". In: (Oct. 2017).

[30] Greenshields, Christopher and Weller, Henry. *Notes on Computational Fluid Dynamics: General Principles*. Reading, UK: CFD Direct Ltd, 2022.

[31] Anderson, J. D. "Governing Equations of Fluid Dynamics". In: *Computational Fluid Dynamics: An Introduction*. Ed. by John F. Wendt. Berlin, Heidelberg: Springer Berlin Heidelberg, 1992, pp. 15–51. isbn: 978-3-662-11350-9. url: `https://doi.org/10.1007/978-3-662-11350-9_2`.

[32] Wikipedia contributors. *Conservation of mass — Wikipedia, The Free Encyclopedia*. 2023. url: `https://en.wikipedia.org/w/index.php?title=Conservation_of_mass&oldid=1153046006`.

[33] Wikipedia contributors. *Newton's laws of motion — Wikipedia, The Free Encyclopedia*. 2023. url: `https://en.wikipedia.org/w/index.php?title=Newton27s_laws_of_motion&oldid=1150369343`.

[34] Wikipedia contributors. *First law of thermodynamics — Wikipedia, The Free Encyclopedia*. 2023. url: `https://en.wikipedia.org/w/index.php?title=First_law_of_thermodynamics&oldid=1152396110`.

[35] Eymard, R., Herbin, and Gallouët, T. "Finite volume method". In: *Scholarpedia* 5.6 (2010), p. 9835. doi: `10.4249/scholarpedia.9835`.

[36] ANSYS, Inc. *Mesh Quality*. url: `https://www.afs.enea.it/project/neptunius/docs/fluent/html/ug/node167.htm#:~:text=Skewness20is20defined20as20the,accuracy20and20destabilize20the20solution`.

[37] Sezai, Ibrahim. *Practical Guidelines for CFD Simulation*. 2015. url: `https://opencourses.emu.edu.tr/pluginfile.php/13882/mod_resource/content/1/chapter207.pdf`.

[38] SimScale. *Mesh Quality*. url: `https://www.simscale.com/docs/simulation-setup/meshing/mesh-quality/`.

[39] idealsimulations. *Turbulence Models in CFD*. url: `https://www.idealsimulations.com/resources/turbulence-models-in-cfd/`.

[40] Gloor, Michael, Obrist, Dominik, and Kleiser, Leonhard. "Linear stability and acoustic characteristics of compressible, viscous, subsonic coaxial jet flow". In: *Physics of Fluids* 25.8 (Aug. 2013). issn: 1070-6631. eprint: `https://pubs.aip.org/aip/pof/article-pdf/doi/10.1063/1.4816368/13983299/084102\_1\_online.pdf`. url: `https://doi.org/10.1063/1.4816368`.

[41] Reynolds, Osborne. "An Experimental Investigation of the Circumstances Which Determine Whether the Motion of Water Shall Be Direct or Sinuous, and of the Law of Resistance in Parallel Channels." In: *Proceedings of the Royal Society of London* 35 (1883), pp. 84–99. issn: 03701662. url: `http : / / www . jstor.org/stable/114354`.

[42] Rahman, Fasi Ur. *Laminar Flow and Turbulent Flow*. url: `https : / / theconstructor.org/fluid-mechanics/laminar-turbulent-flow/559432/`.

[43] Prandtl, L. "Über Flüssigkeitsbewegung bei sehr kleiner Reibung". In: *Vier Adhandlungen zur Hydrodynamik und Aerodynamik* (1928), pp. 1–10. url: `https://ntrs.nasa.gov/archive/nasa/casi.ntrs.nasa.gov/19930090813. pdf`.

[44] Hourigan, Kerry. *Vorticity Generation 1:Introduction and Key Concepts*. 2019. url: `http://vortex.compute.dtu.dk/coursematerial/KERRY/Copenhagen-KH-Lecture-1.pdf`.

[45] Kolmogorov, A. N. "The Local Structure of Turbulence in Incompressible Viscous Fluid for Very Large Reynolds Numbers". In: *Proceedings: Mathematical and Physical Sciences* 434.1890 (1991), pp. 9–13. issn: 09628444. url: `http://www.jstor.org/stable/51980`.

[46] OpenFOAM. *OpenFOAM: User Guide v2112. Reynolds Averaged Simulation (RAS)*. url: `https://www.openfoam.com/documentation/guides/v2112/doc/ guide-turbulence-ras.html`.

[47] Boussinesq, Joseph. *Essay on the theory of running waters*. Paris: National Printing, 1877.

[48] Bayón, Arnau. *Introduction to CFD. Wall functions*. url: `https://cfd.blogs. upv.es/turbulence/wall-functions/`.

[49] Wikipedia contributors. *Shear stress — Wikipedia, The Free Encyclopedia*. [Online; accessed 15-May-2023]. 2023. url: `https://en.wikipedia.org/w/ index.php?title=Shear_stress&oldid=1148032787`.

[50] Economon, Thomas D. *Turbulent Flat Plate*. url: `https://su2code.github. io/tutorials/Turbulent_Flat_Plate/`.

[51]   Wikipedia contributors. *Law of the wall — Wikipedia, The Free Encyclopedia.* [Online; accessed 15-May-2023]. 2023. url: `https://en.wikipedia.org/w/index.php?title=Law_of_the_wall&oldid=1146016322`.

[52]   101, Fluid Mechanics. *Wall Functions.* 2018. url: `https://www.youtube.com/watch?v=fJDYtEGMgzs&t=6s`.

[53]   Miguntanna, Nadeeka S., Moses, Hamish, Sivakumar, Muttucumaru, Yang, Shu-Qing, Enever, Keith James, and Riaz, Muhammad Zain Bin. "Re-examining log law velocity profile in smooth open channel flows". In: *Environmental Fluid Mechanics* 20.1890 (2020), pp. 953–986. issn: 1573-1510. url: `https://doi.org/10.1007/s10652-019-09733-6`.

[54]   Kudela, Henryk. *Turbulent flow.* url: `http://www.itcmp.pwr.wroc.pl/~znmp/dydaktyka/fundam_FM/Lecture_no3_Turbulent_flow_Modelling.pdf`.

[55]   Ting, David S-K. "Chapter 6 - Wall Turbulence". In: *Basics of Engineering Turbulence.* Ed. by David S-K. Ting. Academic Press, 2016, pp. 119–138. isbn: 978-0-12-803970-0. url: `https://www.sciencedirect.com/science/article/pii/B9780128039700000064`.

[56]   Walia, Rajat. *Wall Function Approach.* url: `https://www.everyeng.com/blog/view/9424677f/Wall20Function20Approach`.

[57]   101, Fluid Mechanics. *Thermal Wall Functions.* 2018. url: `https://www.youtube.com/watch?v=2bJ-5gaeSE0&t=1132s`.

[58]   Bredberg, Jonas. *On the Wall Boundary Condition for Turbulence Models.* Jan. 2000.

[59]   101, Fluid Mechanics. *Wall Functions for Turbulent Kinetic Energy.* 2019. url: `https://www.youtube.com/watch?v=zSIgKsQSa9k`.

[60]   Wikipedia contributors. *OpenFOAM — Wikipedia, The Free Encyclopedia.* 2022. url: `https://en.wikipedia.org/w/index.php?title=OpenFOAM&oldid=1130063831`.

[61]   Foundation, The OpenFOAM. *OpenFOAM and The OpenFOAM Foundation.* url: `https://openfoam.org/`.

[62]   Greenshields, Christopher. *OpenFOAM v10 User Guide.* London, UK: The OpenFOAM Foundation, 2022. url: `https://doc.cfd.direct/openfoam/user-guide-v10`.

[63] DeGroot, Chris. *Understanding the OpenFOAM Case Structure.* 2020. url:
`https : / / maplekeylabs . com / understanding - the - openfoam - case -`
`structure/`.

[64] Liu, Fangqing. *A Thorough Description Of How Wall Functions Are*
Implemented In OpenFOAM. In Proceedings of CFD with OpenSource
Software. Ed. by Edited by Nilsson. H. 2016. url: `http://www.tfd.chalmers.`
`se/~hani/kurser/OS_CFD_2016`.

[65] Spalding, D. B. "A Single Formula for the "Law of the Wall"". In: *Journal of*
Applied Mechanics 28 (1961), pp. 455–458.

[66] OpenFOAM. *OpenFOAM: User Guide v2112. nutkRoughWallFunction.* url:
`https : / / www . openfoam . com / documentation / guides / v2112 / doc / guide -`
`bcs-wall-turbulence-nutkRoughWallFunction.html`.

[67] OpenFOAM. *OpenFOAM: User Guide v2112. nutURoughWallFunction.* url:
`https : / / www . openfoam . com / documentation / guides / v2112 / doc / guide -`
`bcs-wall-turbulence-nutURoughWallFunction.html`.

[68] Thiele, Roman. "Mechanistic Modeling of Wall-Fluid Thermal Interactions for
Innovative Nuclear Systems". Stockholm, Sweden, 2015.

[69] OpenFOAM. *OpenFOAM: User Guide v2112.*
alphatJayatillekeWallFunctionFvPatchScalarField Class Reference. url:
`https://www.openfoam.com/documentation/guides/latest/api/classFoam_`
`1_1compressible_1_1alphatJayatillekeWallFunctionFvPatchScalarField.`
`html#details`.

[70] OpenFOAM. *OpenFOAM: User Guide*
v2112. alphatWallFunctionFvPatchScalarField Class Reference. url: `https://`
`www . openfoam . com / documentation / guides / latest / api / classFoam _ 1 _`
`1compressible_1_1alphatWallFunctionFvPatchScalarField.html#details`.

[71] WINTERTON, R.H.S. "CHAPTER 6 - Fluid Flow". In: *Thermal Design of*
Nuclear Reactors. Ed. by R.H.S. WINTERTON. Pergamon, 1981, pp. 84–105.
isbn: 978-0-08-024215-6. url: `https : / / www . sciencedirect . com / science /`
`article/pii/B9780080242156500103`.

[72] Wikipedia contributors. *Fanning friction factor — Wikipedia, The Free*
Encyclopedia. 2022. url: `%7Bhttps://en.wikipedia.org/w/index.php?title=`
`Fanning_friction_factor&oldid=1063815783%7D`.

[73] Abbas, Mustafa. *Wall Functions in OpenFOAM — Implementation in Code.* 2020. url: `https : / / medium . com / @mustafaabbs2 / wall - functions - in - openfoam-implementation-in-code-959eccc4e311`.

[74] Wikipedia contributors. *Hydraulic diameter — Wikipedia, The Free Encyclopedia.* 2023. url: `https : / / en . wikipedia . org / w/index.php?title=%20Hydraulic_diameter&oldid=1146067751`.

[75] Kyriakopoulos, Vasileios, Tano, Mauricio E., and Ragusa, Jean C. "Development of a Single-Phase, Transient, Subchannel Code, within the MOOSE Multi-Physics Computational Framework". In: *Energies* 15.11 (2022). issn: 1996-1073. url: `https://www.mdpi.com/1996-1073/15/11/3948`.

[76] Wikipedia contributors. *Turbulence kinetic energy — Wikipedia, The Free Encyclopedia.* [Online; accessed 24-May-2023]. 2023. url: `https : / / en . wikipedia . org/w/index.php?title=Turbulence_kinetic_energy&oldid= 1154125457`.

[77] Mehta, Dhruv, Radhakrishnan, Adithya Krishnan Thota, Lier, Jules B. van, and Clemens, Francois H.L.R. "Assessment of numerical methods for estimating the wall shear stress in turbulent Herschel–Bulkley slurries in circular pipes". In: *Journal of Hydraulic Research* 59.2 (2021), pp. 196–213. url: `https://doi. org/10.1080/00221686.2020.1744751`.

[78] Wikipedia contributors. *Darcy–Weisbach equation — Wikipedia, The Free Encyclopedia.* [Online; accessed 26-May-2023]. 2023. url: `https : / / en . wikipedia.org/w/index.php?title=DarcyE28093Weisbach_equation&oldid= 1146657509`.

[79] University, Seoul National. *General Remarks about Local Pressure Drops.* url: `https://ocw.snu.ac.kr/sites/default/files/NOTE/Lecture05-2.pdf`.

[80] Wikipedia contributors. *ParaView — Wikipedia, The Free Encyclopedia.* [Online; accessed 24-May-2023]. 2023. url: `https://en.wikipedia.org/w/ index.php?title=ParaView&oldid=1146589776`.

[81] Yunus A. Cengel, Afshin J. Ghajar. *Heat and Mass Transfer: Fundamentals Applications Fourth Edition.* 2011. url: `https://slidetodoc.com/heat-and-mass-transfer-fundamentals-applications-fourth-edition-7/`.

[82] Sellens, Rick. *Power Law Profiles in Pipes.* url: `https : / / me . queensu . ca / People/Sellens/PowerLaw.html`.

Appendix - Contents

Appendix A

New wall function method with u_P described by the power law

As deduced from the results presented in Chapter 5, one of the major problems related to the newly developed methodology is its mathematical formulation which includes the presence of the local velocity of the centroid of the cell at the wall computed by OpenFOAM u_P at the denominator as shown in Eq. 4.5. The presence of u_P at the denominator leads to a strong dependency on the refinement of the mesh used to discretize the domain in problems in which relatively narrow flow passages are present because in case the space between two solid walls with no-slip boundary condition imposed is discretized with too few cells the velocity is captured as equal to zero and the new wall function approach seems to not work as expected as seen for Test Case 5 in sub-channel 3. To avoid this dependency an alternative solution is to substitute the local velocity computed by OpenFOAM with an expression able to describe it. In this appendix, the solution presented consists in exploiting the 1/n power law to describe the local velocity of the cell at the wall.

The 1/n power law is an expression that well describes the velocity profile of a turbulent flow in a pipe and it is reported in Eq. A.1 [82].

$$\frac{U(r)}{u_{max}} = \left(1 - \frac{r}{R}\right)^{\frac{1}{n}} \tag{A.1}$$

r is the radial coordinate shown in Figure **??** that can be converted in y according to the relation $y = R - r$ obtaining the Eq. A.2.

$$\frac{U(y)}{u_{max}} = \left(\frac{y}{R}\right)^{\frac{1}{n}} \tag{A.2}$$

R is the radius of the pipe, n is given by the Eq. A.3 [82] and u_{max} is obtained by the definition of average velocity over the cross-sectional flow area reported in Eq. A.4.

$$n = (4C_f)^{-\frac{1}{2}} \tag{A.3}$$

$$U_{avg} = \frac{\int U(r)dA}{A} = \frac{\int U(r)2\pi r dr}{2\pi R^2} = \frac{2u_{max}}{R^2} \int_0^R r\left(-r/R\right)^{1/n} dr \tag{A.4}$$

Substituting r with y the new expression obtained is reported in Eq. A.5.

$$U_{avg} = -\frac{2u_{max}}{R^2} \int_R^0 r\left(y/R\right)^{1/n} dr \tag{A.5}$$

Solving the integral and manipulating the expression to obtain u_{max}, the expression obtained is reported in Eq. A.6.

$$u_{max} = \frac{(n+1)(2n+1)U_{avg}}{2n^2} \tag{A.6}$$

Combining Eq. A.6 in Eq. A.2, a new expression for the local velocity reported in Eq. A.7 is obtained.

$$U(y) = \frac{(n+1)(2n+1)U_{avg}}{2n^2} \left(\frac{y}{R}\right)^{\frac{1}{n}} \tag{A.7}$$

To generalize this formula to geometry different from pipes the radius R can be defined as half of the flow passage between two generic solid walls. Inserting the Eq. A.7 in the conditional statement in Eq. 4.5 the modification to be applied to the turbulent kinematic viscosity forseen by the new wall function approach is expressed in Eq. A.8.

$$\nu_t = \begin{cases} 0 & y^+ < 11 \\ \nu\left(\frac{y^+}{\frac{1}{\kappa}\log(Ey^+)} - 1\right) & 11 < y^+ < 300 \\ \nu\left(\frac{1}{2}\frac{y^+}{u_\tau \frac{(n+1)(2n+1)U_{avg}}{2n^2}\left(\frac{y_P}{R}\right)^{\frac{1}{n}}}C_f U_{avg}^2 - 1\right) & y^+ > 300 \end{cases} \tag{A.8}$$

Implementing the Eq.A.8 in the new wall function approach instead of Eq. 4.5 will evade the problems related to the discretization of the flow passages between two solid walls that occurred with the approach presented in Chapter 4, but it is still strictly

dependent on the characteristic of the domain geometry since the need to input the

values of R.

Appendix B

New wall function method with u_P described by the log-law

As deduced from the results presented in Chapter 5 and as already mentioned in Appendix A, one of the major problems related to the newly developed methodology is its mathematical formulation which includes the presence of the local velocity of the centroid of the cell at the wall computed by OpenFOAM u_P at the denominator. The presence of u_P at the denominator leads to a strong dependency on the refinement of the mesh used to discretize the domain in problems in which relatively narrow flow passages are present because in case the space between two solid walls with no-slip boundary condition imposed is discretized with too few cells the velocity is captured as equal to zero and the new wall function approach seems to not work as expected as seen for Test Case 5 in sub-channel 3. To avoid this dependency an alternative solution is to substitute the local velocity computed by OpenFOAM with an expression able to describe it.

In this appendix, the solution presented consists in extending the validity of the log-law, as the description of the actual variation of the velocity normal to the wall, to the outer region and exploiting it to describe the local velocity of the cell at the wall, so substantially it consists in the traditional conditional statement used in the traditional wall function approach reported in Eq. 2.27 with the multiplication of a constant B for the first term in the bracket.

The constant B is reported in Eq. B.1

$$B = \frac{1}{2} \left(\frac{U_{avg}}{u_\tau} \right)^2 C_f \tag{B.1}$$

Multiplying the Eq. B.1 to the first term in bracket of Eq. 2.27, the new conditional statement to be applied to the turbulent kinematic viscosity is reported in Eq. B.2.

$$\nu_t = \begin{cases} 0 & y^+ < 11 \\ \nu \left(\frac{1}{2} \frac{y^+}{\frac{1}{\kappa} \log(E y^+)} \left(\frac{U_{avg}}{u_\tau} \right)^2 C_f - 1 \right) & y^+ > 11 \end{cases} \tag{B.2}$$

Implementing the Eq.B.2 in the new wall function approach instead of Eq. 4.5 will evade the problems related to the discretization of the flow passages between two solid walls that occurred with the approach presented in Chapter 4.